DESIGN, CONSTRUCTION AND PRELIMINARY TESTING OF AN AEROSERVOELASTIC TEST APPARATUS TO BE USED IN ANKARA WIND TUNNEL

A THESIS SUBMITTED TO
GRADUATE SCHOOL OF NATURAL AND APPLIED SCIENCES
OF
MIDDLE EAST TECHNICAL UNIVERSITY

BY

SADULLAH UTKU UNAL

IN PARTIAL FULFILLMENT OF THE REQUIREMENTS
FOR
THE DEGREE OF MASTER OF SCIENCE
IN
MECHANICAL ENGINEERING

DECEMBER 2005

Approval of the Graduate School of Natural and Applied Sciences

Prof. Dr.Canan ÖZGEN
Director

I certify that this thesis satisfies all the requirements as a thesis for the degree of Master of Science

Prof. Dr. Kemal İDER
Head of Department

This is to certify that we have read this thesis and that in our opinion it is fully adequate, in scope and quality, as a thesis for the degree of Master of Science

Prof. Dr. Bülent E. PLATİN
Co-Supervisor

Prof. Dr. Tuna BALKAN
Supervisor

Examining Committee Members

Prof. Dr. Kahraman ALBAYRAK (METU, ME) _____

Prof. Dr. Tuna BALKAN (METU, ME) _____

Prof. Dr. Bülent E. PLATİN (METU, ME) _____

Assoc. Prof. Dr. İlhan KONUKSEVEN (METU, ME) _____

Dr. Gökmen MAHMUTYAZICIOĞLU (TÜBİTAK-SAGE) _____

I hereby declare that all information in this document has been obtained and presented in accordance with academic rules and ethical conduct. I also declare that, as required by these rules and conduct, I have fully cited and referenced all material and results that are not original to this work.

Name, Last name : Sadullah Utku ÜNAL

Signature :

ABSTRACT

DESIGN, CONSTRUCTION, AND PRELIMINARY TESTING OF AN AEROSERVOELASTIC TEST APPARATUS TO BE USED IN ANKARA WIND TUNNEL

Ünal, Sadullah Utku
M.Sc., Department of Mechanical Engineering
Supervisor: Prof Dr. Tuna Balkan
Co-Supervisor: Prof Dr. Bülent E. Platin

December 2005, 128 pages

In this thesis, an aeroservoelastic test apparatus is designed to investigate the flutter phenomena in a low speed wind tunnel environment. Flutter is an aeroelastic instability that may occur at control surfaces of aircrafts and missiles. Aerodynamic, elastic and inertial forces are involved in flutter. A mathemetical model using aeroelastic equations of motion is derived to investigate flutter and is used as a basis to design the test set-up. Simulations using this mathematical model are performed and critical flutter velocities and frequencies are found. Stiffness characteristics of the test set-up are determined using the results of these simulations. The test set-up is a two degrees of freedom system, with motions in pitch and plunge, and is controlled by a servomotor in the pitch degree of freedom. A NACA 0012 airfoil is used as a control surface in the test set-up. Using this set-up, the flutter phenomena is generated in the Ankara Wind Tunnel (AWT) and experiments are conducted to validate the results of the theoretical aeroelastic mathematical model calculations.

Keywords: Aeroelasticity, Aeroservoelasticity, Flutter, Wind-Tunnel Testing, Aeroservoelastic Test Setup

ÖZ

ANKARA RÜZGAR TÜNELİ'NDE KULLANILMAK ÜZERE BİR AEROSERVOELASTİK TEST DÜZENEĞİNİN TASARIMI, KURULUMU VE DENEME TESTLERİNİN YAPILMASI

Ünal, Sadullah Utku
Yüksek Lisans, Makina Mühendisliği Bölümü
Tez Yöneticisi: Prof. Dr. Tuna Balkan
Ortak Tez Yöneticisi: Prof. Dr. Bülent E. Platin

Aralık 2005, 128 sayfa

Bu tez çalışmasında çırpıntı olayını gözlemlemek için, düşük hızlı rüzgar tüneli ortamında kullanılmak üzere bir aeroservoelastik test düzeneği tasarlanmıştır. Çırpıntı, uçakların ve füzelerin kontrol yüzeylerinde oluşabilecek bir aeroelastik kararsızlıktır. Çırpıntıda, aerodinamik, elastik ve ataletsel kuvvetler rol oynarlar. Çırpıntıyı incelemek için aeroelastik hareket denklemleri kullanılarak bir matematiksel model oluşturulmuş ve tasarım bu matematiksel modele dayandırılmıştır. Bu matematiksel model kullanılarak, kritik çırpıntı hızını ve frekansını bulmak için benzetimler yapılmıştır. Bu benzetimler sonucunda test düzeneğinin esneklik karakteristikleri çıkarılmıştır. Test düzeneği, yunuslama ve yaylanma olmak üzere iki serbestlik dereceli olup yunuslama hareketi bir servomotor tarafından denetlenmektedir. Test düzeneğinde kontrol yüzeyi olarak bir NACA 0012 profili kullanılmıştır. Aeroservoelastik Test Düzeneği (ATD) olarak adlandırılan bu test düzeneği kullanılarak Ankara Rüzgar Tüneli'nde yapılan deneylerin sonuçları ile kullanılan kuramsal aeroelastik matematiksel model hesaplamaları doğrulanmıştır.

Anahtar Kelimeler: Aeroelastisite, Aeroservoelastisite, Çırpıntı, Rüzgar Tüneli Testi, Aeroservoelastik Test Düzeneği.

ACKNOWLEDGEMENTS

The author wishes to express his deepest gratitude to his supervisor Prof. Dr. Tuna BALKAN and Co-supervisor Prof. Dr. Bülent E. PLATİN for their guidance, advice, criticism, encouragements and insight throughout the research.

The technical assistance of Erdinç N. YILDIZ and Alper AKMEŞE, both from TÜBİTAK-SAGE Mechatronics Division, helped me when I was hopeless. Their help and suggestions are greatfully acknowledged.

I wish to thank to TÜBİTAK-SAGE who introduced me with the subject of aeroelasticity, provided this subject as my thesis topic, supported financially the expenses of my thesis and allowed me to perform experiments in Ankara Wind Tunnel . The computer programs and enourmous knowledge about aeroelasticity and instrumentation helped me during my thesis.

And to Gülesin, who was always with me.

TABLE OF CONTENTS

PLAGIARISM.....i
ABSTRACT..... iv
ÖZ..... vi
ACKNOWLEDGEMENTS.....viii
TABLE OF CONTENTS..... ix
LIST OF TABLES xi
LIST OF FIGURES xii
NOMENCLATURE.....xvi
CHAPTER
1 INTRODUCTION 1
1.1 General.....1
1.2 Ankara Wind Tunnel.....2
1.3 Objectives of the thesis 4
1.4 Scope of the thesis.....4
2 LITERATURE SURVEY 6
2.1 Summary of the chapter.....10
3 AEROELASTICITY.....11
3.1 Introduction.....11
3.2 Historical Background 15
3.3 Summary of the chapter.....19
4 MATHEMATICAL MODELING OF AN AEROELASTIC SYSTEM AND SOLUTION OF FLUTTER EQUATION 20
4.1 Mathematical modeling of a typical section 20
4.2 Solution of the flutter equation 28
4.3 Open loop response of the aeroelastic system.....32
4.4 Summary of the chapter.....38
5 THE TEST SETUP 39
5.1 Motor Selection and Spring Design 39

5.2 Mechanical Parts of the Test Setup 44
5.3 Modal Analysis of the Airfoil 50
5.4 Summary of the chapter 54
6 WIND TUNNEL EXPERIMENTS 55
6.1 Design of experiments in the wind tunnel 55
6.2 Wind Tunnel Experiments 56
6.3 Summary of the chapter 79
7 SUMMARY AND CONCLUSIONS 81
7.1 Summary 81
7.2 Conclusions 82
7.3 Recommendations for future work 84
8 REFERENCES 86
APPENDICES
1 MATLAB® M - FILES 89
1.1 M-file for theoretical flutter calculations 89
1.2 M-file for determining the aeroelastic system matrix at certain air speed 91
1.3 M-file for motor selection calculation 93
1.4 M-file for spring design calculations 95
1.5 Modified m-file for calculating the critical flutter speed and frequency with damping 96
2 TECHNICAL DRAWINGS AND DATA SHEETS 99
2.1 Technical Drawings of the components 100
2.2 Data sheets 106
3 TABLES RELATED TO EXPERIMENTS 112
3.1 Critical Flutter velocities and frequencies for different pitch and plunge stiffness values 113
3.2 Similitude check for different stiffness value combinations 115
3.3 Observations during flutter experiments 116
4 GRAPHS OF EXPERIMENTAL DATA 124

LIST OF TABLES

Table 1. 1: Description of Figure 1 3
Table 4 1: Mass and Inertia properties used in flutter equation. 30
Table 4 2: Pitch and Plunge stiffness values for the same aeroelastic plant. 33
Table 5. 1: Parameters of the selected motor AKM42G. 41
Table 5. 2: Number of active coils and stiffness properties of the designed torsional springs 42
Table 5. 3: Number of active coils and stiffness properties of the designed compression springs. 43
Table A3.1 1: Critical flutter speed and flutter frequency for plunge stiffness of 30,000 N/m. 113
Table A3.1 2: Critical flutter speed and flutter frequency for plunge stiffness of 20,000 N/m. 113
Table A3.1 3: Critical flutter speed and flutter frequency for plunge stiffness of 15,000 N/m. 113
Table A3.1 4: Critical flutter speed and flutter frequency for plunge stiffness of 12,000 N/m. 114
Table A3.1 5: Critical flutter speed and flutter frequency for plunge stiffness of 10,000 N/m. 114
Table A3.2 1: Similitude check table for different stiffness value combinations. 115
Table A3.3 1: Observations during wind tunnel experiments. 116

LIST OF FIGURES

Figure 1. 1: Cross Section of Ankara Wind Tunnel 3
Figure 3. 2: Cut-away drawing of TDT at Langley 16
Figure 3. 3: A Cessna Aircraft, modeled and instrumented for aeroelastic experiments at TDT 18
Figure 4. 1: The Typical Section 21
Figure 4. 2: Open-loop poles. 31
Figure 4. 3: The system becomes unstable between 32nd and 33rd iteration; between 32 m/s and 33 m/s. 32
Figure 4. 4: Simulink Model to observe the open loop responses of the aeroelastic system with different stiffness value combinations. 33
Figure 4. 5: Open loop response of pitch and plunge motions of Plant 1 of Table 4.2 at U=31 m/s. 34
Figure 4. 6: Open loop response of pitch and plunge motions of Plant 1 of Table 4.2 at U=34 m/s. 34
Figure 4. 7: Open loop responses of pitch and plunge motions of Plant 2 of Table 4.2 at U=70 m/s. 36
Figure 4. 8: Open loop responses of pitch and plunge motions of Plant 3 of Table 4.2 at U=35 m/s. 36
Figure 4. 9: Open loop responses of pitch and plunge motions of Plant 4 of Table 4.2 at U=32 m/s. 37
Figure 4. 10: Open loop responses of pitch and plunge motions of Plant 5 of Table 4.2 at U=60 m. 37
Figure 5. 1: Power requirement for the motor. 40
Figure 5. 2: NACA 0012 Airfoil. 44
Figure 5. 3: Airfoil Shaft. 45
Figure 5. 4: Isometric view of the upper casing. 46
Figure 5. 5: Isometric view of the linear guide interface. 46

Figure 5. 6: Isometric view of the spring holders. 47
Figure 5. 7: Two isometric views of the casing. 48
Figure 5. 8: Assembly of the test setup. 48
Figure 5. 9: Exploded view of the test setup. 49
Figure 5. 10: 1st bending mode of the airfoil and the shaft @ 53.2 Hz. 51
Figure 5. 11: 1st bending mode of the airfoil and the shaft @ 53.2 Hz., perspective view. 52
Figure 5. 12: 2nd Bending mode of the airfoil and the shaft @ 62.6 Hz. 52
Figure 5. 13: 3rd mode shape of the airfoil and the shaft @ 210.5 Hz. 53
Figure 5. 14: 3rd mode shape of the airfoil and the shaft @ 210.5 Hz., perspective view. 53
Figure 6. 1: The ATD placed in the wind tunnel. 57
Figure 6. 2: The ATD viewed from under the wind tunnel ground. 57
Figure 6. 3: Orientation of the airfoil with respect to the wind tunnel centerline. 58
Figure 6. 4: National Instruments' PCI 6031E Analog Input Module. 59
Figure 6. 5: Kollmorgen® Servostar 620 and Kollmorgen® Servostar 603 digital servo amplifiers. 60
Figure 6. 6: Damped oscillations at 74.7 m/s 61
Figure 6. 7: Pulse response of pitch angle and plunge displacement at 0 m/s, after improvements. 64
Figure 6. 8: Frequency response of the pitch angle to motor input. 65
Figure 6. 9: Frequency response of the plunge displacement to motor input. 66
Figure 6. 10: Pulse responses in each degree of freedom, motor command and motor angle at U=10 m/s. 67
Figure 6. 11: Pulse responses in each degree of freedom, motor command and motor angle at U=20 m/s. 68
Figure 6. 12: Pulse responses in each degree of freedom, motor command and motor angle at U=30 m/s. 68

Figure 6. 13: Pulse responses in each degree of freedom, motor command and motor angle at U=30 m/s. 69
Figure 6. 14: Power spectral density of the data acquired from the linear scale channel. 70
Figure 6. 15: Accelerometer measurements at U=30 m/s. 71
Figure 6. 16: Undamped oscillations in pitch and plunge degrees of freedom at 60.6 m/s. 72
Figure 6. 17: Limit cycle oscillations in pitch degree of freedom at 53 m/s. 73
Figure 6. 18: FFT graph of limit cycle oscillations at U=50 m/s. 74
Figure 6. 19: FFT graph of limit cycle oscillations at U=50 m/s with peaks at distinct frequencies marked on the graph. 75
Figure 6. 20: FFT graph of the limit cycle oscillations at U=51 m/s. 76
Figure 6. 21: FFT graph of the limit cycle oscillations at U=52 m/s. 76
Figure 6. 22: FFT graph of the limit cycle oscillations at U=53 m/s. 77
Figure 6. 23: FFT graph of the limit cycle oscillations at U=55 m/s. 77
Figure 6. 24: FFT graph of the limit cycle oscillations at U=56 m/s. 78
Figure 6. 25:Amplitudes of limit cycle oscillations with respect to air speed. 78
Figure 6. 26: Oscillations during flutter in pitch and plunge at 60.5 m/s. .. 79
Figure A.2. 1: Technical drawing of the airfoil shaft. 100
Figure A.2. 2: Technical drawing of the casing. 101
Figure A.2. 3: Technical drawing of the linear guide interfaces. 102
Figure A.2. 4: Technical drawing of the motor shaft. 103
Figure A.2. 5: Technical drawing of the spring holder. 104
Figure A.2. 6: Technical drawing of the upper casing. 105
Figure A.2. 7: Datasheet of RE-21-1-B71 Resolver. 106
Figure A.2. 8: The datasheet of Lenord Bauer's GEL176 A0100 A Linear Scale. 107
Figure A.2. 9: A sample page of the Sumitomo's FC-A35-29 gearbox showing the inertia and stiffness properties of the gearbox. 111

Figure A4. 1: Accelerometer measurements during 2º pulse response at U=10 m/s. 124
Figure A4. 2: Accelerometer measurements during 2º pulse response at U=20 m/s. 125
Figure A4. 3: Accelerometer measurements during 2º pulse response at U=30 m/s. 125
Figure A4. 4: Accelerometer measurements during 2º pulse response at U=40 m/s. 126
Figure A4. 5: Pitch response in sinesweep test with in put amplitude of 6º before the modifications..... 126
Figure A4. 6: Plunge response in sinesweep test with in put amplitude of 6º before the modifications. 127
Figure A4. 7: Pitch response in sinesweep test with in put amplitude of 2º after the modifications..... 127
Figure A4. 8: Plunge response in sinesweep test with in put amplitude of 2º after the modifications. 128

NOMENCLATURE

[B] : Damping matrix.

$[B_{nc}]$: Aerodynamic non-circulatory damping matrix.

[K] : Stiffness matrix.

[M] : Mass matrix.

$[M_{nc}]$: Aerodynamic non-circulatory mass matrix.

a : Nondimensional distance of the elastic axis from the mid-chord.

b: : Half chord length.

C : Spring index.

C(k) : Theodorsen's function.

d : Spring wire diameter.

D : Spring diameter.

E : Modulus of elasticity.

G : Shear modulus of elasticity.

h : Plunge displacement of the mechanism.

H(k) : Hankel function.

I_α : Moment of inertia of the airfoil.

j :Imaginary number.

k: : Reduced frequency, Strouhal's number.

K_h : Plunge stiffness.

K_α : Pitch stiffness.

l: : Span of the control surface.

L : Aerodynamic lift force.

m : Mass of the mechanism.

M : Aerodynamic moment.

N : Number of active coils in springs.

S_α : Static mass moment per unit span.

t : Time.

U : Free stream air velocity.

x_{pa} : Aerodynamic states.

x_α : Nondimensional static unbalance distance from elastic axis.

α : Pitch displacement of the airfoil.

δ : Ratio of the magnitudes of oscillations.

ζ : Damping ratio.

ρ : Air density.

σ : Tensile stress due to bending.

τ : Shear stress.

ω_h : Uncoupled plunge natural frequency.

ω_σ : Uncoupled pitch natural frequency.

$(\dot{})$: Differentiation with respect to time.

CHAPTER 1

INTRODUCTION

1.1 General

Guidance in airborne structures such as aircrafts and missiles is made by control surfaces. Aircrafts are controlled by moveable ailerons which are placed usually at the rear section of a wing and missiles are controlled by control surfaces placed in the front part or the aft part of the missile body. Ailerons in aircrafts are driven by hydraulic and electromechanical mechanisms whereas the control surfaces of the missiles are driven by electromechanical, hydraulic, and even pneumatic mechanisms. These surfaces are subjected to aerodynamic loading during their operation and this loading may affect the control surface performance, thus affecting the overall system performance. Therefore, these control surfaces must withstand aerodynamic loading and instabilities should be avoided in the flight envelope.

Flutter is the most important dynamic instability in aeroelasticity and it is mostly encountered in airborne structures subjected to large lateral aerodynamic loads of lift type [1]. The structure presents a self-sustained oscillatory behavior at a certain critical airspeed, called as the critical flutter speed [2]. In general, coupling of several degrees of freedom is essential for flutter to occur, and the oscillation that occurs at the critical flutter speed is harmonic [2]. Above that critical speed oscillations are divergent

Demand for high maneuverable and high speed aircraft has increased since the World War II. This demand increased the effort in the design of aircraft structures encountering aeroelastic instabilities. Mass balancing, structural modifications to increase the stiffness properties of the structures, and modifications of the elastic axis location may result in

an enormous increase in weight, contradicting with the aircraft speed and performance requirements. Nowadays active control techniques on control surfaces for suppression of flutter are used to increase flutter speed without any additional weight.

Since flutter is destructive for aircraft components and airborne structures, critical components should be tested in wind tunnels to avoid failure during flight. Full scale models of wings or control surfaces, and/or scaled down models of the aircraft are constructed and instrumented for flutter experiments. These experiments are also performed to validate mathematical models to predict critical flutter speed. The behavior of the structure is observed prior to flight in a safe laboratory environment, and a safe flight envelope is constructed. Also active control strategies may be tested to suppress flutter and expand the flight envelope. Experiments with different types of active controllers are carried out to compare the performances of each control strategy with one another. Flight flutter tests are also performed on aircrafts and critical flutter speed is predicted with accelerometer measurements on the wings and control surfaces of the aircrafts, which is an expensive way to observe flutter phenomena. Wind tunnel models are also used to measure the pressure distribution on the control surface in an unsteady flow during flutter [17].

In flutter experiments, flexible wing models or rigid wing models with flexible mounting systems may be used. The former is a more realistic approach, but the latter is more suitable for easy mounting in wind tunnels and test models can be changed without replacing the mounting system [3]. Also instrumentation needs not be replaced at every change of the wind tunnel model. But if scaled down models of aircrafts are being tested, instrumentation should be changed on every model.

1.2 Ankara Wind Tunnel

Flutter experiments in this thesis are carried in Ankara Wind Tunnel (AWT). It was built between 1946 and 1950 and was modernized by

TÜBİTAK-SAGE between 1993 and 1998. AWT is a low subsonic wind tunnel with maximum 0.3 Mach speed capacity which corresponds to approximately 100 m/s airspeed. It has a cross-section of 3.05 m x 2.44 m at the test section and the test section length is 6.10m. Figure 1.1 shows a cross section view of AWT and Table 1.1 gives detailed description of the Figure 1.1 as well as some technical specifications.

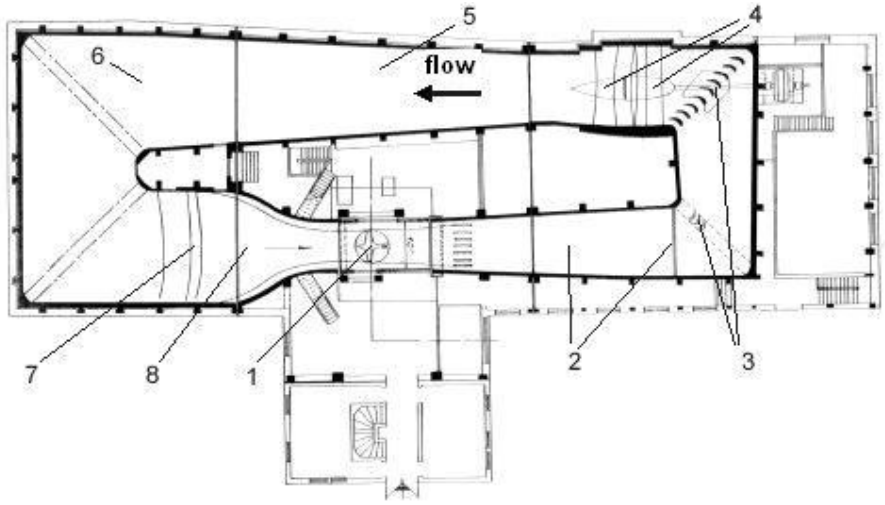

Figure 1. 1: Cross Section of Ankara Wind Tunnel

Table 1. 1: Description of Figure 1

①	Test Room, 3.05x2.44x6.10m	⑤	Pressure room, 5mx5mx10m, 8 º expansion angle
②	Diffuser and safety screen, 5º expansion angle.	⑥	Second guidance vane group
③	First guidance vane group	⑦	Turbulence screens
④	Propeller and stators	⑧	Contraction cone, contraction ratio is 7.5.

AWT serves in many engineering areas. Aerodynamic performance testing, external loads effect testing, store separation testing and design

change effect testing are the ordinary tests carried in AWT. Besides, wind and structure interaction tests for buildings and other civil engineering structures, performance tests including fuel consumption and maneuverability properties of automobiles are being investigated and studied in AWT. But a flutter test has never been carried in AWT.

1.3 Objectives of the thesis

There are many studies currently going on at TÜBİTAK-SAGE about aeroelasticity. Aeroservoelasticity, flutter prediction and flight flutter testing are among these studies. The motivation of this thesis was designing a two degree of freedom test bed to validate the results of these studies by wind tunnel tests. Observation of flutter using the test setup in AWT was the objective of this study. The stiffness characteristics of the test setup were aimed to be changed by using different springs so that flutter could be observed at different air speeds.

For active flutter suppression studies, the setup is aimed to be controllable in pitch degree of freedom. The system bandwidth was set as 50 Hz at 1º input command. Also it is aimed to measure the accelerations on some specific points of the airfoil for flutter prediction from accelerometer data. The effects of certain conditions such as nonlinearities due to friction and backlash on the critical flutter speed and frequency were also targeted to be observed.

1.4 Scope of the thesis

In this thesis, a two degree of freedom structure is designed, manufactured, and constructed for observation of flutter in Ankara Wind Tunnel (AWT). A NACA 0012 airfoil profile is used as the wing model since it is thin and mathematical models are derived for thin airfoils. Position sensors to observe the motion of the model in two separate degrees of freedom, pitch and plunge, and a servomotor is connected to the model through a shaft and a spring in the pitch degree of freedom. Stiffness

characteristics of the model are determined by compression springs in plunge degree of freedom and a torsional spring, placed between the motor and model shaft in pitch.

A brief outline of this thesis is as follows: In Chapter 2, a brief summary of the previous works done in theoretical and experimental aeroelasticity is given. Aeroelasticity and aeroelastic instabilities are introduced in Chapter 3. Experimental aeroelasticity, with historical background is also introduced in this chapter. In Chapter 4, equations of motion of a typical section using unsteady incompressible aerodynamic forces are given and the solution of the flutter equation for the model that is used in the experiments is presented. Mechanical design of the test setup is discussed in Chapter 5. This chapter includes calculations made for the selection of proper torsional and compression springs and also selection of the servomotor and sensors. The test setup is described with illustrative figures and detailed drawings. Modal analysis results of the system are presented. The results of the wind tunnel experiments are given in Chapter 6. Finally, conclusion and future work suggestions are presented in Chapter 7.

CHAPTER 2

LITERATURE SURVEY

Aeroelasticity was first studied in detail by Thedore Theodorsen in 1935. In his famous report [4], he introduced Theodorsen Function $C(k)$ for the oscillatory part of aerodynamic loads. In this report, he showed the effects of certain parameters on the critical flutter speed and frequency, namely density ratio, bending-torsion frequency ratio, dimensionless static unbalance, dimensionless radius of gyration. Later, he suggested methods to solve the flutter problem numerically and conducted wind tunnel experiments to validate his results [5]. A famous and basic book for flutter studies was written by Fung [2], first in 1955. In this book Fung discusses some aeroelastic instabilities including divergence, flutter and aileron reversal, etc; fundamentals of flutter analysis and gives aeroelastic equation of motion in detail.

Flutter and divergence phenomena were analyzed using the generalized aeroelastic analysis method by Edwards J.W., and Wieseman C.D. They applied the analysis to three different check cases which are restrained airfoil model, unrestrained airfoil model and a BAH (Bisplinghoff, Ashley, and Halfman) wing model. Exact root loci that show the flutter and divergence of the airfoils were given and inconsistencies of the root loci with other publications were discussed and resolved. Doublet-Lattice Method computer code was introduced for calculation of the root loci of the wing model. They summarized the results of critical flutter speed and frequencies of the restrained and unrestrained airfoils [6].

An experimental flutter study was carried by Borglund D., and Kuttenkueler in 2001. They studied the aeroservoelastic behavior of a thin

rectangular wing with a controllable trailing edge flap. They conducted experiments with a high aspect ratio wing model. Their experiments showed that their stability analysis agreed with experimental data. They stabilized the model during flutter with a fixed structure feedback controller. They were able to increase the critical flutter speed and verified the results with experiments [7].

Özkaynak A., Özkök B., Katemliadis S., and Weltin U. constructed an experimental setup for flutter control by manipulating the materialistic properties of the setup. They changed the torsional stiffness characteristics and center of mass position of the test setup to increase the critical flutter speed. A step motor is used to change the torsional stiffness characteristics and a servomotor is used to change the center of mass. For control of flutter, they designed three different controllers, namely “On/Off Controller”, “PID Controller”, and “Neural Network Controller” and concluded that the use of neural networks resulted in a faster response and less oscillations [22].

Akmeşe A., Cömert M.D., and Platin B.E. analyzed aeroservoelastic behavior of missile control surfaces by using robust control methods. They constructed a three degree of freedom aeroservoelastic model of a missile control actuation system. They studied the effects of uncertainties on the flutter and instability speeds of the control actuation system. They modeled the control surface as a typical section with uncertainties in damping and stiffness coefficients and modeled the actuator dynamics as a second order system with a frequency varying uncertainty. They concluded that dynamic pressures of flutter and instability calculated by V-g method and μ-method were in accordance. They showed that the robust dynamic pressure of flutter and instability can be less than the results obtained by dividing nominal values by common safety factors [23].

Lee B.H.K., Gong L., and Wong W.S. analyzed nonlinear dynamic response of a two degree of freedom system and they applied this to aeroelasticity. They applied cubic stiffness in pitch and plunge degrees of

freedom as nonlinearity. They derived the governing equations based on a coupled system of Duffling's Equations, for a two dimensional airfoil oscillating in pitch and plunge. For the solution only the harmonic motion was considered and they used the method of slowly varying amplitude to investigate the dynamic response of the system to external excitation. Examples were given for a dynamic system without aerodynamic forces to show the jump phenomenon where the solution jumps from one branch of the amplitude frequency curve to the other. The behavior of a two degree of freedom airfoil as the speed approaches critical flutter speed was shown and analytical results were verified by numerical calculations [8].

Goorjian P.M. and Guruswamy G.P. studied the unsteady transonic flows about airfoils and wings including aeroelastic effects. They summarized the results for unsteady, transonic, small disturbance potential equation on airfoils and wings as a survey. They gave the results for transonic flow with moving shock waves over an airfoil and compared with experimental results. They also studied a low aspect ratio wing and a variable sweep wing [9].

Pidapardi R.M.V analyzed flutter of cantilevered curve composite panels. He used a 48 degree of freedom doubly curved quadrilateral thin shell finite element to study the supersonic flutter of cantilevered curved composite panels. He presented their results to illustrate the behavior of flutter for curved cylindrical panels and demonstrated the accuracy, efficiency, and applicability of the present finite element method by examples with results that compare well with the available solutions in literature [10].

NASA started an experimental aeroelastic and aeroservoelastic research program at Langley Transonic Wind Tunnel. This program was named Benchmark Active Control Technologies (BACT). In the BACT program an aeroservoelastic test apparatus was used as a test bed to study the effects of certain controllers designed with different techniques. Adams W.M, Waszak M.R. and Christhilf introduced three different

controllers to suppress flutter at low speed using the BACT model. The first controller was designed with classical control tools such as pole zero loci and Nyquist diagrams. In the second method they used linear combinations of several accelerometer measurements and dynamic compensation to synthesize the modal rate of the critical mode for feedback to the distributed control surfaces. The third one was a LQG controller to minimize energy. They concluded that only the traditional controller was sufficiently robust to errors in the nominal plant to suppress flutter during wind tunnel tests [11]. Using BACT model, also unsteady-flow distributions on a NACA0012 airfoil was investigated [12]. The mathematical derivation of aeroelastic equations of motion was given in [13]. The physical properties of the BACT model were given in [14].

BACT model was tested in [3], but physical properties were changed so that the model should encounter flutter in a low speed wind tunnel environment. A state-feedback controller was designed and it was shown that the controller was able to increase the critical flutter speed. Flutter frequencies and flutter speeds were listed in detail.

A nonlinear aeroelastic test bed was designed at Texas A&M, named NATA (Nonlinear Aeroelastic Test Apparatus). O'neil, Block, Ko, Thompson and Dowell investigated nonlinear responses of three different wing sections as well as the development of active flutter suppression controllers. They used models with nonlinear structural stiffness parameters and these parameters could be changed using a cam mechanism. They observed limit cycle oscillations with nonlinear spring hardening behavior. They also studied the effect of cubic stiffness on flutter and they observed that limit cycle oscillations occurred and the stability boundary was insensitive to initial conditions [15].

Lind and Brenner also used a test bed for implementation of their robust control strategies at Department of Aerospace Engineering at Texas A&M University. The open loop responses of the system with different kinds of nonlinearities were studied [16]. In his book, Lind gave

aeroelastic modeling of the test set-up as well as aeroservoelastic modeling including the interactions between the actuator and the test airfoil.

2.1 Summary of the chapter

In this chapter, a brief summary of the literature about the topic aeroelasticity is given. Aeroelastic systems were analyzed using different methods like generalized aeroelastic analysis method in [6], and robust control methods in [23]. Efffects of certain nonlinearities on critical flutter speed were investigated in [8, 16]. Various active control techniques for supression of flutter were implemented and the theoretical results were validated by experiments in [3, 7, 11, 15, 16, 22]. Experiments were carried out with various airfoil and wing types.

CHAPTER 3

AEROELASTICITY

3.1 Introduction

Aeroelasticity is often described as the science which studies the interactions between aerodynamic forces and elastic forces, and the effects of these forces on airborne structure design. Airborne structures are very flexible and this flexibility is responsible for various types of aeroelastic phenomena, which would not be observed if the structures were perfectly rigid. Structural flexibility may not be detrimental until deformations induce additional aerodynamic forces on the structure. These aerodynamic forces may induce greater displacements which would induce still greater aerodynamic forces. This interaction may tend to reach a stable equilibrium condition or they may tend to diverge to an aeroelastic instability condition. Since the weight limitation is an important parameter in airborne structure design, flexibility of the structure is unavoidable. Therefore aeroelasticity should be considered in detail during the design period.

However, the term aeroelasticity is not completely descriptive since some aeroelastic phenomena involve inertial forces as well as aerodynamic and elastic forces. The dynamic aeroelastic phenomena include inertial, aerodynamic and elastic forces whereas the static aeroelastic phenomena include only aerodynamic and elastic forces.

Collar's triangle is a diagram that is used to describe the interactions of aerodynamic, elastic and inertial forces, and aeroelastic phenomena [1]. In Figure 3-1, the three different types of forces are placed at the corners of the triangle and are represented by letters A, E, and I,

respectively. Aeroelastic phenomena are located on the triangle according to their relation to the three forces in each corner.

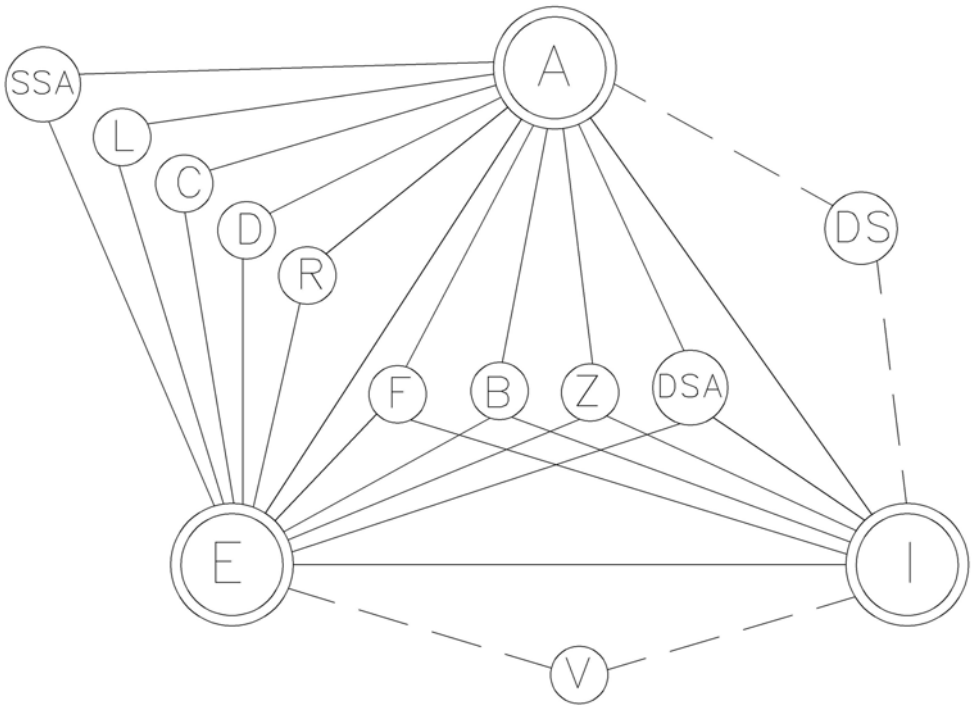

Forces	Aeroelastic Phenomena
A: Aerodynamic Force	F: Flutter
E: Elastic Force	B: Buffeting
I: Inertial Force	Z: Dynamic Response
	L: Load Distribution
	D: Divergence
	C: Control Effectiveness
	R: Control System Reversal

Related Fields	
V: Mechanical Vibrations	DSA: Aeroelastic Effects on Dynamic Stability
DS: Dynamic Stability	SSA: Aeroelastic Effects on Stability

Figure 3. 1: Collar's Aeroelastic Triangle of Forces [1]

Dynamic aeroelastic problems lie inside the triangle and are associated with the three forces. Flutter, F, which lies inside the triangle is an example of such dynamic aeroelastic phenomena. Static aeroelastic phenomena lie outside the triangle on the upper left side. Only aerodynamic and inertial forces are connected to these phenomena. For example the divergence (D) is a static aeroelastic phenomenon. The classes of problems connected by solid lines to the corners of the triangle in Figure 3.1 are usually accepted as principal ones. Other engineering disciplines can be placed on the diagram, like mechanical vibrations and rigid body aerodynamic stability and these fields are connected to related forces by dashed lines.

Although not mentioned in this diagram, thermal forces and control forces may be added to the triangle to define aerothermoelastic, aeroservoelastic and aerothermoservoelastic problems and phenomena. Because, the stress induced by high temperatures is important in aircraft structures.

Definitions of each aeroelastic phenomena described in the triangle are given in the following paragraphs [1].

- **Flutter, F:** A dynamic aeroelastic instability occurring in an aircraft in flight, at a speed called flutter speed, where the elasticity of the structure plays an essential part in the instability.
- **Buffeting, B:** Transient vibrations of aircraft structural components due to aerodynamic impulses produced by the wake behind the wings, nacelles, fuselage pods, or other components of the airplane.
- **Dynamic Response, Z:** Transient response of aircraft structural components produced by rapidly applied loads due to gusts, landing, gun reactions, abrupt control motions, moving shock waves, or other dynamic loads.

- **Divergence, D:** Static aeroelastic instability of a lifting surface of an aircraft in flight, at a speed called the divergence speed, where the elasticity of the lifting surface plays an essential role in instability.
- **Aeroelastic Effects on Stability, (D/S) SA:** Influence of elastic deformations of a structure on dynamic and static airplane stability.
- **Load Distribution, L:** Influence of elastic deformations of a structure on the distribution of aerodynamic pressures over the structure.
- **Control Effectiveness, C:** Influence of elastic deformations of a structure on the controllability of an aircraft.
- **Control System Reversal, R:** A condition occurring in flight, at a speed called control reversal speed, at which the intended effects of displacing a given component of a control system are completely nullified by elastic deformations of the structure.

The interaction between aerodynamic, inertial and elastic forces is also important for mechanical vibration engineers and civil engineers. Structures have different vibration characteristics in vacuum than in airflow, especially if the structure has a lifting surface. Civil engineers should consider the effects of aeroelasticity in their design phase, especially for high chimneys and long bridges. The collapse of Tacoma Narrows Bridge in 1940 is an outstanding example of aeroelastic failure of civil engineering structures. Aeroelasticity is also important in turbomachinary; the blades might encounter instabilities because of the complex flow around them. Design of helicopter blades is another example.

In the next section, a historical background of aeroelasticity and experimental aeroelasticity will be given.

3.2 Historical Background

Aeroelastic problems have been encountered since the first days of flight. Wright Brothers made beneficial use of aeroelasticity for roll control of their biplane by using wing warping in place of ailerons. They were also aware of the adverse aeroelastic effect of the loss of thrust of a propeller, due to twisting of the blades [1]. Since the aircraft speeds were relatively much smaller than today's modern aircrafts, statically designed structures mostly proved to be sufficiently rigid to preclude most aeroelastic instabilities. The encountered problems were solved by structural modifications. As the speeds increased, aircraft designers faced a wide variety of aeroelastic problems. Samuel P. Langley's monoplane suffered from a wing failure which could be described as torsional divergence. Success of Wright Brothers' biplane and failure of Langley's monoplane may be the original reason for people to choose biplanes rather than monoplanes.

The most important and widespread aeroelastic problem in the days when biplanes were dominant among military aircraft was the tail flutter problem. Aeroelastic wing problems appeared when the designers abandoned biplane construction with its interplane bracing and relatively high torsional rigidity, in favor of monoplane types. Monoplanes often had insufficient torsional rigidity, and flutter, loss of aileron effectiveness and change in load distribution resulted. Static strength tests were revealing that the wings were sufficiently strong enough for loading but they still collapsed. Further investigations showed that torsional deflection at the wing tips at high angles of attacks was the reason for the failures. The period of development of the cantilever monoplane aircraft was the period in which serious research and observation in aeroelasticity was made.

Theory came a little time after the observation of aeroelastic instabilities. A theory of wing-load distribution and wing divergence was first presented in 1926 and a theory of loss of lateral control and aileron reversal was first given in 1932. In 1934, Thedore Theodorsen presented

the mechanism of flutter with potential flow in his famous paper. He gave a complete theory for the two dimensional oscillating flat plate undergoing translation, torsion, and aileron type motions. He separated the non-circulatory part of the velocity potential from the circulatory part associated with the effect of wake. The trailing edge flow condition sets a relation between the two parts, whose solution leads to a combination of Bessel (or Henkel) functions, designated *C(k)*. This function establishes the lags between the airfoil motions and aerodynamic forces, and has been later denoted as Theodorsen's function *C(k),* where *k* is reduced frequency (Strouhal number) calculated as $\omega V/b$ (ω is the angular frequency, *V* is the airspeed, and *b* the half-chord length) [1]. But only a few designers were able to comprehend the theories and put them into practice.

After the construction of the theory, engineers designed and performed experiments to observe the flutter phenomena under their control in structural laboratories and wind tunnels that are built for this purpose. In order to determine the structural properties of the models before testing, static and dynamic structural test facilities as well as modal analysis systems were developed. NASA Langley Research Center was the first wind tunnel constructed for only observing flutter phenomena and transonic tests could be carried on in it. Later that tunnel was changed into Transonic Dynamics Tunnel (TDT). Figure 3.2 is a cut-away view of Transonic Dynamics Tunnel at NASA Langley Research Center.

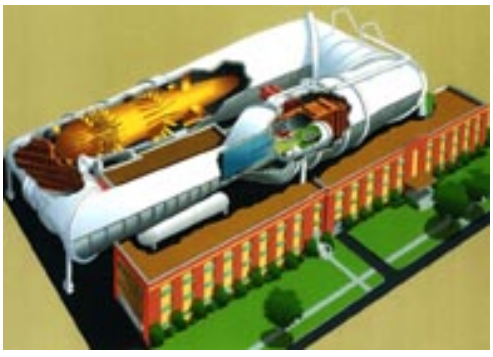

Figure 3. 2: Cut-away drawing of TDT at Langley

With the facilities at their hand, engineers focused on to the wind tunnel models and test apparatus. Improvements in models and mounting systems were made and measurement techniques and devices evolved to get a clearer view of the phenomena. Several different methods were used in constructing aeroelastic wind tunnel models to maintain certain scaling parameters. These methods included relatively simple plate-like models from balsa wood and complex replica models to validate full-scale designs. In replica modeling, each spar and rib of a wing were scaled using the same material for the model as was used in the aircraft. However, this was an expensive method, and it became more and more difficult to model accurately more efficient structures. A new method was developed called “spar-and-pod” construction. In this method a single aluminum spar is used to represent the majority of the stiffness of the model, and segmented pods which were attached to it provide the proper geometric shape and mass/inertia properties [17]. In order to implement active control on flutter wind tunnel models, many models were equipped with remotely actuated control devices. Figure 3.3 shows a Cessna aircraft prior to a wind tunnel test. Electromechanical and hydraulic control systems were developed. For observation of flutter phenomena, strain gages, potentiometers and accelerometers were commonly used. Gyroscopes were used for measuring model displacements and rates. Pressure transducers in models through the chord length were used to measure the static and dynamic pressure distributions.

Figure 3. 3: A Cessna Aircraft, modeled and instrumented for aeroelastic experiments at TDT

Experimental programs in different fields of aeroelasticity carried on. These include flight flutter testing or envelope clearance testing, aeroelastic tailoring, unsteady aerodynamics and active control. Flight flutter testing is the validation of aeroelastic characteristics of the aircraft and is carried on during flight. However, most flight programs were preceded by wind tunnel tests in order to demonstrate that the new vehicle designs were free from all unwanted static and dynamic response or instabilities throughout the simulated flight envelope [17]. Experiments were carried to measure the unsteady pressure distribution over oscillating wings. The results were compared with the CFD codes in different flow regimes. Development of active control strategies for improvement of aeroelastic response has relied heavily on experimental demonstrations and validations. These experiments were conducted to suppress flutter, to improve aircraft static stability, to increase wing roll control and to reduce aircraft gust response and helicopter rotor blade dynamic response [17].

Although the flutter phenomenon had been heavily studied theoretically and experimentally, not everything about aeroelastic behavior was known [17]. System behavior caused by structural nonlinearities (joint damping, freeplay), transonic aerodynamic loads (shocks, flow separation, viscosity) and active control system performance are still hot topics that are currently being studied.

3.3 Summary of the chapter

In this chapter, effects of aeroelasticity in the design of airborne structures are discussed. Collar's triangle is given to show the relations of aeroelasticity with different engineering fields. Definitions of various instabilities related to aeroelasticity are given in detail. A historical background of aeroelasticity is overviewed and some aeroelastic problems that people had to solve during first days of flight are presented. The theoretical study of Thedorsen on aeroelasticity, which is a very helpful analysis tool of flutter phenomena, is introduced. Experimental studies carried in wind tunnels are discussed with examples on various fields of aeroelasticity, for example flight flutter testing and implementation of active flutter suppression methods.

CHAPTER 4

MATHEMATICAL MODELING OF AN AEROELASTIC SYSTEM AND SOLUTION OF FLUTTER EQUATION

4.1 Mathematical modeling of a typical section

Figure 4.1 shows the location and description of the coordinate system used and some dimensional quantities of primary interest in modeling an aeroelastic system. This airfoil is a representative “typical section” used by Theodorsen and Garrick in their famous reports [4, 5]. They suggest that for purposes of theoretical flutter prediction, inertial and geometric properties of a large span and straight wing can be represented by a typical section with inertial and geometric properties of the wing at ¾ of the distance from root to tip. This suggestion holds where the aspect ratio is large, the sweep is small, and the sectional characteristics vary smoothly across span. The typical section representation is not only suitable for cantilever wing simulation but also for missile control surface aeroelastic analysis. Control surfaces are assumed to be chordwise rigid and obey the thin airfoil assumption. Since the control surface is connected to the control unit via a torsionally less stiff shaft than the control surface, it can be assumed that elastic rotation takes place at the connecting shaft only. The mechanical components of the servo system such as links of the mechanism or the transmission box, and the nonlinearities such as free play on these components will also decrease the equivalent stiffness of the shaft further. The difference between a cantilever wing and a control surface is that the bending stiffness of the control surface is much larger than its torsional stiffness, due to relatively low aspect ratio.

In Figure 4.1, z=0 line represents the undeflected airfoil centerline; b is the half-chord length; a is the ratio of the distance between the centerline and the elastic axis to the half-chord length b; x_α is the ratio of distance between the elastic axis and the center of gravity of the airfoil to the half-chord length b; h is the deflection of the airfoil in plunge direction and α is the deflection angle in pitch direction. K_h and K_α are the restraining spring stiffness values in plunge and pitch degree of freedoms, respectively. L is the aerodynamic lift force and M_y is the aerodynamic moment.

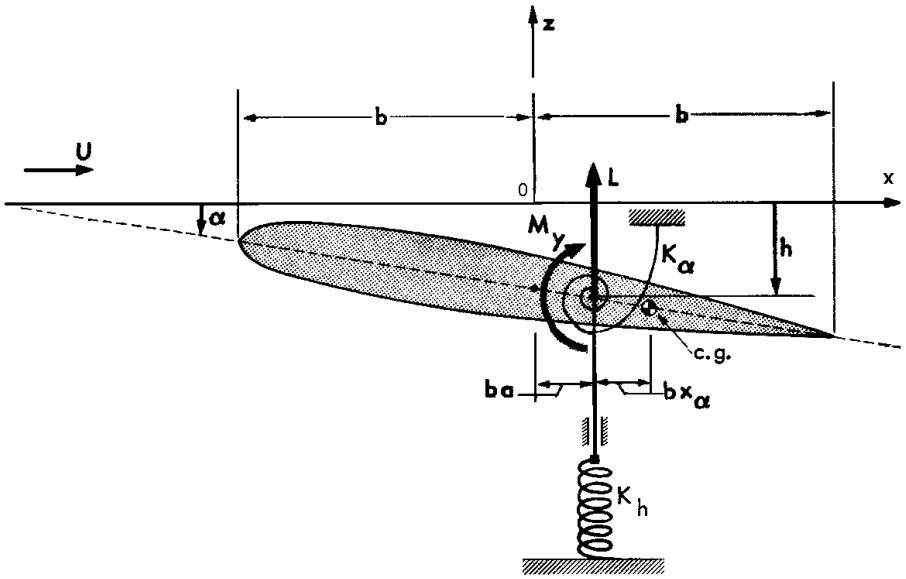

Figure 4. 1: The Typical Section [1].

The notation given above is called Theodorsen's notation. The general equations of motion per unit span length for the typical section without damping and linear stiffness parameters are given as;

$$m\ddot{h} + S_\alpha \ddot{\alpha} + K_h h = -L \tag{4-1a}$$

in plunge degree of freedom, and

$$S_\alpha \ddot{h} + I_\alpha \ddot{\alpha} + K_\alpha \alpha = M \tag{4-1b}$$

in pitch degree of freedom, where

$$S_\alpha = mbx_\alpha \tag{4-2}$$

is the static mass moment per unit span, I_α is the mass moment of inertia of the airfoil, K_h is the plunge stiffness, K_α is the pitch stiffness, L is the aerodynamic lift, and M is the aerodynamic moment.

Since the AWT has a maximum airspeed capacity of 100 m/s, subsonic incompressible unsteady aerodynamic expressions can be used for aerodynamic loading. Lift equation for unsteady incompressible flow per unit span is given as [2];

$$L = -\pi\rho b^2\left[\ddot{h} + U\alpha - ba\ddot{\alpha}\right] - 2\pi\rho UbC(k)\left[U\alpha + \dot{h} + \dot{\alpha}b\left(a + \frac{1}{2}\right)\right] \tag{4-3a}$$

and the moment equation for unsteady subsonic incompressible flow per unit span is [2];

$$M = \pi\rho b^2\left[ba\ddot{h} - Ub\left(\frac{1}{2} - a\right)\dot{\alpha} - b^2\left(\frac{1}{8} + a^2\right)\ddot{\alpha}\right] +$$
$$2\pi\rho Ub^2\left(a + \frac{1}{2}\right)C(k)\left[U\alpha + \dot{h} + b\left(\frac{1}{2} - a\right)\dot{\alpha}\right] \tag{4-3b}$$

In Eq. 4-3a and 4-3b ρ is the air density, U is the air speed, $C(k)$ is the Theodorsen's function. The aerodynamic lift and moment equations are written in terms of aerodynamic states h and α. Theodorsen $C(k)$ is a complex valued function and k is the reduced frequency (wU/b). The exact expression of the Theodorsen's function is

$$C(k) = F(k) + iG(k) = \frac{H_1^{(2)}(k)}{H_1^{(2)}(k) + iH_0^{(2)}(k)} \tag{4-4}$$

where *H(k)* is the Henkel function [2]. Usually the exact Theodorsen function is not used directly, but it is replaced by approximate functions [2]. *C(k)* is approximated as [2]

$$C(k) = 1 - \frac{0.165}{1 - i\frac{0.0455}{k}} - \frac{0.335}{1 - i\frac{0.3}{k}} \quad \text{for } \mathrm{k} < 0.5 \tag{4-5}$$

and

$$C(k) = 1 - \frac{0.165}{1 - i\frac{0.041}{k}} - \frac{0.335}{1 - i\frac{0.32}{k}} \quad \text{for } k \geq 0.5 \tag{4-6}$$

Equations of motion can be written in matrix form, combining Eq's. 4-1a and 4-1b;

$$[M]\begin{bmatrix} \ddot{h} \\ \ddot{\alpha} \end{bmatrix} + [K]\begin{bmatrix} h \\ \alpha \end{bmatrix} = \begin{bmatrix} L \\ M \end{bmatrix} \tag{4-7}$$

Lift and moment Eq's of 4-3a and 4-3b become;

$$\begin{bmatrix} L \\ M \end{bmatrix} = \begin{bmatrix} -\pi\rho b^2 & \pi\rho a b^3 \\ \pi\rho a b^3 & \pi\rho b^4\left(\frac{1}{8} + a^2\right) \end{bmatrix}\begin{bmatrix} \ddot{h} \\ \ddot{\alpha} \end{bmatrix} + \begin{bmatrix} 0 & -\pi\rho b^2 U \\ 0 & -\pi\rho b^3 U\left(\frac{1}{2} - a\right) \end{bmatrix}\begin{bmatrix} \dot{h} \\ \dot{\alpha} \end{bmatrix}$$
$$+2\pi\rho U b C(k)\left(\begin{bmatrix} -1 & -b\left(\frac{1}{2} - a\right) \\ b\left(a + \frac{1}{2}\right) & b^2\left(a + \frac{1}{2}\right)\left(\frac{1}{2} - a\right) \end{bmatrix}\begin{bmatrix} \dot{h} \\ \dot{\alpha} \end{bmatrix} + U\begin{bmatrix} 0 & -1 \\ 0 & b\left(a + \frac{1}{2}\right) \end{bmatrix}\begin{bmatrix} h \\ \alpha \end{bmatrix}\right) \tag{4-8}$$

The lift and moment for incompressible subsonic flow can be separated into two parts; circulatory and non-circulatory. As stated earlier, circulatory parts are the terms involving the Theodorsen's function $C(k)$. The above equations can be re-arranged to separate circulatory and non-circulatory parts to give;

$$\begin{bmatrix} L \\ M \end{bmatrix} = \left[M_{nc}\right]\begin{bmatrix} \ddot{h} \\ \ddot{\alpha} \end{bmatrix} + \left[B_{nc}\right]\begin{bmatrix} \dot{h} \\ \dot{\alpha} \end{bmatrix} + 2\pi\rho UbC(k)\left([R][S_1]\begin{bmatrix} \dot{h} \\ \dot{\alpha} \end{bmatrix} + U[R][S_2]\begin{bmatrix} h \\ \alpha \end{bmatrix}\right) \tag{4-9}$$

where

$$[R] = \begin{bmatrix} -1 \\ b\left(a + \frac{1}{2}\right) \end{bmatrix} \qquad [S_1] = \begin{bmatrix} 1 & b\left(\frac{1}{2} - a\right) \end{bmatrix} \qquad [S_2] = [0 \quad 1] \tag{4-10}$$

and $\left[M_{nc}\right]$ and $\left[B_{nc}\right]$ are the aerodynamic non-circulatory mass and damping matrices.

Theodorsen Function *C(k)* is approximated as in Eq. 4-5 and rewritten in the following form,

$$C(k) = 0.5 + \frac{0.0075}{jk + 0.0455} + \frac{0.10055}{jk + 0.3} \tag{4-11}$$

If the circulatory parts of the lift and moment equations are treated separately and the Theodorsen Function approximation is written in Laplace form, after some manipulations the circulatory part becomes;

$$2\pi\rho Ub\left(0.5+\frac{c_1 s+\frac{U}{b}c_2}{\frac{b^2}{U^2}s^2+b\frac{c_3}{U}s+c_4}\right)\left\{[R][S_1]\begin{bmatrix}\dot{h}\\ \dot{\alpha}\end{bmatrix}+U[R][S_2]\begin{bmatrix}h\\ \alpha\end{bmatrix}\right\}=$$

$$\pi\rho bU\left([R][S_1]\begin{bmatrix}\dot{h}\\ \dot{\alpha}\end{bmatrix}+U[R][S_2]\begin{bmatrix}h\\ \alpha\end{bmatrix}\right)+$$

$$2\pi\rho U^2\left(c_1 s+\frac{U}{b}c_2\right)[R]\left(\frac{\dot{h}+b(\frac{1}{2}-a)\dot{\alpha}+U\alpha}{s^2+\frac{U}{b}c_3 s+\frac{U^2}{b^2}c_4}\right)$$

(4-12)

From the above equality the effect of the circulatory part to damping and stiffness matrices can be seen. The circulatory damping and circulatory stiffness matrices are;

$$[B_c]=\pi\rho bU[R][S_1]\begin{bmatrix}\dot{h}\\ \dot{\alpha}\end{bmatrix}=\begin{bmatrix}-\pi\rho Ub & -\pi\rho Ub^2\left(\frac{1}{2}-a\right)\\ \pi\rho Ub^2\left(a+\frac{1}{2}\right) & \pi\rho Ub^3\left(a+\frac{1}{2}\right)\left(\frac{1}{2}-a\right)\end{bmatrix}\begin{bmatrix}\dot{h}\\ \dot{\alpha}\end{bmatrix}$$

(4-13)

and

$$[K_c]=\pi\rho bU^2[R][S_2]\begin{bmatrix}h\\ b\end{bmatrix}=\begin{bmatrix}0 & -\pi\rho bU^2\\ 0 & \pi\rho b^2U^2\left(a+\frac{1}{2}\right)\end{bmatrix}\begin{bmatrix}h\\ \alpha\end{bmatrix}\qquad(4\text{-}14)$$

The remaining part of the equality can be used to obtain the aerodynamic states. Since the approximation to the Theodorsen Function is of 2nd order, there will be two aerodynamic states. The order of

approximation defines the additional aerodynamic states added to the total number of states of the system.

By defining;

$$x_{pa} = \left(\frac{\dot{h} + b\left(\frac{1}{2} - a\right)\dot{\alpha} + U\alpha}{s^2 + \frac{U}{b}c_3 s + \frac{U^2}{b^2}c_4} \right) \tag{4-15}$$

the aerodynamic state equation in time domain can be written as

$$\begin{aligned} &\ddot{x}_{pa} + \frac{Uc_3}{b}\dot{x}_{pa} + \frac{U^2 c_4}{b^2}x_{pa} = \dot{h} + b\left(\frac{1}{2} - a\right)\dot{\alpha} + U\alpha \\ &x_{a1} = x_{pa}, \\ &x_{a2} = \dot{x}_{pa}, \\ &\ddot{x}_{pa} = \dot{h} + b\left(\frac{1}{2} - a\right)\dot{\alpha} + U\alpha - \frac{Uc_3}{b}\dot{x}_{pa} - \frac{U^2 c_4}{b^2}x_{pa} \end{aligned} \tag{4-16}$$

In state space form aerodynamic state equation can be written as;

$$\begin{bmatrix} \dot{x}_{a1} \\ \dot{x}_{a2} \end{bmatrix} = \begin{bmatrix} 0 & 0 \\ 1 & b\left(\frac{1}{2} - a\right) \end{bmatrix} \begin{bmatrix} \dot{h} \\ \dot{\alpha} \end{bmatrix} + \begin{bmatrix} 0 & 0 \\ 0 & U \end{bmatrix} \begin{bmatrix} h \\ \alpha \end{bmatrix} + \begin{bmatrix} 0 & 1 \\ -\frac{U^2 c_4}{b^2} & -\frac{Uc_3}{b} \end{bmatrix} \begin{bmatrix} x_{a1} \\ x_{a2} \end{bmatrix} \tag{4-17}$$

$$\begin{bmatrix} \dot{x}_{pa} \end{bmatrix} = \begin{bmatrix} E_1 \end{bmatrix} \begin{bmatrix} h \\ \alpha \end{bmatrix} + \begin{bmatrix} E_2 \end{bmatrix} \begin{bmatrix} \dot{h} \\ \dot{\alpha} \end{bmatrix} + \begin{bmatrix} F \end{bmatrix} \begin{bmatrix} x_{a1} \\ x_{a2} \end{bmatrix} \tag{4-18}$$

Eq. 4-12 becomes,

$$\left[B_c\right]\begin{bmatrix}\dot{h}\\ \dot{\alpha}\end{bmatrix}+\left[K_c\right]\begin{bmatrix}h\\ \alpha\end{bmatrix}+2\pi\rho U^2\left[R\right]\left(c_1 s+\frac{Uc_2}{b}\right)x_{pa}= \tag{4-19}$$

$$\left[B_c\right]\begin{bmatrix}\dot{h}\\ \dot{\alpha}\end{bmatrix}+\left[K_c\right]\begin{bmatrix}h\\ \alpha\end{bmatrix}+\left[D\right]\begin{bmatrix}x_{pa}\\ \dot{x}_{pa}\end{bmatrix}$$

where

$$\left[D\right]=2\pi\rho U^2\left[R\right]\left(c_1 s+\frac{Uc_2}{b}\right)x_{pa}c=2\pi\rho U^2\left[R\right]\begin{bmatrix}\frac{U}{b}c_2 & c_1\end{bmatrix}\begin{bmatrix}x_{pa}\\ \dot{x}_{pa}\end{bmatrix} \tag{4-20}$$

Writing the equations of motion of the system again with the above manipulations, Eq. 4-7 can be written as,

$$\left[\left[M\right]-\left[M_{nc}\right]\right]\begin{bmatrix}\ddot{h}\\ \ddot{\alpha}\end{bmatrix}+\left[-\left[B_{nc}\right]-\left[B_c\right]\right]\begin{bmatrix}\dot{h}\\ \dot{\alpha}\end{bmatrix}+\left[\left[K\right]-\left[K_c\right]\right]\begin{bmatrix}h\\ \alpha\end{bmatrix}=\left[D\right]\begin{bmatrix}x_{pa}\\ \dot{x}_{pa}\end{bmatrix} \tag{4-21}$$

By defining;

$$\begin{aligned}\left[M\right]&=\left[\left[M\right]-\left[M_{nc}\right]\right]\\ \left[B\right]&=\left[-\left[B_{nc}\right]-\left[B_c\right]\right]\\ \left[K\right]&=\left[\left[K\right]-\left[K_c\right]\right]\end{aligned} \tag{4-22}$$

as mass, damping and stiffness matrices and the state equation for the whole system can be written using Eq. 4-18 and Eq. 4-21 as follows:

$$
\begin{aligned}
&[M]\begin{bmatrix}\ddot{h}\\ \ddot{\alpha}\end{bmatrix}+[B]\begin{bmatrix}\dot{h}\\ \dot{\alpha}\end{bmatrix}+[K]\begin{bmatrix}h\\ \alpha\end{bmatrix}=[D]\begin{bmatrix}x_{pa}\\ \dot{x}_{pa}\end{bmatrix}\\
&\begin{bmatrix}\dot{x}_{pa}\end{bmatrix}=[E_1]\begin{bmatrix}h\\ \alpha\end{bmatrix}+[E_2]\begin{bmatrix}\dot{h}\\ \dot{\alpha}\end{bmatrix}+[F]\begin{bmatrix}x_{a1}\\ x_{a2}\end{bmatrix}\\
&xs1=\underline{q},\\
&xs2=\underline{\dot{q}},\\
&xs3=\underline{x_p},\\
&\dot{x}s2=\underline{\ddot{q}}=-[M]^{-1}[B]\underline{\dot{q}}-[M]^{-1}[K]\underline{q}+[M]^{-1}[D]\underline{x_p}
\end{aligned}
\tag{4-23}
$$

Then the aeroelastic system can be written in state space form as;

$$
\begin{bmatrix}\dot{x}s1\\ \dot{x}s2\\ \dot{x}s3\end{bmatrix}=\begin{bmatrix}\underline{0} & I & \underline{0}\\ -[M]^{-1}[K] & -[M]^{-1}[B] & [M]^{-1}[D]\\ [E_1] & [E_2] & [F]\end{bmatrix}\begin{bmatrix}xs1\\ xs2\\ xs3\end{bmatrix} \tag{4-24}
$$

4.2 Solution of the flutter equation

Equations of motion for the aeroelastic plant are constructed using linear approximations of aerodynamic lift and moment equations. The aeroelastic system is linear and time invariant. The state space representation of a linear time-invariant dynamic system is;

$$
\begin{aligned}
\dot{x} &= Ax + Bu\\
y &= Cx + Du
\end{aligned}
\tag{4-25}
$$

where A is the state matrix, B is the input matrix, C is the output matrix and D is the direct transmission matrix [18].

For the 2-dof aeroelastic model, whose equations of motion are derived in the previous section, system matrix A is given in Eq. 4-24. For the stability analysis only the system matrix is needed whereas for open

loop time domain simulations using state space techniques A, B, C, and D matrices should be known. B and C are defined as;

$$[B] = \begin{bmatrix} 0 \\ 1 \\ 0 \\ 0 \\ 0 \\ 0 \end{bmatrix} \quad (4\text{-}26), \qquad [C] = \begin{bmatrix} 1 & 0 & 0 & 0 & 0 & 0 \\ 0 & 1 & 0 & 0 & 0 & 0 \end{bmatrix} \quad (4\text{-}27)$$

which physically means that the input is given to angle of attack α by means of an actuator and the outputs are h and α which are the generalized coordinates.

Since there is no contribution of the input to the output of the system.

$$[D] = [0 \quad 0]^T \quad (4\text{-}28)$$

As stated, in the test setup, a NACA 0012 airfoil will be used. Mass and inertia properties of the airfoil are taken from the solid model prior to manufacturing for theoretical investigations and are used to construct the system matrix. The numerical value of the system matrix [A] for plunge stiffness value of K_h = 10,000 N/m, pitch stiffness value of K_α = 55.2 N.m/rad and air speed U=60 m/s is

$$[A] = \begin{bmatrix} 0 & 0 & 1 & 0 & 0 & 0 \\ 0 & 0 & 0 & 1 & 0 & 0 \\ 1{,}308 & 73 & -1 & 0 & 1{,}385 & 55 \\ 2{,}016.7 & 4758 & 4 & -12 & 9038 & 358 \\ 0 & 0 & 0 & 0 & 0 & 1 \\ 0 & 60 & 1 & 0 & -2184 & -138 \end{bmatrix} \quad (4\text{-}29)$$

Table 4 1: Mass and Inertia properties used in flutter equation.

Total Mechanism Mass (including motor, gearbox, casing, and upper casing)	27.85 kg
Airfoil and Shaft Mass	10.29 kg
a (ratio of the distance between the centerline and the elastic axis to the half chord length)	-0.6
x_α (ratio of the distance between the elastic axis and the center of gravity of the airfoil to the half chord length)	-0.5
b (half chord length)	0.15
K_α (Pitch Stiffness)	55.2 N.m/rad
K_h (Plunge Stiffness)	10,000 N/m
Airfoil and Shaft Inertia (about Elastic axis)	0.0509 kg.m²

Finding the flutter speed and flutter frequency of the system is an iterational procedure. The stability of the system is checked for values of air speed, from 1 m/s to 70 m/s, which is the maximum operational limit of AWT for flutter tests. A MATLAB® m-file is written for this purpose and open-loop poles of the system and the real parts of the open-loop poles of the system are plotted vs. air speed, U. The m-file is given in Appendix 1. In this m-file, one can enter different values of torsional and plunge stiffness values to see the effect of different stiffness value combinations of the system to flutter speed and flutter frequency.

For the NACA 0012 profile with chord length of 0.3 m and span of 0.6m, the open-loop poles and real parts of open-loop poles are plotted in Figure 4.2 and Figure 4.3, respectively. The elastic axis is 90 mm aft of the half chord and center of gravity is 15 mm aft of the half chord length. In other words, the ratio “a” is -0.6, and the ratio “x_α” is -0.5 according to

Theodorsen's notation. To solve the flutter equation other parameters such as the mass and inertia properties of the servo mechanism and the airfoil should be given. The mass in plunge motion includes the airfoil and the total mechanism mass whereas the mass and inertia properties in pitch degree of freedom is given by only the airfoil and the shaft connected to the airfoil. Note that the inertia properties of the airfoil and the connected shaft are taken about the elastic axis. Table 4.1 shows the mass properties of the mechanism and the airfoil with the shaft connected to the airfoil.

Figure 4.2 shows the loci of the open loop poles of the aeroelastic system for a plunge stiffness value of K_h = 10,000 N/m and a pitch stiffness value of K_α = 55.2 N.m/rad.

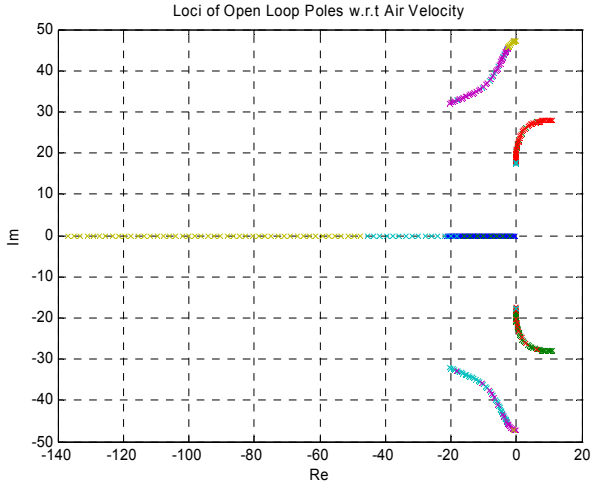

Figure 4. 2: Open-loop poles Locations as a Function of Air Speed**.**

The crosses indicate the iteration of the air speed. In other words, each cross is a value of the air speed. The air speed is incremented by 1 m/s from 1 m/s to 70 m/s, the poles are calculated and plotted Figure 4-3. When one of the poles shifts to right side of the imaginary axis, the aeroelastic system becomes unstable. The critical air speed can be calculated by bisection method. In Figure 4.3 it is seen that the system

becomes unstable between 32nd and 33rd iteration, meaning that critical flutter speed is between 32 m/s and 33 m/s. The calculated critical flutter speed is 32.4 m/s and the corresponding critical flutter frequency is 3.28 Hz.

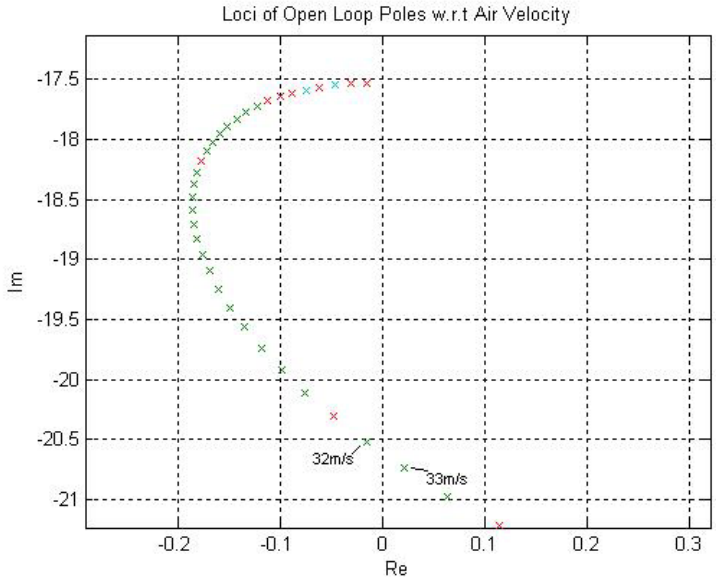

Figure 4. 3: The open loop poles shifts to the right side of the imaginary axis after 32 m/s..

4.3 Open loop response of the aeroelastic system

Below the critical flutter speed, the response of the system is bounded and damped. Above the critical flutter speed, the oscillations are unbounded. To graphically explain this phenomenon, a simple MATLAB® Simulink® model is constructed, and is given in Figure 4.4. The state space representation of the aeroelastic system is constructed for a specific air speed by an m-file which is given in Appendix 1.

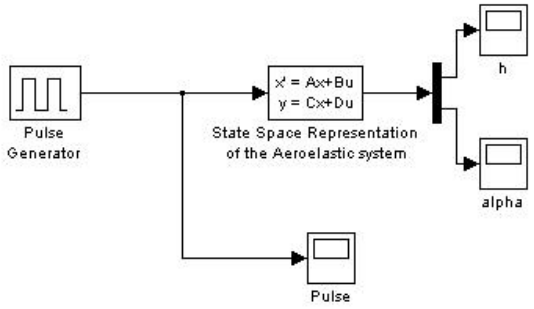

Figure 4. 4: Simulink® Model to observe the open loop responses of the aeroelastic system with different stiffness value combinations.

The open loop response of the aeroelastic system with various plunge and pitch degree of freedom stiffness values are given graphically through Figures 4.7 to 4.10. Table 4.2 show various pitch and plunge stiffness values for the same aeroelastic plant. Note that only stiffness properties are changed in every aeroelastic plant, mass and inertia as well as the position of the elastic axis with respect to the half chord length and center of gravity are kept the same since only the torsional and compression springs in the mechanism can be changed physically.

Table 4 2: Pitch and Plunge stiffness values for the same aeroelastic plant.

	Pitch Stiffness (N.m/rad)	Plunge Stiffness (N/m)
Plant 1	10,000	55.2
Plant 2	12,000	165.6
Plant 3	15,000	47.3
Plant 4	10,000	47.3
Plant 5	30,000	165.6

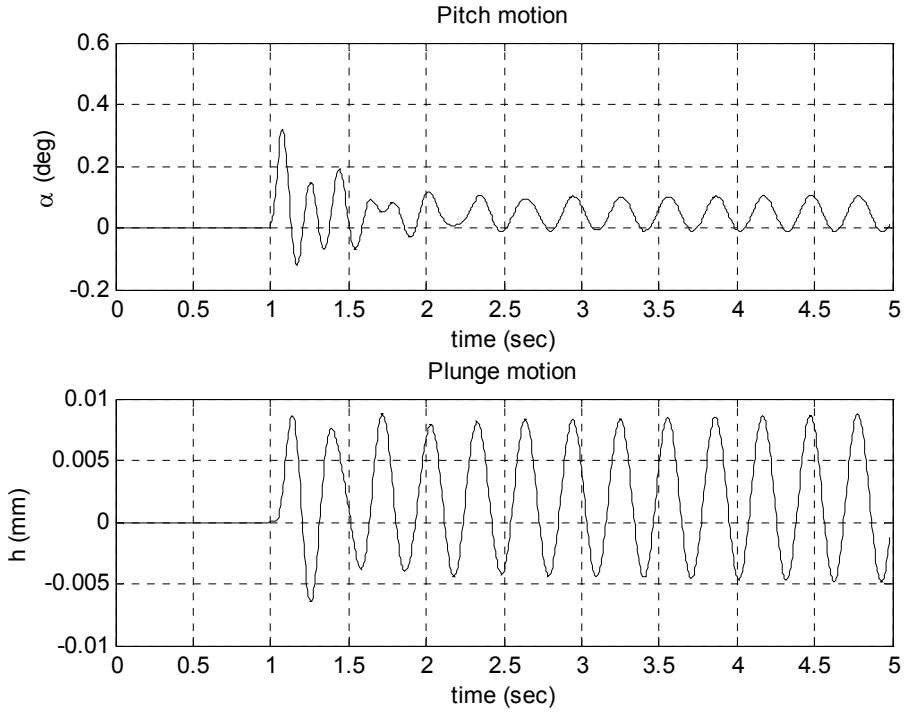

Figure 4. 5: Open loop impulse response of pitch and plunge motions of Plant 1 of Table 4.2 at U=31 m/s.

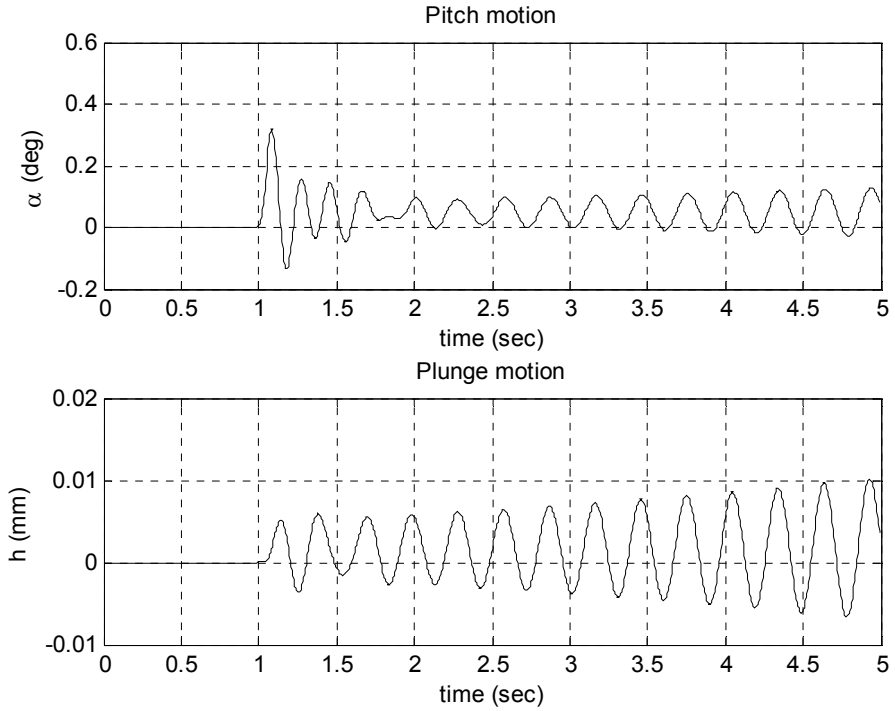

Figure 4. 6: Open loop impulse response of pitch and plunge motions of Plant 1 of Table 4.2 at U=34 m/s.

The open loop responses of the aeroelastic system below critical flutter speed are given in Figure 4.5 whereas the responses above critical flutter speed are given in Figure 4.6. It is seen that below critical flutter speed, the oscillations in plunge, h, and the oscillations in pitch, α are bounded and damped. On the other hand, above critical flutter speed, these oscillations are unbounded.

Open loop responses of Plant 2 to Plant 5 above their critical flutter speed are given in Figure 4.7 to Figure 4.10. Table 4.3 shows the critical flutter speed and critical flutter frequency for each plant.

Table 4.3: Critical flutter speed and frequency values for plants given in Table 4.2.

	Critical Flutter Speed (m/s)	Critical Flutter Frequency (Hz)
Plant 1	32.4	3.3
Plant 2	66.1	4.1
Plant 3	32	3.9
Plant 4	30.1	3.3
Plant 5	56.2	5.7

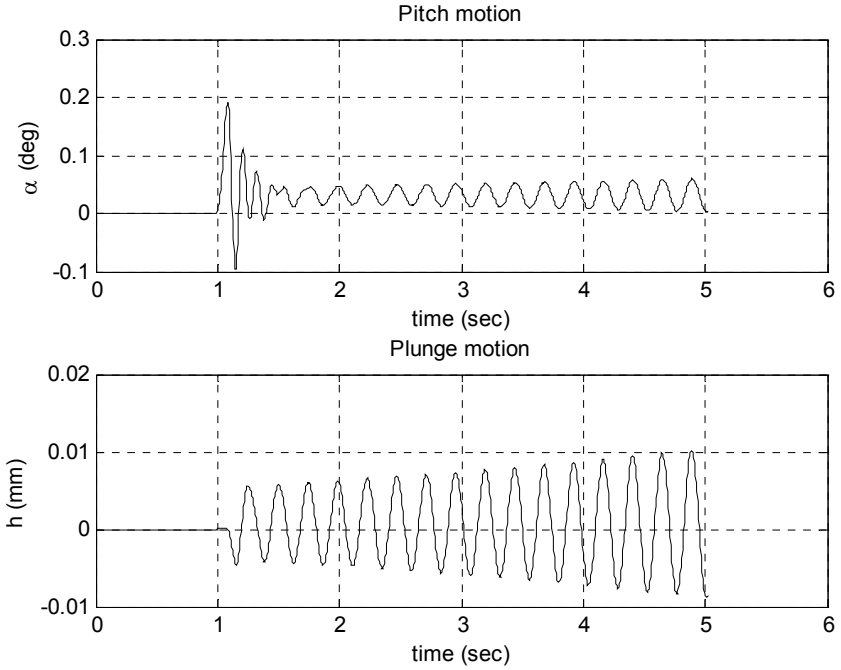

Figure 4. 7: Open loop impulse responses of pitch and plunge motions of Plant 2 of Table 4.2 at U=70 m/s.

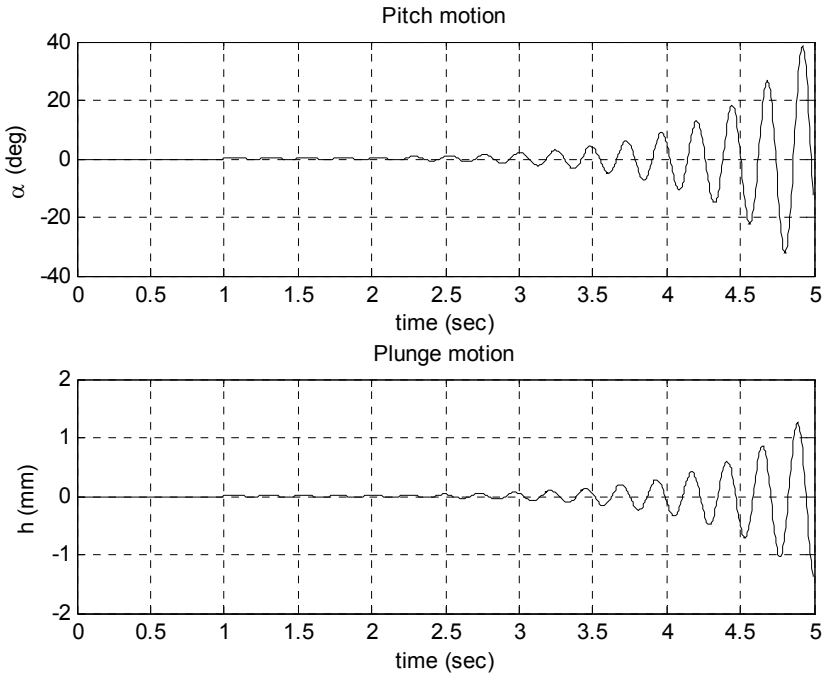

Figure 4. 8: Open loop impulse responses of pitch and plunge motions of Plant 3 of Table 4.2 at U=35 m/s.

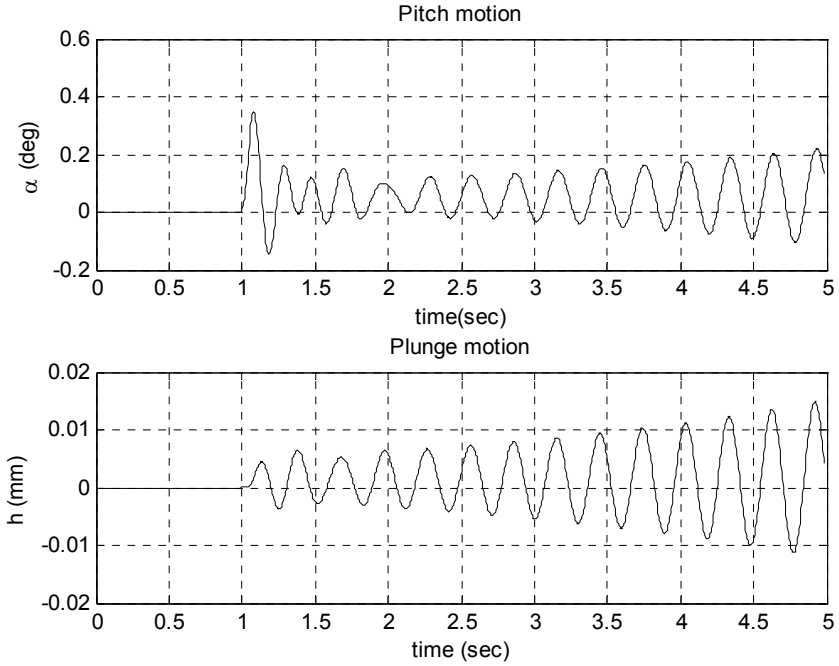

Figure 4. 9: Open loop impulse responses of pitch and plunge motions of Plant 4 of Table 4.2 at U=32 m/s.

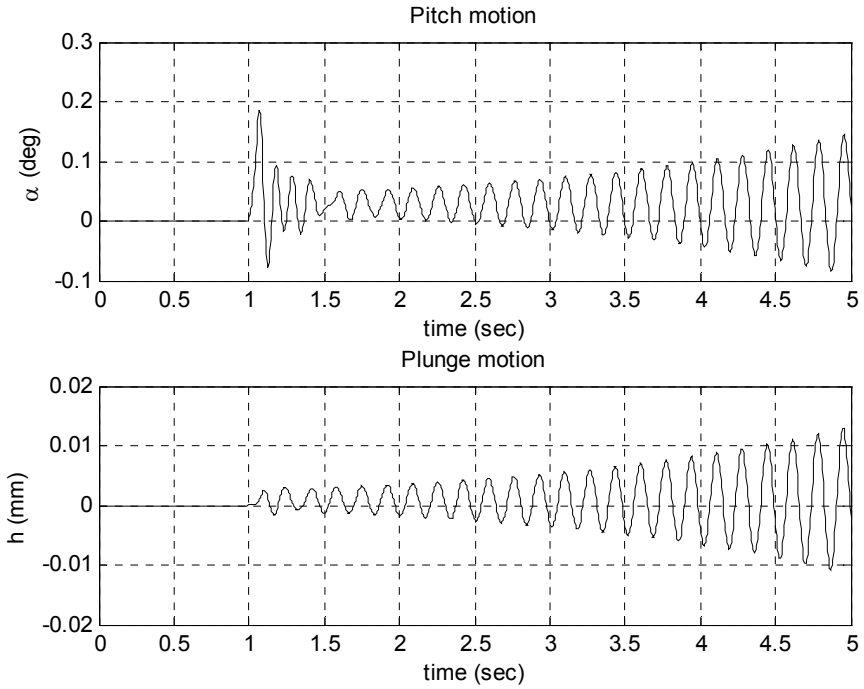

Figure 4. 10: Open loop impulse responses of pitch and plunge motions of Plant 5 of Table 4.2 at U=60 m.

4.4 Summary of the chapter

In this chapter, typical section is introduced for analysis of flutter phenomena and a mathematical model is constructed. Derivation of the aeroelastic system equations in state space is given in detail. By using the constructed aeroelastic mathematical model and the parameters set for the test setup, stability analysis of the aeroelastic system is carried out. Critical flutter speeds and frequencies are calculated for various stiffness characteristics combinations in pitch and plunge. Open loop impulse responses of the aeroelastic system are given to show that the system becomes unstable above the calculated theoretical critical flutter speeds for six different combinations of stiffness values in pitch and plunge.

CHAPTER 5

THE TEST SETUP

Conceptual design of the test setup starts with determining the aerodynamic loads on the airfoil and setting the bandwidth requirement for motor selection. Bandwidth requirement of the system is set as 50 Hz for 1º command input for flutter suppression. The maximum theoretical critical flutter frequency is calculated as 5.5 Hz and system bandwidth is set ten times this frequency. Mechanical design of the springs is followed by sensor selection and detailed design.

5.1 Motor Selection and Spring Design

The first step in designing the test setup is calculating the aerodynamic loads on the airfoil. The maximum aerodynamic lift and moment on the test setup can be calculated from steady lift and moment expressions for thin airfoils and are given as,

$$L_{\max} = -\frac{1}{2}\rho U^2 c l C_l \qquad \text{and} \qquad (5\text{-}1)$$

$$M_{\max} = L_{\max}\left(ba + \frac{1}{2}b\right) \qquad (5\text{-}2)$$

where C_l is the aerodynamic lift coefficient [19].

These lift and moment equations are linear in angle of attack and can be safely used up to ±15º for thin airfoils [19]. When angle of attack becomes too large, the flow starts to separate from the surface of the airfoil and the lift decreases [19]. The decrease of the lift coefficient of a NACA 0012 airfoil profile can be seen in Figure 5 in [20]. The NACA 0012 airfoil profile used in experiments have a chord length of c=0.3 m and a

span of l = 0.6 m. The maximum operational air speed of AWT for flutter experiments is 70 m/s. Then the maximum lift on the airfoil is calculated as 852.3 N and the maximum moment on the airfoil is calculated as 15.4 Nm. These loads are used as inputs for motor selection calculations. The motor will be used for flutter suppression and command tracking purposes for later studies. In this thesis, a servomotor is used to give disturbances as pulses, to initiate flutter above the critical flutter speed. The calculation for motor selection is given in Appendix 1. The instantaneous power requirement for the motor is given in Figure 5.1.

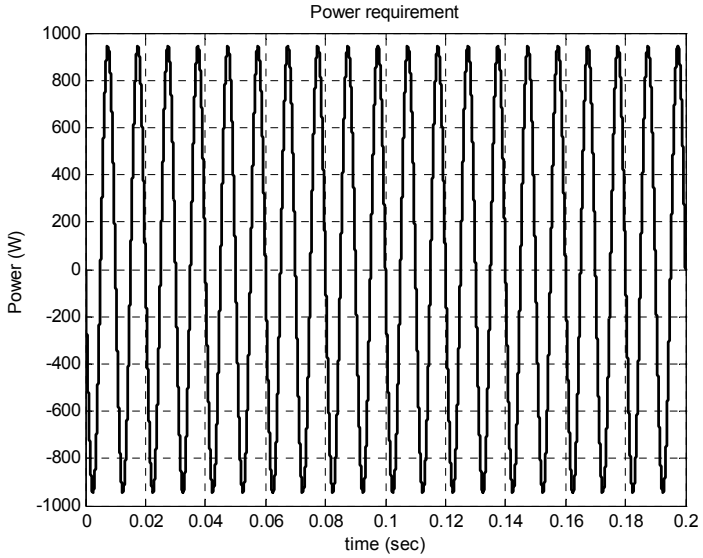

Figure 5. 1: The instantaneous power requirement for the motor.

The maximum power that the motor should give is about 900W. The motor selected is Kollmorgen® AKM42G has a rated power of 1.06kW and the motor is selected with brake to hold the airfoil shaft rigidly while there is no active control on the ATD. Some important properties of the selected motor are given in Table 5.1.

Table 5. 1: Parameters of the selected motor AKM42G.

Max. Mechanical Speed	6,000 rpm
Peak Torque	11.5 N.m
Rated Power	1.06 kW
Torque Constant, K_t	0.74 N.m/A_{rms}
Inertia	1.5 kg.cm^2
Brake Inertia	0.068 kg.cm^2
Viscous Damping, K_{dv}	0.013 N.m/krpm

In the test setup, the stiffness characteristics in both degrees of freedom are determined by a torsional spring in pitch degree of freedom, and two compression springs in plunge degree of freedom.

For designing the torsional springs, the maximum bending stress can be obtained by the expression;

$$\sigma = K\frac{32M}{\pi d^3} \tag{5.3}$$

where K is the stress concentration factor. Analytically determined K values for a round wire are;

$$K_i = \frac{4C^2 - C - 1}{4C(C-1)} \tag{5.4}$$

and

$$K_o = \frac{4C^2 + C - 1}{4C(C+1)} \tag{5.5}$$

where C is the spring index, D/d and the subscripts i and o stand for inner and outer fibers. K_i is used to determine stress rather than K_o, since K_o is always smaller than unity. Then the bending stress equation for a round-wire torsion spring becomes;

$$\sigma = K_i\frac{32M}{\pi d^3} \tag{5.6}$$

The deflection equation for a round-wire torsional spring is [21];

$$k = Fr / \theta = \frac{d^4 E}{64DN} \tag{5.7}$$

To determine the torsional spring constants to be used in the aeroelastic test setup, the dimensions, wire diameters, and active coil numbers should be physically manufacturable. The wire diameter for the torsional springs is chosen to be 8 mm, the outer diameter is chosen to be 40 mm and the maximum number of active coils is chosen to be 7. The design calculations of the torsional spring are given in an m-file in Appendix 1. Table 5.2 shows the number of active coils and the spring constants for the designed torsional springs.

Table 5. 2: Number of active coils and stiffness properties of the designed torsional springs

Number of Active Coils	Spring Constant (N.m/rad)
7	47.3
6	55.2
5	66.3
4	82.8
3	110.4
2	165.6

For designing the compression springs, the maximum shear stress which given by Eq. 5-8 can be used [21];

$$\tau = K_s \frac{8FD}{\pi d^3} \tag{5.8}$$

In Eq. 5-8 K_s is the shear-stress multiplication factor and is defined by the equation;

$$K_s = 1 + \frac{0.5}{C} \tag{5.9}$$

where C is the spring index given by the expression D/d. The deflection equation for a compression spring is [21];

$$k = \frac{d^4 G}{8D^3 N} \tag{5.10}$$

Again the physical properties of the compression spring should not restrict the manufacturing of the springs. The wire diameter of the compression spring is chosen to be 6 mm, the outer diameter is chosen to be 60 mm, the maximum number of active coils is chosen to be 6, and the minimum number of active coils is 2. The design calculations of the torsional spring are also given in the same m-file in Appendix 1. Table 5.3 shows the number of active coils and the spring constants for the designed compression springs.

Table 5. 3: Number of active coils and stiffness properties of the designed compression springs.

Number of Active Coils	**Spring Constant (N.m/rad)**
6	10,000
5	12,000
4	15,000
3	20,000
2	30,000

5.2 Mechanical Parts of the Test Setup

The test setup is composed of 6 different mechanical parts. They are the NACA 0012 airfoil, airfoil shaft, upper casing, casing, spring holders and linear guide interfaces. There are also non-designed parts on the test setup, which are four linear guides, two rolling bearings, a resolver, a linear scale and 4 accelerometers.

5.2.1 NACA 0012 Airfoil

The NACA 0012 airfoil profile is scaled such that the chord length is 300 mm and span length is 600 mm. An isometric view of the profile is given in Figure 5.2.

Figure 5. 2: NACA 0012 Airfoil.

The upper part of the airfoil is milled 280 mm deep with a certain profile for adjusting the center of gravity which is 15 mm in front of the half chord length. The elastic axis and center of gravity are essential parameters for flutter calculations. The elastic axis is placed 90 mm in front of the half chord length, 60 mm aft of the leading edge of the airfoil.

5.2.2 Airfoil Shaft

The airfoil shaft connects the airfoil to the torsional spring. It also holds the two rolling bearings to support the airfoil and the rotor of the resolver. An isometric view of the airfoil shaft is given in Figure 5.3.

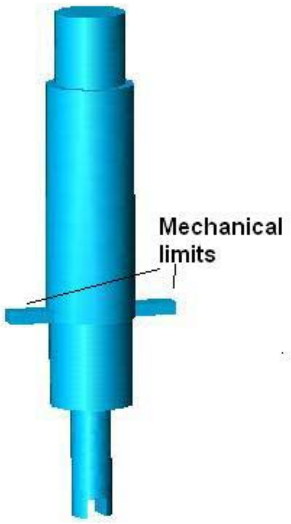

Figure 5. 3: Airfoil Shaft.

The upper part of the airfoil shaft is connected to the airfoil and the torsional spring is connected to the 8 mm slot in the lower part. The mechanical limits on the shaft are for restricting the rotational motion of the airfoil to ±15º. The rotor of the resolver is placed just above the slot of the torsional spring. Two rolling bearings are connected to the shaft below the mechanical limits. The detailed technical drawing of the airfoil shaft is given in Appendix 2.

5.2.3 Upper Casing

An upper casing holds the two rolling bearings that are connected to the airfoil shaft. It also has ±15º grooves that act as mechanical stops. An isometric view of the upper casing is given in Figure 5.4. It is connected to the casing with six M5 bolts. The detailed technical drawing of the upper casing is given in Appendix 2.

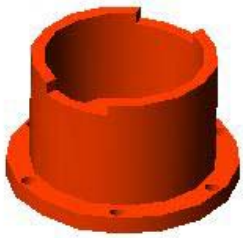

Figure 5. 4: Isometric view of the upper casing.

5.2.4 Linear Guide Interfaces

The test setup moves in plunge direction on 4 NSK LH30AN self-aligning linear guides. Linear guide interfaces are the parts that connect the linear guides to the casing. Linear guide interfaces are connected to the casing by three M8 bolts, and to each linear guide by two M8 bolts. One interface is connected to the front side of the casing and the other is connected to the back side. An isometric view of the linear guide interfaces is given in Figure 5.5. The technical drawing of the interfaces is given in Appendix 2.

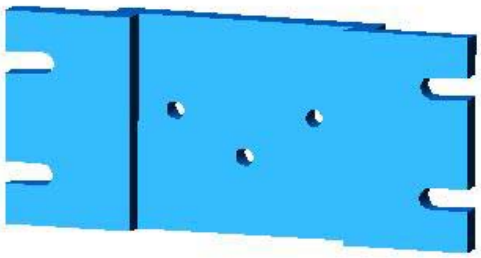

Figure 5. 5: Isometric view of the linear guide interface.

5.2.5 Spring Holders

Spring holders are connected to the chassis and holds the two compression springs which are placed between the casing and the spring holders. They are connected to the chassis by three M8 bolts and they also align the springs in their compression direction. An isometric view of

the spring holders is given in Figure 5.6. The technical drawing of the spring holder is given in Appendix 2.

Figure 5. 6: Isometric view of the spring holders.

5.2.6 Casing

Casing is the main frame of the test setup and all the mechanical components as well as the gearbox and the motor assembly, the stator of the resolver, and the ring of the linear scale is connected to this part. The motor and gearbox assembly is connected to the lower part of the casing by 8 M8 bolts. A shaft connected to the gearbox holds the torsional spring, whose other end is connected to the airfoil shaft. Compression springs are mounted in right and left sides of the casing, in the direction of plunge motion. The resolver is mounted on the upper part of the casing, where the upper casing is mounted. Linear guide interfaces connect the casing to the linear guides placed on the chassis (chassis is the mounting assembly that fixes the test setup to the wind tunnel ground). Two isometric views of the casing are given in Figure 5.7. The detailed technical drawing of the casing is given in Appendix 2.

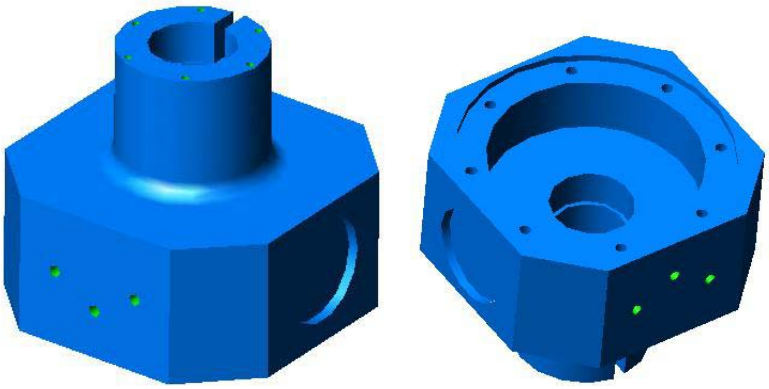

Figure 5. 7: Two isometric views of the casing.

Figure 5.8 shows the assembled test setup, and Figure 5.9 shows the exploded test setup.

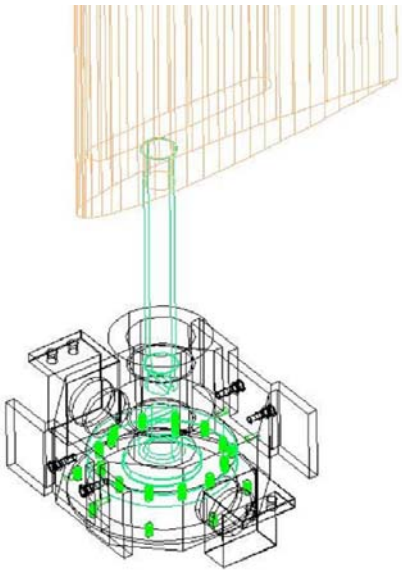

Figure 5. 8: Assembly of the test setup.

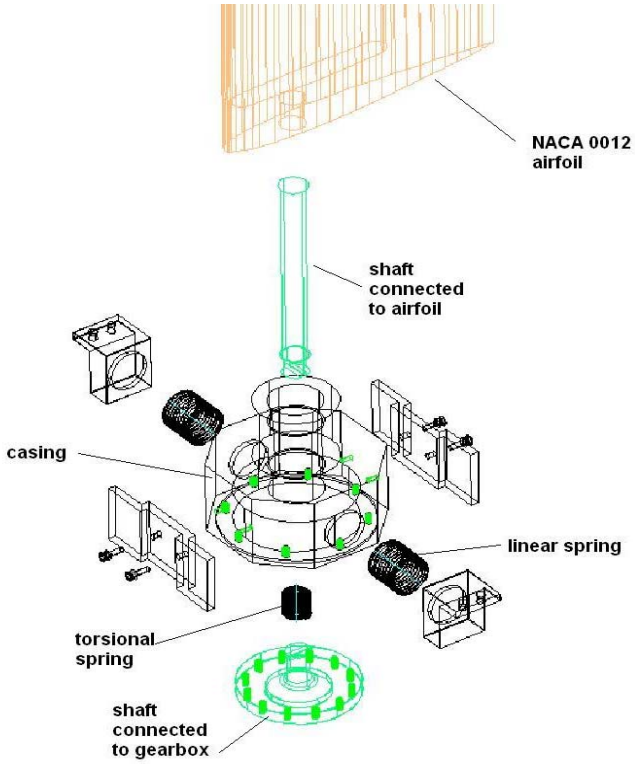

Figure 5. 9: Exploded view of the test setup.

5.2.7 Gearbox

The gearbox is directly connected to the motor shaft. A zero or very low backlash gearbox was chosen. Since the backlash introduces nonlinearity to the aeroelastic system, the measured critical flutter speed and critical flutter frequency would deviate from the calculated ones. Being free from backlash is the exclusive requirement for the choice of the gearbox. A gearbox ratio of N=29 is the smallest choice of the available ones, and is satisfactory considering the power requirements of the motor. The code number of the gearbox is Sumitomo Fine Cyclo's FC-A35-29 and its detailed data sheet is given in Appendix 2.

5.2.8 Linear Scale

A linear scale is used to measure the plunge motion of the test apparatus. It is composed of a fixed body with a magnetic rod of 100 mm

and a ring that moves with the casing. It produces analog output between 0V-10V. 0V corresponds to zeroth mm of the measuring range and 10V corresponds to the 100th mm of the measuring range. The selected linear scale is LenordBauer's GEL176 A 0100 A. The detailed datasheet of the linear scale is given in Appendix 2.

5.2.9 Resolver

A pancake resolver is used to measure the pitch motion of the airfoil. Pancake configuration is chosen for eliminating gearbox use. Nearly all encoders have an output shaft and a gearbox is necessary to connect airfoil shaft and encoder shaft, which are not inline. Gearbox usage brings an additional and uncontrollable backlash source to the test setup. The selected resolver is LTN's RE-21-1-B71. The detailed datasheet is given in Appendix 2.

5.3 Modal Analysis of the Airfoil

The test apparatus is designed to flutter at certain flutter frequency range of 3.1 Hz to 5.5 Hz. These flutter frequency values are found by solving the flutter equation for the system at determined plunge and torsional stiffness values and within the air speed limits of the AWT. Uncoupled plunge natural frequencies of the system with certain stiffness values range from 2.9 Hz to 5 Hz and uncoupled torsional natural frequencies of the system with certain stiffness values range from 6 Hz to 11 Hz.

It is desired that the system's flutter behavior be determined by the stiffness of the compression and torsional springs, not by the elastic behavior of the airfoil. So the airfoil's 1st bending and 1st torsional natural frequencies should be well above the systems 1st uncoupled plunge natural frequency and 1st uncoupled torsional natural frequency. Before manufacturing the components of the test setup, these conditions must be satisfied.

For the modal analysis, a solid model of the airfoil with the shaft is made. The shaft is made of steel and in the analysis density of steel is taken as 7,810 kg/m³, Poisson's ratio of steel is taken as 0.3 and modulus of elasticity of steel is taken as 210 GPa. The airfoil is made of Aluminum and density of Aluminum is taken as 2,710 kg/m³, Poisson's ratio of Aluminum is taken as 0.3 and modulus of elasticity of Aluminum is taken as 70 GPa. The analysis is made by assuming that the shaft is constrained in all directions, the supporting bearing section. So the original shaft is cut from the location where the first bearing is placed for the simplicity of the analysis. The shaft and the airfoil are glued to each other at the connection area so that the displacements at this glued area are the same for the airfoil and for the shaft.

The analysis is run on ANSYS®. SOLID 187 elements are used and a total of 43,134 elements were obtained. The mode shapes up to 1,000 Hz are extracted since 1,000 Hz is well above the frequency range of interest and is high enough to see the first two or three mode shapes of the airfoil and the shaft connected to it.

The results of the first three modes can be seen in Figures 5-10 to 5-14.

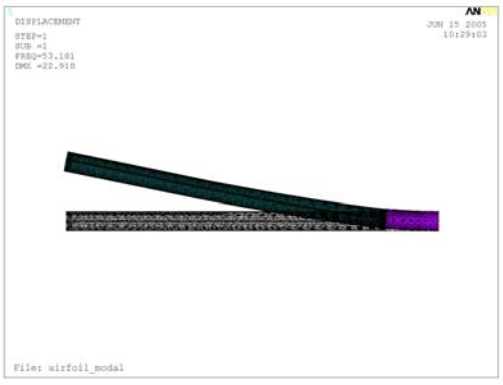

Figure 5. 10: 1st bending mode of the airfoil and the shaft @ 53.2 Hz.

It can be seen that the 1st mode of the airfoil and the shaft is bending mode at 53.2 Hz, which is associated with the uncoupled plunge natural frequency (2.9 Hz to 5 Hz). It can be concluded that the first bending mode of the airfoil is well above the 1st uncoupled plunge natural frequency of the system. Another view of this mode shape is given in Figure 5.11.

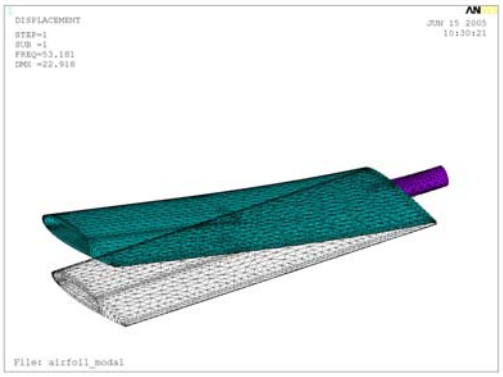

Figure 5. 11: 1st bending mode of the airfoil and the shaft @ 53.2 Hz., perspective view.

The second mode is again a bending mode of the airfoil, but in a perpendicular direction to the first bending direction, in the direction of the air speed.

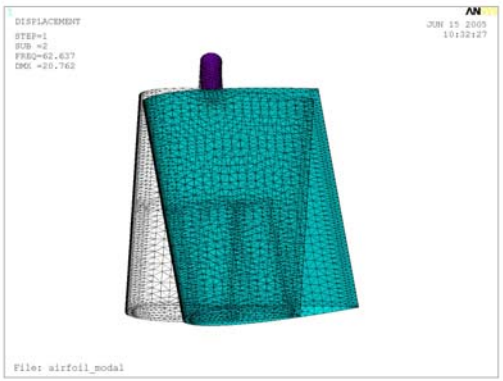

Figure 5. 12: 2nd Bending mode of the airfoil and the shaft @ 62.6 Hz.

But this second bending mode of the airfoil and the shaft is not associated with the flutter phenomena. The magnitude of the lift force does not change but the direction changes due to deformations on the shaft, but these deformations are small in amplitude so the lift force remains the same.

The first torsional mode shape is seen as the 3rd mode shape of the airfoil and shaft at 210.5 Hz.

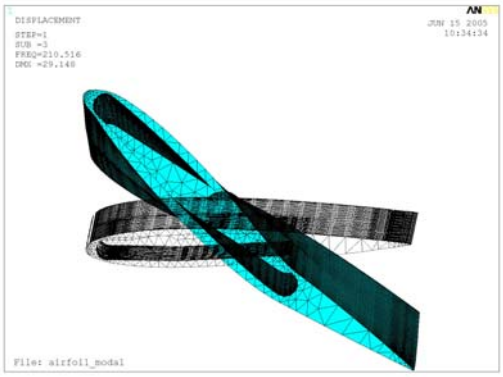

Figure 5. 13: 3rd mode shape of the airfoil and the shaft @ 210.5 Hz.

This torsional mode is associated with the uncoupled torsional natural frequency (6 Hz to 11 Hz). It can again be concluded that the first torsional mode of the airfoil and the shaft is well above the 1st uncoupled torsional natural frequency of the system. Another view of the mode shape is given in Figure 5.14.

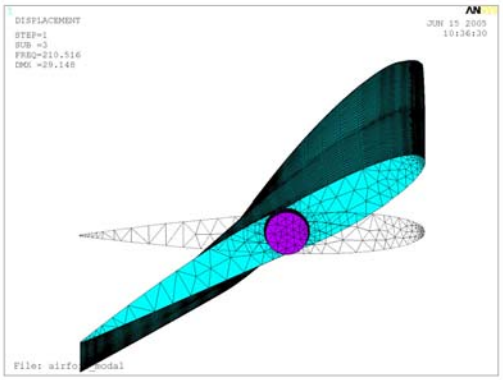

Figure 5. 14: 3rd mode shape of the airfoil and the shaft @ 210.5 Hz., perspective view.

The modal analysis revealed that the structural natural frequencies of the airfoil is different and well above the coupled natural frequencies of the test apparatus. It can be concluded that while conducting the experiments, the governing natural frequencies of the flutter phenomena are the plunge and torsional natural frequencies (determined by the changeable compression and torsional springs) of the test apparatus, not the 1st bending and 1st torsional natural frequencies of the airfoil.

5.4 Summary of the chapter

In the first part of this chapter, a detailed description of the design process of the test setup is given. Requirements for the servomotor and the motor selection calculatons are introduced. Also mechanical design of the compression and torsional springs, that are used to define the stiffness characteristics of the test setup, is given in detail. Parameters of the selected motor and stiffness values of the torsional and compression springs are given in tables. Later each part of the test setup are described with some illustrative solid model pictures. An exploded view of the test setup is also included. Detailed descriptions of the gearbox, the linear scale and the resolver are given. In the second part of this chapter, modal analysis results of the airfoil are given and it is concluded that the airfoil can be assumed as a rigid body.

CHAPTER 6

WIND TUNNEL EXPERIMENTS

6.1 Design of experiments in the wind tunnel

In the test apparatus, the use of 5 different compression springs with stiffness values of 10,000 N/m, 12,000 N/m, 15,000 N/m, 20,000 N/m and 30,000 N/m; and 6 different torsional springs with stiffness values of 47.3 Nm/rad, 55.2 Nm/rad, 66.3 Nm/rad, 82.8 Nm/rad, 110.4 Nm/rad and 165.6 Nm/rad is targeted in order to obtain flutter in different frequencies and speeds. The stiffness values of the compression and torsional springs are calculated in Chapter 5. This makes 30 experiments in total when every combination is considered. The critical flutter speeds and frequencies of these combinations are given in Appendix 3.

For a typical section, the flutter frequency and speed depend on 5 different, dimensionless system parameters [1], namely,

a	= the elastic axis location,
ω_h / ω_α	= the uncoupled bending-torsional frequency ratio,
$x_a = S / mb$	= the dimensionless static unbalance,
r_α	= the dimensionless radius of gyration,
$m / \pi \rho b^2$	= the density ratio.

For the test apparatus, only the uncoupled bending-torsional frequency ratio can be changed. All other parameters are constant since the airfoil, mechanism, motor etc. (e.g. all other components that define system parameters such as mass, inertia etc.) are kept constant.

The uncoupled bending-torsional frequency ratio ω_h / ω_α, is calculated for 30 different combinations of the springs. This calculation revealed that there are only eighteen combinations have different ω_h / ω_α ratio and twelve of thirty combinations are redundant for performing experiments.

Still 18 experiment combinations are considered to be too many. Hence a further elimination is needed. For this purpose, combinations with high ω_h / ω_α ratio are kept in experiments since systems having ω_h / ω_α ratio close to 1 are likely to flutter. Also for flutter suppression purposes, combinations with high stiffness values and combinations with low stiffness values can be chosen in order to compare the performance of the controllers.

6.2 Wind Tunnel Experiments

After the mechanical parts are manufactured, the test setup is assembled and instrumented in the wind tunnel. xPC Target Box® is used with MATLAB® for data acquisition and controller implementation. Aeroelastic Test Setup, ATD is fixed to the external balance system of AWT and all the mechanism except the airfoil remain under the wind tunnel floor. Figure 6.1 shows the ATD, the mechanism and the wind tunnel floor. The wooden tile on the surface of the wind tunnel floor is removed for a better view of the placement of the ATD.

Figure 6. 1: The ATD placed in the wind tunnel.

Figure 6. 2: The ATD viewed from under the wind tunnel ground.

Two grooves on the airfoil are milled for placement of accelerometers and cables connected to the accelerometers. For smoothness of the airfoil surface, the grooves are filled with wax. Figure 6.2 shows the ATD and the chassis that is designed to fix the ATD on the external balance mechanism. The chassis is welded to the ground. Also all motor connections, resolver and linear scale connections can be seen in Figure 6.2. Orientation of the airfoil with respect to the wind tunnel centerline is given in Figure 6.3.

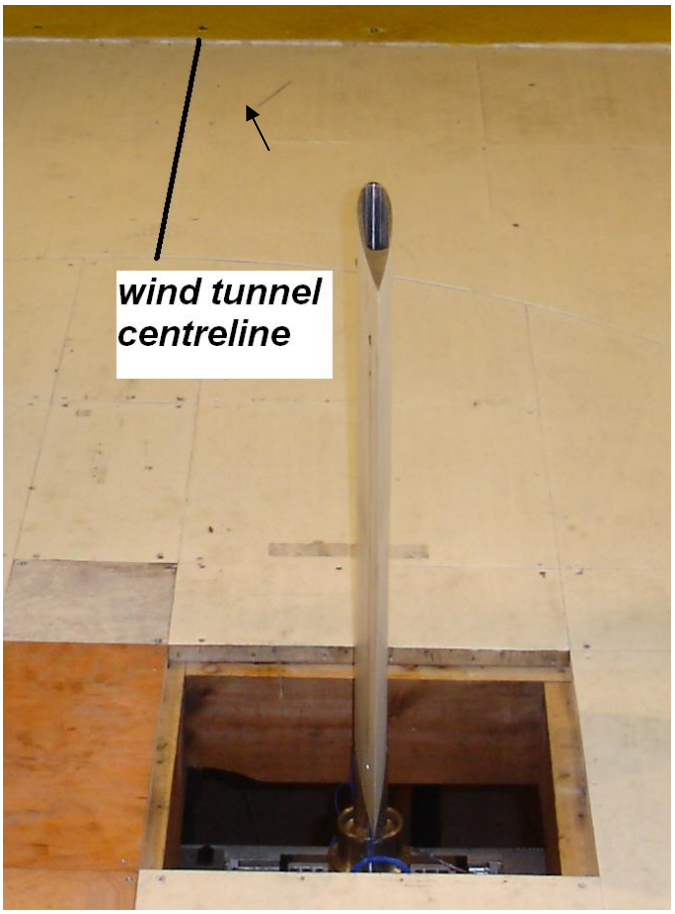

Figure 6. 3: Orientation of the airfoil with respect to the wind tunnel centerline.

A National Instruments's PCI 6031E analog input and output module is used for data acquisition and motor driving purposes through xPC Target®. Accelerometers are connected to a signal conditioner and the outputs of the signal conditioner are connected to the analog input module. Since the linear scale data is analog, it is also connected to the analog input module. Figure 6.4 shows the input module and connected input connections.

Figure 6. 4: National Instruments' PCI 6031E Analog Input Module.

A Kollmorgen® Servostar 620 digital servo amplifier is used to drive the motor. The motor is controlled by current control and the calculated current commands are transmitted to the digital servo amplifier via analog output module. Input command to the digital servo amplifier is given as analog voltage by xPC Target® to the analog input of the digital servo amplifier while it is in "Analog Torque Mode". The command input voltage is converted to current inside the digital servo amplifier. The scaling of the digital servo amplifier is such that the digital servo amplifier can give 20A

of current at 10V current command. The feedback element for the motor is a resolver packaged into the motor. The digital servo amplifier gives the angle of the motor shaft as simulated encoder output. Resolver to digital conversion is made within the amplifier and the angle is emulated. For reading the encoder emulation output, Measurement Computing's PCI-QUAD04 incremental encoder board is used. The incremental encoder output of the digital servo amplifier has a resolution of 4096 pulses per revolution. Although resolver-to-digital converter was not used to acquire the measured resolver data results, the resolution of the encoder emulation output of the digital servo amplifier is sufficient.

For reading data from the resolver, that is used to measure the airfoil and airfoil shaft angle, another digital servo amplifier, Kollmorgen Servostar 603 was used. Figure 6.5 shows the digital servo amplifiers.

Figure 6. 5: Kollmorgen® Servostar 620 and Kollmorgen® Servostar 603 digital servo amplifiers.

After completing the instrumentation and mechanically assembling the ATD completely in the wind tunnel, first experiment is conducted with a plunge stiffness of 30,000 N/m and pitch stiffness value of 47.3 N.m/rad combination. Although the air speed is increased up to 74.7 m/s, the pulse response of the airfoil and the airfoil shaft are all damped at all air speeds. Figure 6.6 shows the damped oscillations in pitch and plunge degree of freedom at 74.7 m/s.

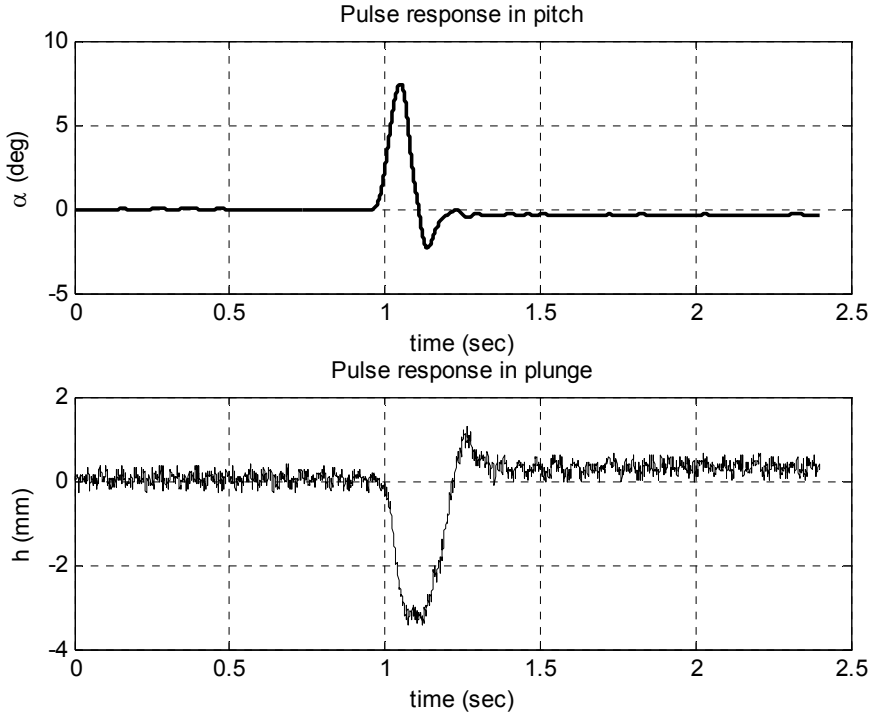

Figure 6. 6: Damped oscillations at 74.7 m/s

These damped oscillations show that the damping of the system is too high. The calculated critical flutter frequency and critical flutter speed for the combination of plunge stiffness 30,000 N/m and pitch stiffness 47.3 N.m/rad is 5.3 Hz and 40.4 m/s. The experiment reveals that the damping sources of the test setup are considerably dominant and calculating the critical flutter frequency and speed without damping is a wrong

assumption. The damping ratio in each degree of freedom can be calculated from the measured data using the logarithmic decrement method as

$$\delta = \frac{1}{n}\ln(\frac{X_i}{X_{i+n}}) \tag{6.1}$$

The logarithmic decrement is the ratio of the magnitudes of the oscillations in each cycle. ζ value can be calculated as

$$\zeta = \frac{\delta}{\sqrt{\delta^2 + 4\pi^2}} \tag{6.2}$$

The calculated damping ratio for plunge motion is ζ_h=0.21 and the calculated damping ratio for pitch motion is ζ_α=0.36.

A sinesweep test was run on the ATD without running the wind tunnel for determining the natural frequencies of the test setup. An input is given from the motor from 1 Hz to 15 Hz with magnitude of 6º at the airfoil shaft and the responses in pitch and plunge degrees of freedom are plotted. Figures of responses in both degrees of freedom in the sinesweep test conducted before the modifications are given in Appendix 4.

Further investigations on problems in the test setup revealed that the torsional spring's active wires are sliding on each other, restricting the motion of the spring, therefore creating a source of friction. The first torsional spring has a stiffness of 47.3 Nm/rad and has 7 active wires. The torsional spring is also touching the wall of the casing. These problems are caused by improper manufacturing of the torsional spring. The linear guides are a source of friction in plunge degree of freedom. Sufficient energy to overcome the stick-slip friction due to the linear guides, cannot be transferred from pitch degree of freedom to plunge degree of freedom, which is necessary for flutter to occur.

The friction problem in pitch degree of freedom is solved by carefully manufacturing another torsional spring, but this time with a theoretical stiffness value of 55.2 Nm/rad, which has 6 active wires with spacing between each active wire. Therefore the active wires would not slide on each other. Also the wall of the casing is widened so that the torsional spring would not touch the casing. The grease inside the rolling bearings was removed with a solvent. Removing the grease in the linear guides would reduce the friction force, but it is observed that linear guides do not function properly without grease. So experiments are conducted with the available linear guides.

After completing the improvements, the pulse response of the airfoil is examined again. This time, a combination of plunge stiffness of 10,000 N/m, and pitch stiffness of 55.2 N.m/rad are used in the ATD. Figure 6.7 shows both the pitch response and plunge response to 5º pulse given to the airfoil. The oscillations are damped again settling time is much longer than the previous system before modifications in pitch degree of freedom. This shows that the friction problems are highly eliminated in pitch degree of freedom. However there is still considerable friction in plunge degree of freedom. The pulse with magnitude of 5º is given to the airfoil without airflow on the airfoil; i.e., at 0 m/s.

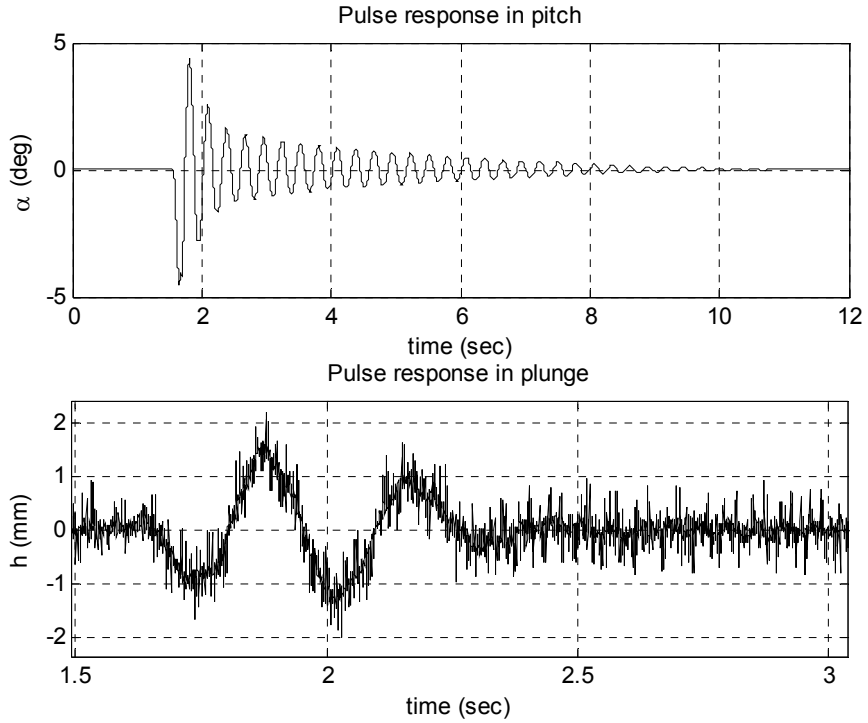

Figure 6. 7: Pulse response of pitch angle and plunge displacement at 0 m/s, after improvements.

Figure 6.7 reveals that the friction problem of the linear guides still remains. The oscillations in plunge degree of freedom are highly damped. After improvements, the new damping ratio of plunge motion is calculated as ζ_h=0.14 and the new damping ratio for pitch motion is calculated as ζ_α=0.08, again by using the logarithmic decrement method. It is seen that the improvements to reduce friction worked.

The theoretical flutter calculations are made assuming no damping in the setup. Therefore, a new set of calculations are needed including damping terms. For this purpose, the MATLAB® code for flutter calculations is modified and damping terms are included in the system matrix. With damping ratios given above, theoretical critical flutter speed is calculated as 45.7 m/s and the critical flutter frequency is found as 3.9 Hz. The modified MATLAB® code can be found in Appendix 1.

The sinesweep test after the improvements to the setup is repeated without running the wind tunnel for determining the natural frequencies of the test setup. This time input is given from the motor from 1 Hz to 15 Hz with magnitude of 2º. This sinesweep test is performed two times on the ATD; one started from 1 Hz and finished at 15 Hz, the other started from 15 Hz and finished at 1 Hz. The graphs of these new sinesweep tests can be found in Appendix 4. Using the data acquired in the low to high and high to low sinesweep tests, the frequency response of the pitch angle and the plunge displacement to motor input are estimated using MATLAB®'s transfer function estimate command "tfestimate". Figure 6.8 and Figure 6.9 shows frequency responses in both degrees of freedom.

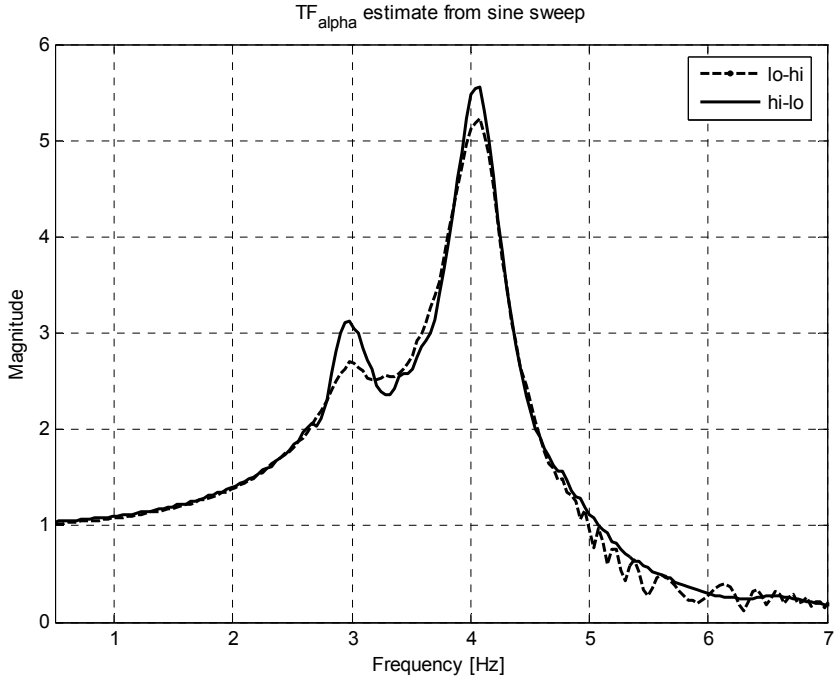

Figure 6. 8: Frequency response of the pitch angle to motor input.

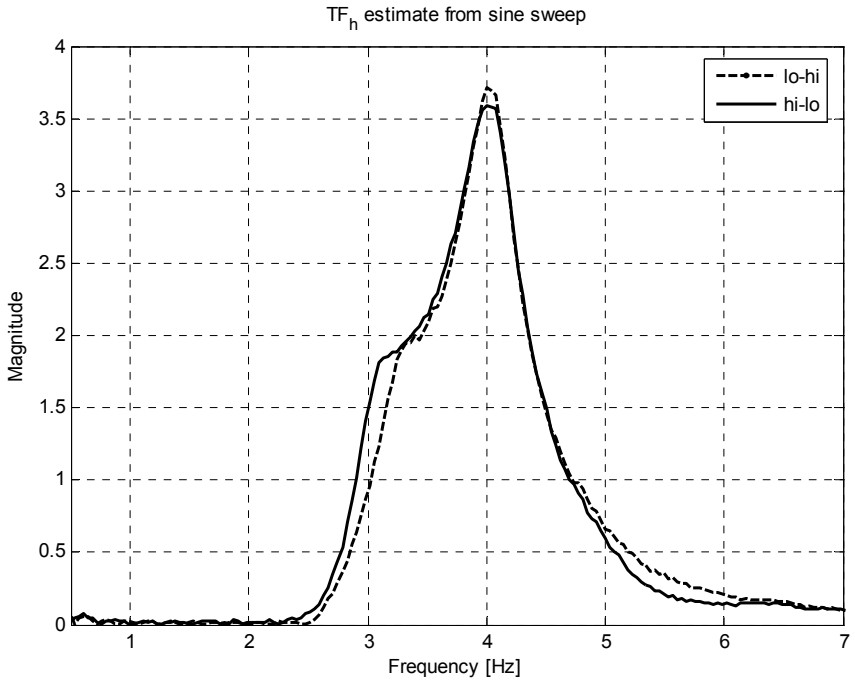

Figure 6. 9: Frequency response of the plunge displacement to motor input.

Figure 6.8 and 6.9 show the natural frequencies of the system in both degrees of freedom. One is about 3 Hz., and the other is about 4 Hz. The frequency shift in both graphs may result from the nonlinearities in the ATD in both pitch and plunge degrees of freedom. It is also seen that the energy transferred to plunge degree of freedom is so low that the magnitude in plunge motion is nearly zero, i.e.; no motion in plunge is observed up to 2.5 Hz.

With this configuration, wind tunnel experiments are started again. 6 different runs are made with the same pitch and plunge stiffness values of 55.2 Nm/rad and 10,000 N/m, respectively. The observations made during the experiment are given in Appendix 3.

In the first experiment, air speed is increased by nearly 10 m/s increments, and 3 consecutive 2º pulses are given to the airfoil at 10 m/s, 20 m/s, 25 m/s, 30 m/s, 39.2 m/s, 50 m/s and 60.6 m/s. Below 60.6 m/s,

the oscillations are damped and the setup do not flutter. The pulse responses in pitch and plunge degrees of freedom of the system at 10 m/s, 20m/s, 30 m/s, and 40 m/s together with the pulse input comment and motor angle are given in Figure 6.10 to Figure 6.13.

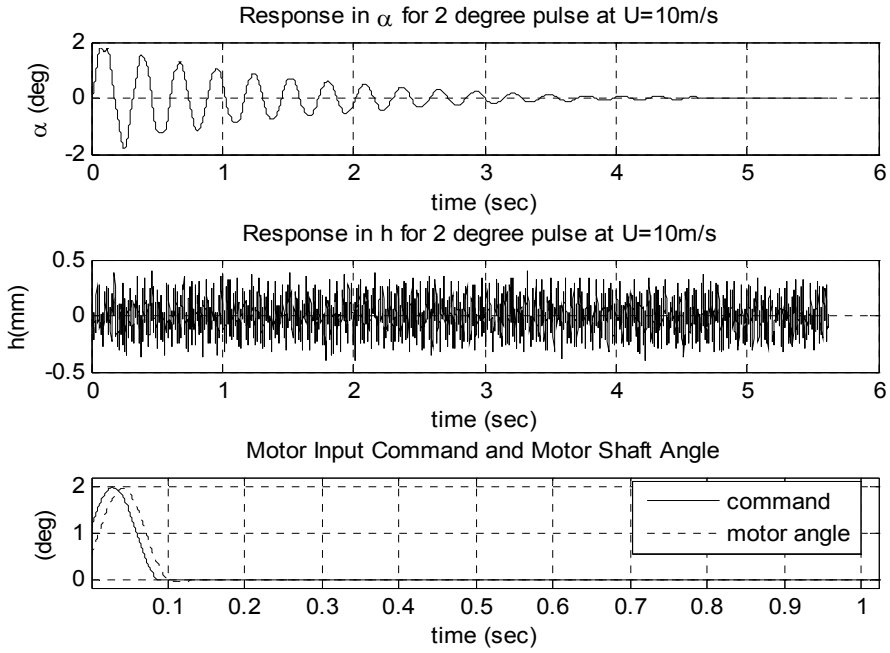

Figure 6. 10: Pulse responses in each degree of freedom, motor command and motor angle at U=10 m/s.

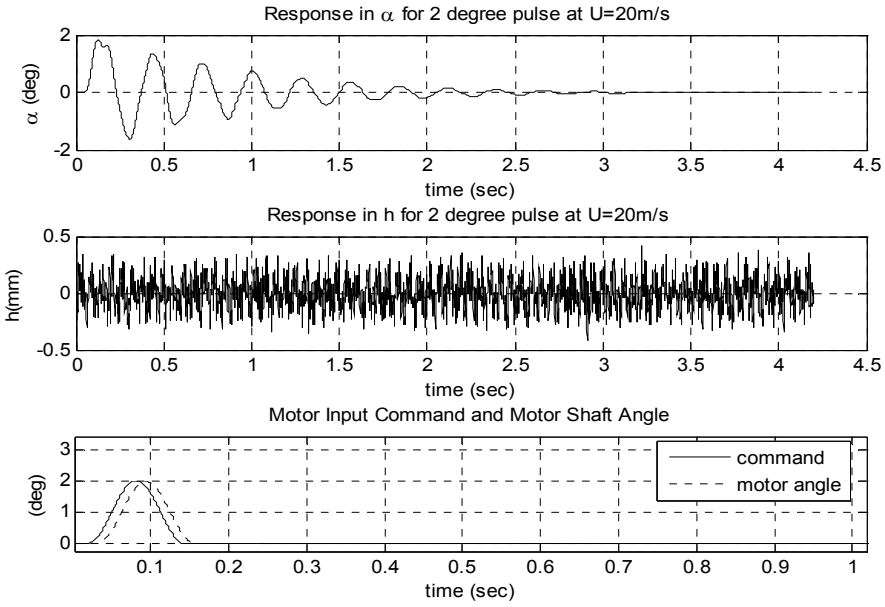

Figure 6. 11: Pulse responses in each degree of freedom, motor command and motor angle at U=20 m/s.

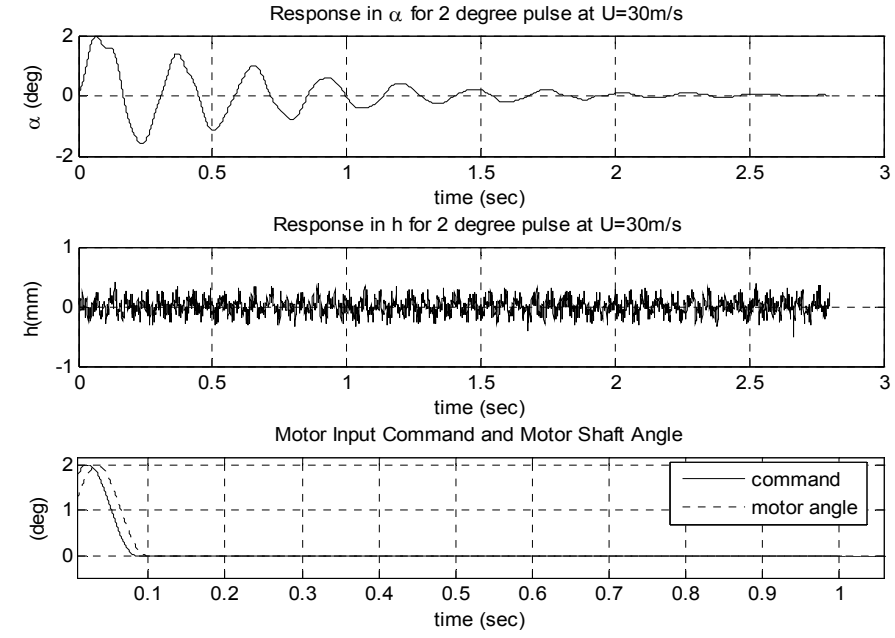

Figure 6. 12: Pulse responses in each degree of freedom, motor command and motor angle at U=30 m/s.

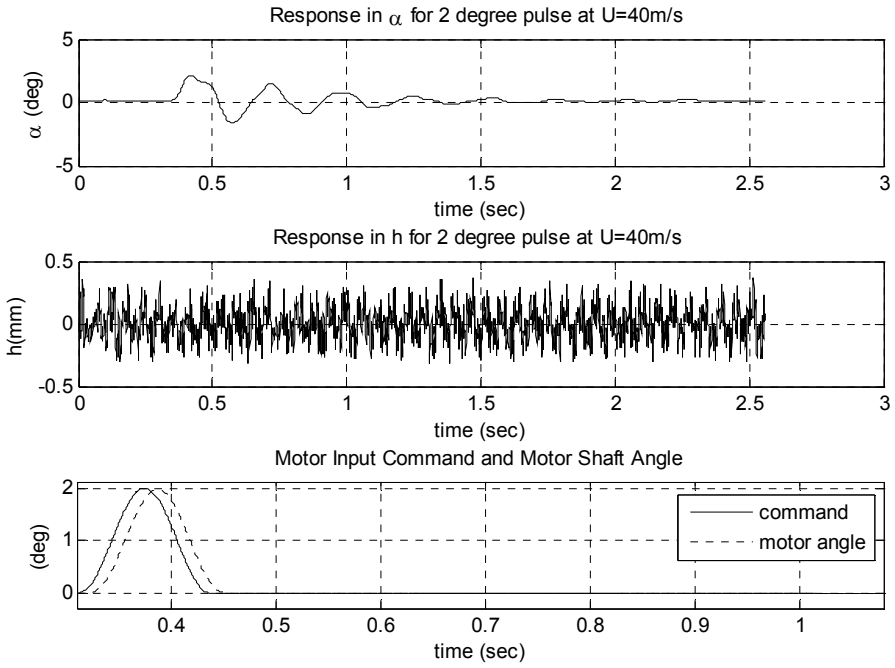

Figure 6. 13: Pulse responses in each degree of freedom, motor command and motor angle at U=30 m/s.

From the above graphs, it is seen that the settling time of the oscillations in pitch degree of freedom decreases as the air speed increases. This shows that the aerodynamic damping increases as the air speed increases. The aerodynamic damping increases and then decreases as the air speed approaches the critical flutter speed [1]. Therefore it can be concluded that the setup will flutter at a speed above 40 m/s. By determining the slope of the damping curve in a U-g graph, critical flutter speed can be determined. No motion is observed in the plunge degree of freedom because the amplitude of the pulse (2º amplitude) is too low for energy to be transferred to plunge motion.

The measurement from the linear scale is too noisy, and Figure 6.14 shows the power spectral density of the measured noise in linear scale channel. It is seen that there are high frequency components. This

data was acquired while the wind tunnel was running and the set up was stationary. The electrical grounding in the wind tunnel has some problems, the servomotor was located near the linear scale and the wind is circulated in the wind tunnel by a very powerful electric motor, this noise may result from the magnetic interference of the motor. Also the servomotor in the mechanism may have magnetic interference on the linear scale measurement.

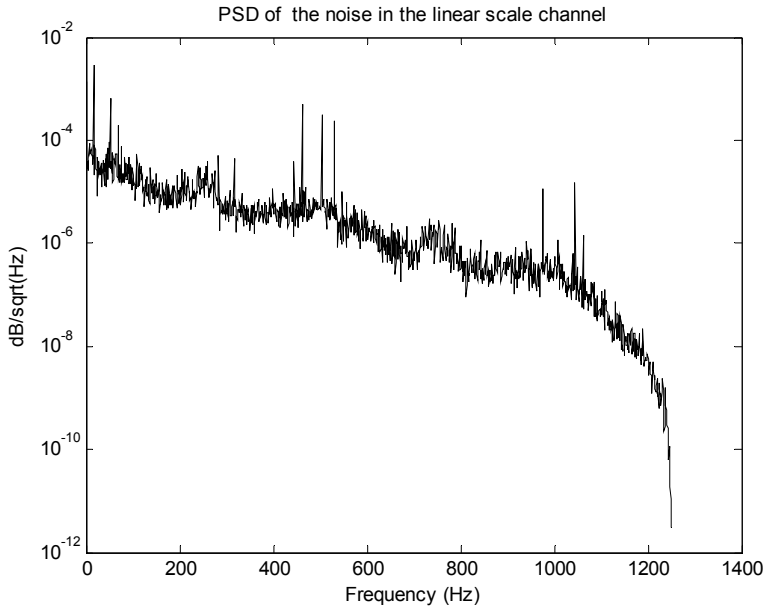

Figure 6. 14: Power spectral density of the data acquired from the linear scale channel.

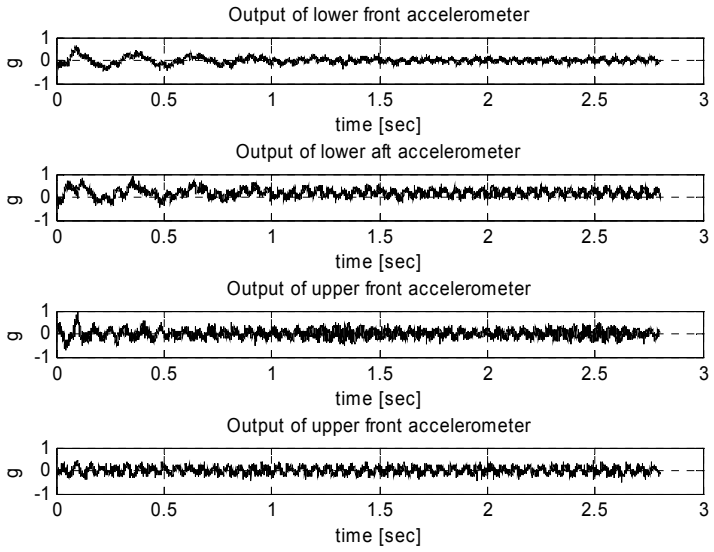

Figure 6. 15: Accelerometer measurements at U=30 m/s.

Four accelerometers are placed on the airfoil for further studies on flutter predictions from flight data. Measurements of the accelerometer outputs at 30 m/s are given in Figure 6.15 for demonstrational purposes. Accelerometer data obtained at 10 m/s, 20 m/s and 40 m/s are given in Appendix 4.

At 60.6 m/s air speed, the ATD went into flutter after giving a 5º degree pulse to the airfoil. In Figure 6.16, undamped oscillations in pitch and plunge degree of freedoms can be seen, respectively.

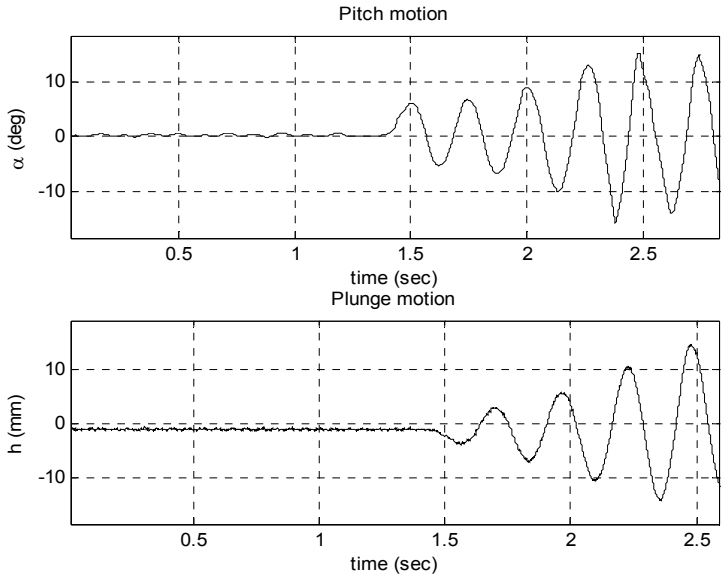

Figure 6. 16: Undamped oscillations in pitch and plunge degrees of freedom at 60.6 m/s.

The motion in the pitch degree of freedom is mechanically limited to ±15º.

In the second experiment, air speed is directly increased to 45 m/s, without disturbing the ATD, for finding the exact flutter speed. This time 6 consecutive pulses with magnitudes 1º to 6º are given to the airfoil. The resulting oscillations are damped. Then the air speed is increased to 47.5 m/s and the same pulses are given to the airfoil. The oscillations are still damped and no oscillations are observed in plunge degree of freedom. When the air speed reaches 53 m/s, after 6º pulse, the oscillations do not damp, but they are bounded. Limit cycle oscillations due to nonlinearities in the springs or backlash in the ATD are observed during the second experiment. During the limit cycle, oscillations in plunge degree of freedom are also observed. In Figure 6.17, limit cycle oscillations in pitch and plunge degrees of freedom at 53 m/s can be seen.

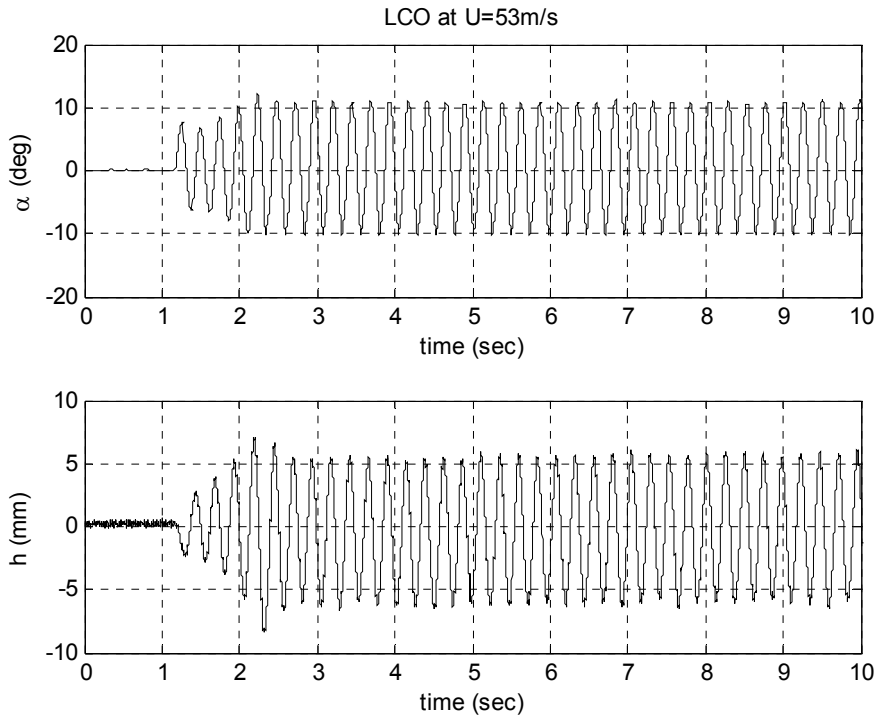

Figure 6. 17: Limit cycle oscillations in pitch degree of freedom at 53 m/s.

Note that the amplitudes of the oscillations are bounded to +10.7º/-10º in pitch degree of freedom. The difference of limit cycle oscillations from flutter oscillations is that the amplitudes of oscillations in limit cycle are bounded whereas the amplitudes of oscillations in flutter are unbounded. Both phenomena are destructive for airborne structures, but flutter is more predictable than limit cycle, because nonlinearities cannot be predicted precisely.

The limit cycle oscillations in pitch degree of freedom are more repeatable than in plunge degree of freedom. When the system is in limit cycle, pitch angle oscillates between the same boundaries whereas upper and lower boundaries in plunge motion vary with time. This may be due to the stick-slip friction characteristics of the linear guides on which the ATD is moving in plunge direction.

In the third, fourth and fifth experiments, the air speed are increased from 51 m/s to 60 m/s with 1m/s increments. In every experiment, limit cycle oscillations are observed and recorded. Observations during these experiments can be found in Appendix 3.

For better understanding the limit cycle phenomenon, FFT graphs of the limit cycle oscillations at 50 m/s, 51 m/s, 52 m/s, 53 m/s, 55 m/s, and 56 m/s are given in Figure 6.18 through Figure 6.24.

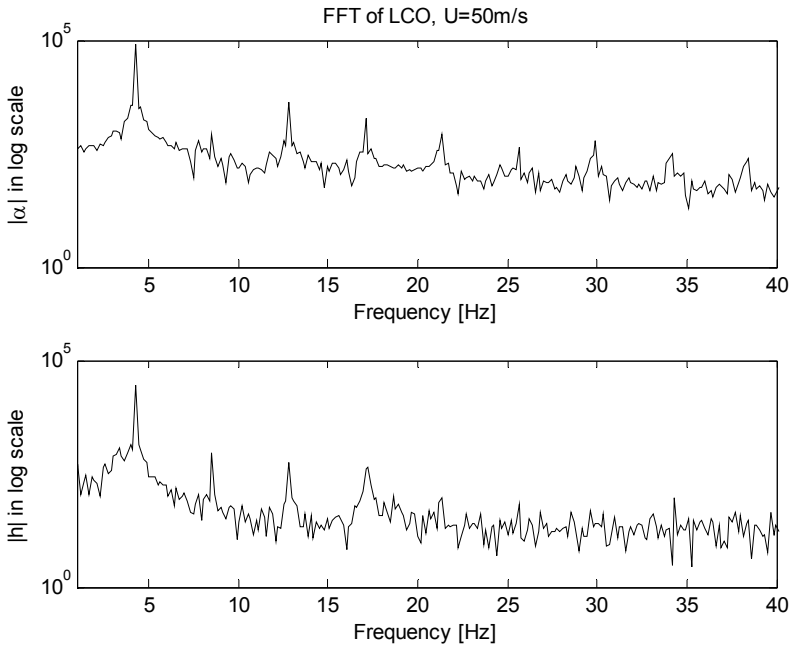

Figure 6. 18: FFT graph of limit cycle oscillations at U=50 m/s.

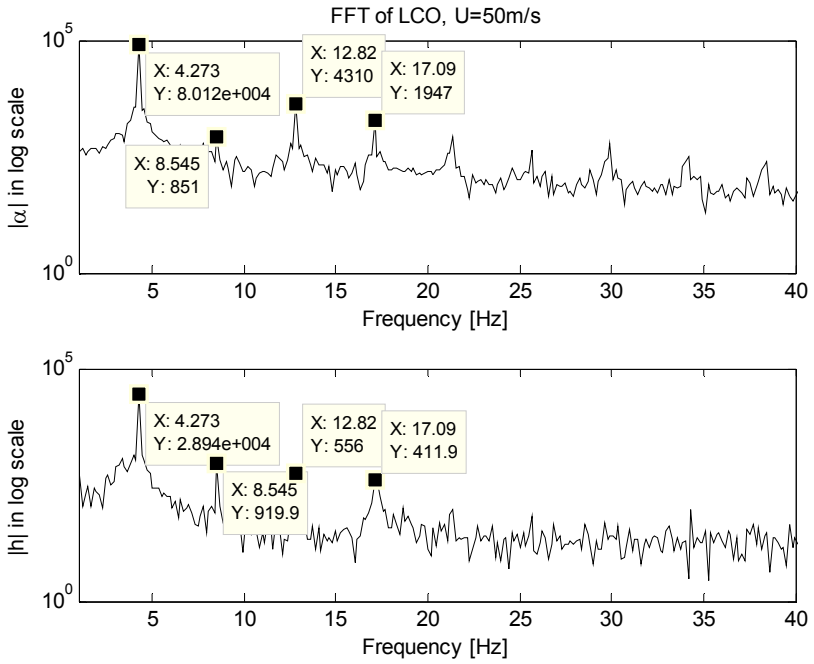

Figure 6. 19: FFT graph of limit cycle oscillations at U=50 m/s with peaks at distinct frequencies marked on the graph.

In Figure 6.21, multiple frequency contents of the limit cycle can be seen. There is motion in both pitch and plunge degrees of freedom. Higher harmonics are involved in the limit cycle oscillations. Also subharmonic components can be seen at 50 m/s and 51 m/s. Subharmonic components are more distinctive in plunge motion where nonlinearities due to stick-slip friction are dominant in motion. First four peaks are exactly at the integer scales of the fundamental frequency.

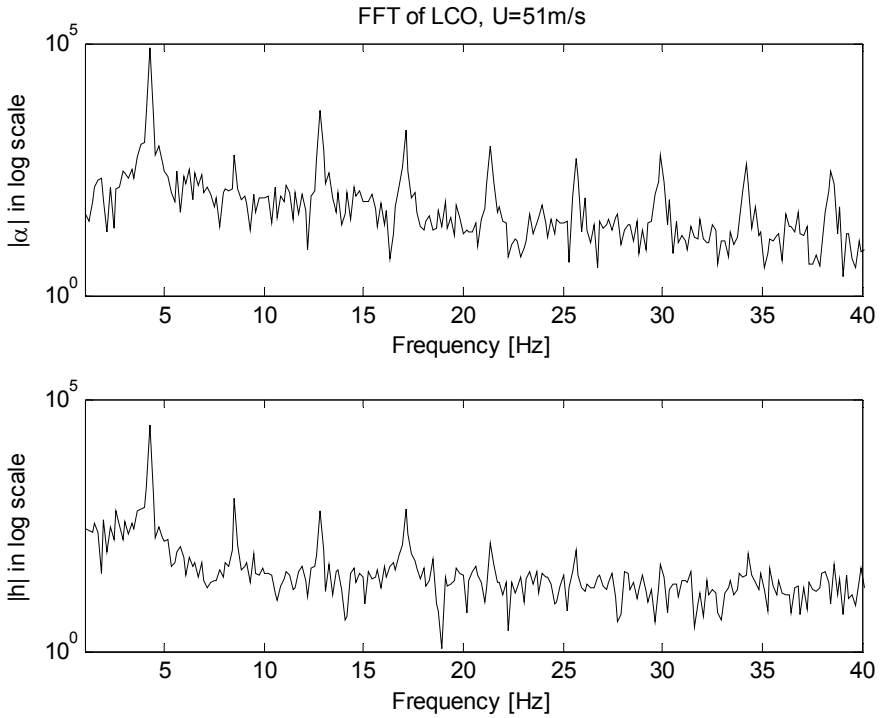

Figure 6. 20: FFT graph of the limit cycle oscillations at U=51 m/s.

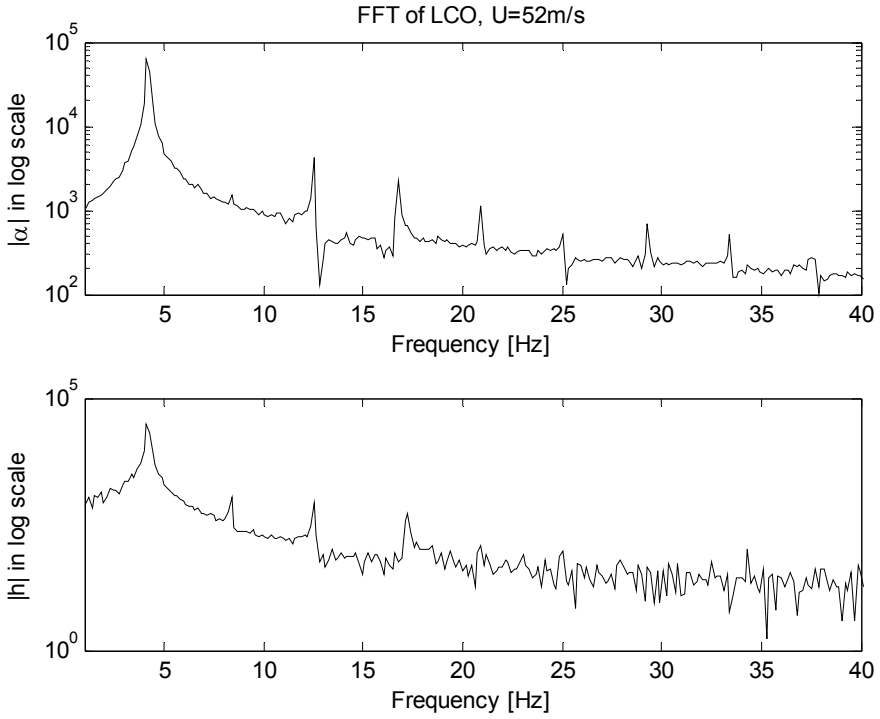

Figure 6. 21: FFT graph of the limit cycle oscillations at U=52 m/s.

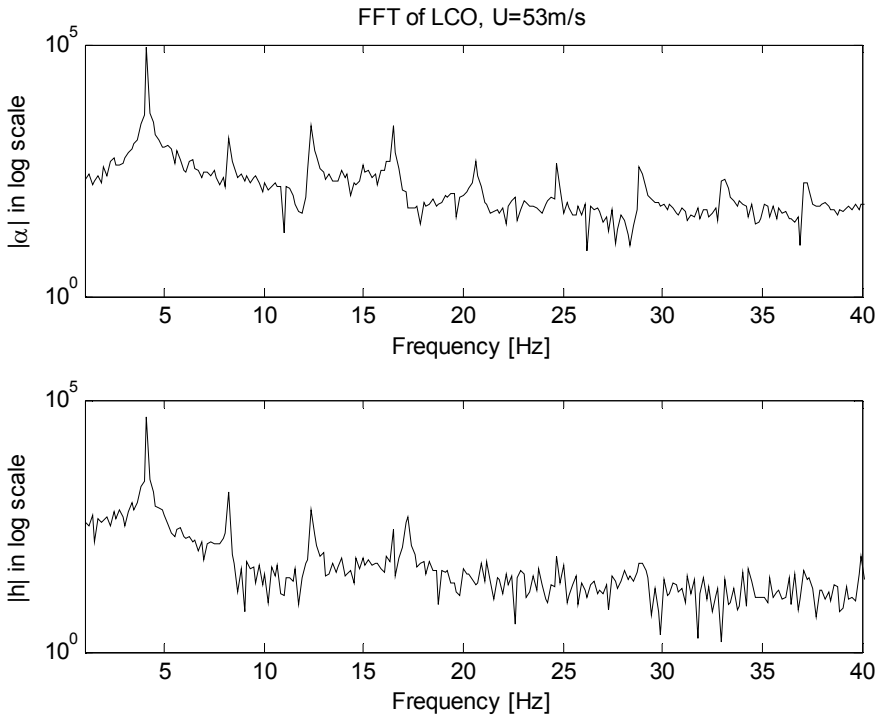

Figure 6. 22: FFT graph of the limit cycle oscillations at U=53 m/s.

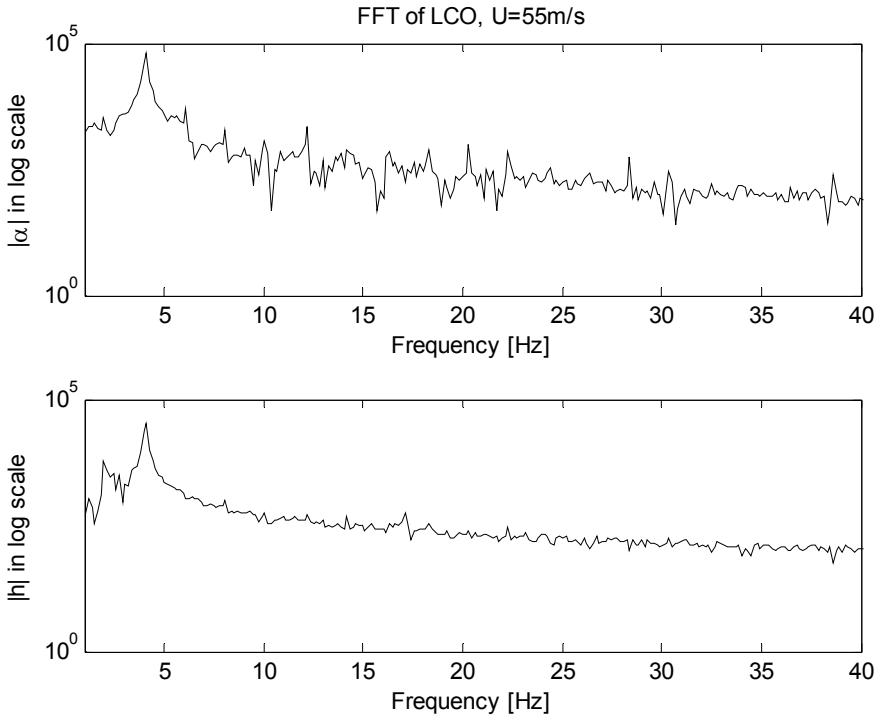

Figure 6. 23: FFT graph of the limit cycle oscillations at U=55 m/s.

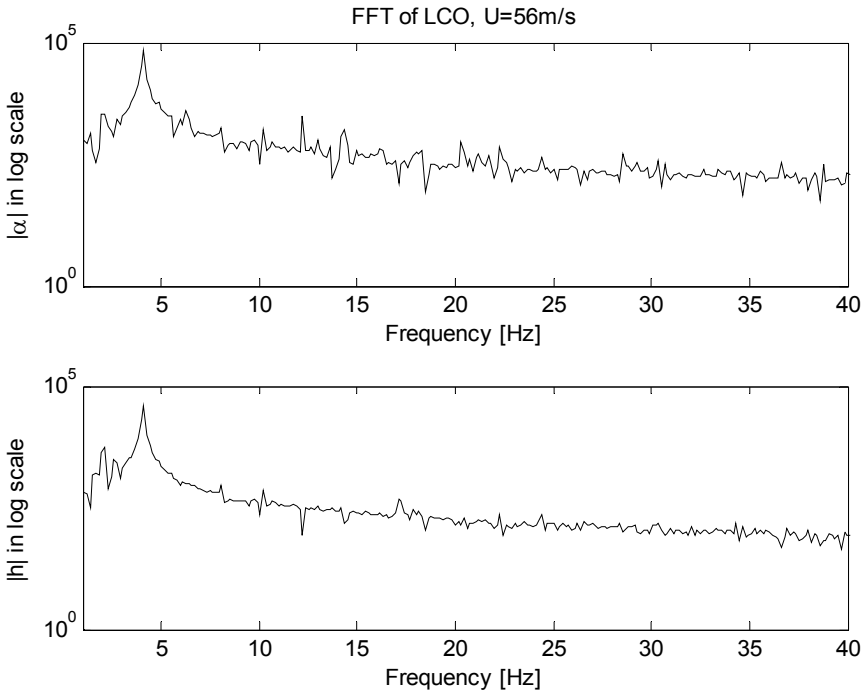

Figure 6. 24: FFT graph of the limit cycle oscillations at U=56 m/s.

Figures 6.18 through 6.24 reveal that the contribution of higher harmonics decrease as the speed increases. Since flutter is a single frequency phenomenon, it is expected to have single frequency limit cycles at speeds close to the flutter speed with increasing amplitudes.

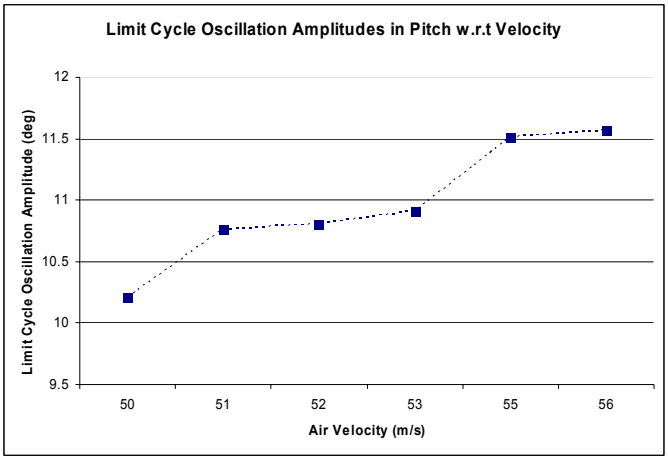

Figure 6. 25: Amplitudes of limit cycle oscillations with respect to air speed.

In Figure 6.27,5, amplitudes of the limit cycle oscillations in pitch degree of freedom are given with respect to speed. The amplitudes of oscillations increase with increasing air speed.

In the sixth experiment, air speed is increased to 60.5 m/s without disturbing the airfoil, and 5 consecutive pulses from 1º to 5º are given to the airfoil at 60.5 m/s. After 5º pulse, sufficient energy is transferred from pitch degree of freedom to plunge degree of freedom to overcome the friction and flutter and was observed. Figure 6.26 shows the data recorded during the flutter phenomenon.

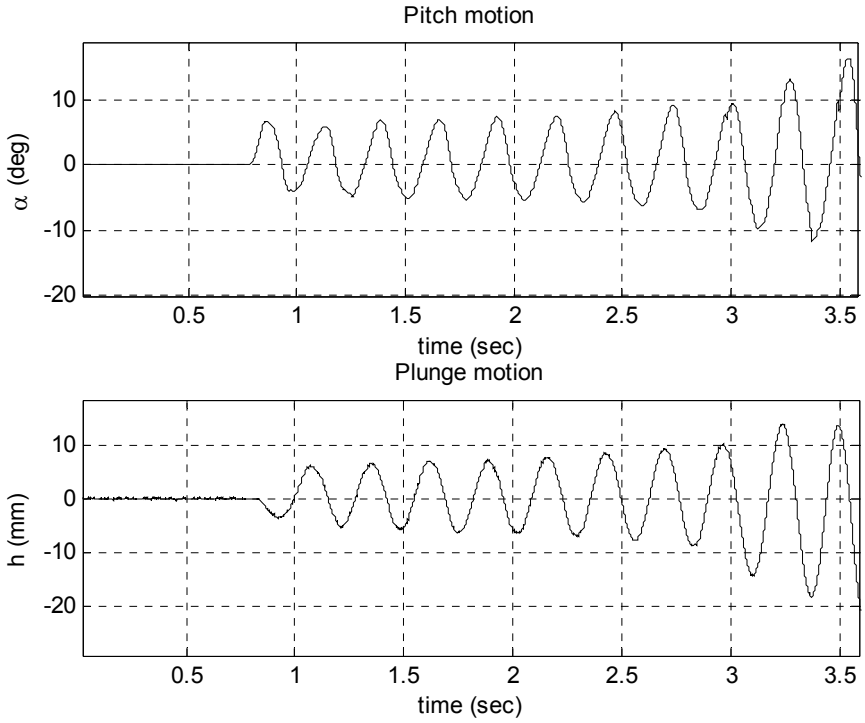

Figure 6. 26: Oscillations during flutter in pitch and plunge at 60.5 m/s.

6.3 Summary of the chapter

In this chapter, design of the wind tunnel experiments and elimination of the some of the stiffness value combinations are discussed. Instrumentation on the ATD is described in detail with some photographs.

Illustrative photographs of the ATD placed in the wind tunnel are also given. In the remaining part of the chapter, results of the conducted experiments are discussed in detail. Problems encountered during the experiments are described and solutions to some of these problems are introduced.

Pulse response of the ATD in pitch and plunge degrees of freedom before and after modifications to the setup are given graphically. Damping characteristics of the test setup are found from the pulse responses in both degrees of freedom by logarithmic decrement method. The effect of modifications is observed by the decrease in the equivalent damping ratio in pitch degree of freedom. The critical flutter speed and frequency of the test setup are calculated including damping. Frequency response characteristics in pitch and plunge are found and given in Figures 6.8 and 6.9.

Flutter is observed during the wind tunnel experiments at 60.5 m/s, and the motion of pitch and plunge during flutter are given in Figures 6.16 and 6.26. Also limit cycle oscillations were observed at various air speeds. Observation of limit cycle oscillations reveals that there are nonlinearities in the test setup. Limit cycle oscillations in pitch are more repeatable than in plunge since the stick-slip friction on the linear guides introduces severe nonlinearity. FFT graphs of limit cycle oscillations at 50 m/s, 51 m/s, 52 m/s, 53 m/s, 55 m/s, and 56 m/s are given. From these graphs, it is concluded that contributions of higher harmonics decrease as the air speed increases since flutter is a single frequency phenomenon, it is expected to have single frequency limit cycles at speeds close to the flutter speed with increasing amplitude. Increase in the limit cycle oscillations amplitude in pitch degree of freedom is also shown.

CHAPTER 7

SUMMARY AND CONCLUSIONS

7.1 Summary

In this study, a two degree of freedom aeroelastic test apparatus (ATD) is designed to observe the flutter phenomenon within the test limits of the Ankara Wind Tunnel. Theoretical flutter calculations based on the typical section and the notation used by Theodorsen are carried out. Simulations to find the critical flutter speed and frequency are performed with various stiffness characteristics combinations in both degrees of freedom. By using the maximum aerodynamic lift force and maximum aerodynamic moment values together with the bandwidth requirement that is set prior to the design stage, the requirements for the servomotor in the pitch axis are obtained. A gearbox with a low backlash and gear ratio of 29 is selected for torque and speed adjustment. The results of the theoretical flutter calculations and simulations serve as a base to determine the stiffness characteristics of the ATD and these values are used to design physically manufacturable torsional and compression springs to be used in pitch and plunge degrees of freedom. The conceptual design of the ATD is completed and detailed design stage started. The mechanical design of the springs is followed by the selection of the resolver and the linear scale, which are used to observe the two states of the dynamical system, namely pitch angle and plunge displacement, respectively. After selecting the sensors, design of the ATD is completed and detailed technical drawings are made for manufacturing the setup components. The most difficult part to manufacture is of course the NACA0012 airfoil profile.

Due to the work load of AWT and long delivery time of the manufactured parts, only one week is reserved for conducting the

experiments in the wind tunnel. Problems encountered during the assembly and pretesting of the test setup further reduce the available test time and experiments can be conducted with only one combination of pitch and plunge stiffness values. However, flutter phenomena is observed in AWT. During experiments, limit cycle oscillations are also observed at different air velocities.

7.2 Conclusions

Designing a structure to observe flutter at low subsonic flow conditions is a much more difficult task than designing a structure not to flutter in this flow condition. ATD is the first test setup to observe flutter in Ankara Wind Tunnel, and probably the first such apparatus built in Turkey. Although the experiments are conducted with only one pitch and plunge stiffness combination, flutter phenomenon as well as limit cycle oscillations are observed in the wind tunnel with the designed setup with a pitch stiffness value of 55.2 N.m/rad and plunge stiffness value of 10,000 N/m.

In designing airborne structures, critical flutter speed and frequency are calculated without including damping in the equations of motion for conservatism. Structural or viscous damping increases the critical flutter speed. But when it comes to designing a system specifically to flutter, especially in a low speed environment, calculations without including damping are not meaningful. So calculating the critical flutter speed and frequency without damping terms is a wrong assumption and a wrong start for the design. A detailed identification of the system should have been carried just after the ATD was assembled in a laboratory environment and damping ratios in both degrees of freedom should have been extracted. Then with these damping ratios, theoretical critical flutter speed and frequency should have been calculated, and the results should have been compared with the experiment results.

The calculated theoretical critical flutter speed including damping do not match the experimental flutter speed. The former is 45.7 m/s while the

latter is 60.5 m/s. This difference between the theoretical and experimental results may arise from the difference between real stiffness values of the compression and torsional springs and theoretical design values. Another source of error is the differences in the damping ratios of pitch and plunge degrees of freedom. The stick-slip friction in plunge motion is a source of severe nonlinearity and it affects the system response. Such severe frictions introduce considerable amount of equivalent damping to the system, which stabilizes the aeroelastic systems. Although some modifications to the setup are made, frequency response of the plunge displacement shows that there is still considerable damping in plunge motion. The effect of this friction can also be seen in pulse responses of plunge degree of freedom. The oscillations in pitch motion last longer than the oscillations in plunge motion and 2º degree pulse response at even high air velocities such as 40 m/s, energy could not be transferred to h. Also manufactured parts may not have the theoretical mass and inertia values, however critical flutter speed and frequency is not affected drastically with such changes. Although the springs in both degrees of freedom are assumed to be linear, spring may not be linear in their operating range.

Although not predicted and studied during thesis, limit cycle oscillations are also observed during experiments. FFT graphs of the limit cycle oscillations reveal that higher harmonics and subharmonics are involved, but the contribution of the higher and subharmonic components decrease as the air speed approaches critical flutter speed, which is 60,5 m/s for the ATD with pitch stiffness value of 55.2 N.m/rad and plunge stiffness value of 10,000 N/m.

Flutter is observed with the test setup at 60.5 m/s. Oscillations during flutter are limited with the mechanical limit in pitch degree of freedom of the ATD, which is ±15º.

Oscillations in flutter are unbounded but the limit cycle oscillations are bounded. Limit cycle oscillations may result from the nonlinearities in

the springs and backlash in the connections of the springs to the airfoil and motor shafts as well as the nonlinear friction force on the linear guides.

7.3 Recommendations for future work

For a complete experimental validation of the theoretical flutter calculations using the ATD, a system identification should be carried out to calculate the damping ratio in each degree of freedom. Using the experimental damping ratios, theoretical flutter calculations should be revised.

Eliminating the friction in the linear guides is another study to be carried out on the ATD. If necessary, some modifications on the mechanical design should be made and other types of guides or other types of rails may be used. Also stiffness characteristics of the springs should be experimentally determined. Characteristics of the compression springs may be determined by using a tensile test machine or by measuring the deflection under certain load. Characteristics of the torsional springs may be determined by applying a certain moment with the help of a moment arm and measuring the deflection angle. Experiments with more combinations of stiffness values in each degree of freedom should be made and the results should be compared with the results of theoretical calculations.

The ATD may be used for further studies on aeroelasticity and aeroservoelasticity as well as nonlinear dynamics and aerodynamics. Since the pitch degree of freedom can be controlled by a servo motor, different flutter suppression controllers may be implemented. Also command tracking controllers may be designed and performances of the controllers may be compared. Different airfoil profiles and different control surfaces may be used with the ATD.

Certain, controllable values of backlash may be given to the system by manufacturing different components and the response of the airfoil may

be observed. Also robustness of controllers to nonlinearities in the system can be studied

Accelerometer data may be used for flutter prediction studies. Since usually accelerometers are used in real flight flutter testing, the ATD is equipped with accelerometers.

Unsteady aerodynamics may be studied with this setup with certain modifications to the airfoil. Pressure transducers may be placed on the surface of the airfoil and the pressure distribution during flutter may be acquired.

REFERENCES

1. Bisplinghoff, Raymond L., Ashley, H., Halfman, Robert L., Aeroelasticity. Addison-Wesley Publications, Massachusetts, 1957.

2. Fung, Y.C., An Introduction to the Theory of Aeroelasticity. Dover Publications, New York, 1993.

3. Marqui C.D., Morgado Jr. E.B., Marques F.D., Wind Tunnel Model and a Controller for Flutter Suppression. 45th AIAA/ASME/ASCE/AHS/ASC Structures, Structural Dynamics, and Materials Conference, AIAA 2004-1854, April 2004.

4. Theodorsen, T., General Theory of Aerodynamic Instability and the Mechanism of Flutter. NACA Technical Report No: 496,1938.

5. Theodorsen, T., Garrick, I.E., Mechanism of Flutter- A Theoretical and Experimental Investigation of the Flutter Problem. NACA Technical Report No: 685, 1938.

6. Wieseman C.D., Edwards J.W., Flutter and Divergence Analysis Using the Generalized Aeroelastic Analysis Method. AIAA 2003 – 1489, April 2003.

7. Borglund D., Kuttenkeuler J., Active Wing Flutter Suppression Using a Trailing Edge Flap. Journal of Fluids and Structures (2002) 16(3) 271-294, August 2001.

8. Lee B.H.K., Gong L., Wong Y.S., Analysis and Computation of Nonlinear Dynamic Response of a Two-Degree-of-Freedom System

and its Application in Aeroelasticity. Journal of Fluids and Structures (1997) 11, 225-246.

9. Goorjian P.M., Guruswamy G.P., Transonic Unsteady Aerodynamic and Aeroelastic Calculations about Airfoils and Wings. Computers and Structures Vol.30, No.4, pp.928-936, 1988.

10. Pidapardi R.M.V., Flutter Analysis of Cantilevered Curved Composite Panels. Composite Structures 25 (1993), 89-93.

11. Adams W.A., Jr., Christhilf D.M., Waszak M.R., Design, Test and Evaluation of Three Active Flutter Suppression Controllers. NASA-TM-4338, October 1992.

12. Riviera J.A., Jr., Dansberry B.E., Bennett R.M., NACA 0012 Benchmark Model Experimental Flutter Results with Unsteady Pressure Distributions. NASA-TM-107581, March 1992.

13. Waszak M.R., Modeling the Benchmark Active Control Technology Wind Tunnel Model for Active Control Design Applications. NASA/TP-1998-206270, June 1998.

14. Riviera J.A., Jr., Dansberry B.E., Bennett R.M., Durham M.H., Turnock D.L., Silva W.A., Physical Properties of the Benchmark Models Program Supercritical Wing. NASA-TM-4457, September 1993.

15. Dowell E., Edwards J., Strganac T.W., Nonlinear Aeroelasticity. 44th AIAA/ASME/ASCE/AHS, Structures, Structural Dynamics, and Materials Conference, April 2003, Virginia.

16. Lind R., Brenner M., Robust Aeroservoelastic Stability Analysis. Springer Publications, 1999.

17. Ricketts, Rodney H., Experimental Aeroelasticity History, Status and Future in Brief. NASA-TM-102651, April 1990.

18. Ogata K., Modern Control Engineering. Prentice-Hall International Editions, 1990.

19. Yıldız, E. N., Aeroelastic Analysis of Nonlinear Control Surfaces, MSc Thesis METU, December 2000.

20. Hooker, R. W., The Aerodynamic Characteristics of Airfoils as Affected by Surface Roughness. NACA-TN-457, April 1933.

21. Shigley J. E., Mischke C. R., Mechanical Engineering Design. Mc Graw Hill International Editions, 1989.

22. Özkaynak A., Özkök B., Katemliadis S., Weltin U., Experimental Setup for the Study of Flutter Control. 9th Mechatronics Forum International Conference, Turkey, August 2004.

23. Akmeşe A., Cömert M. D., Platin B.E., Aeroservoelastic Analysis of Missile Control Surfaces via Robust Control Methods. IFAC 2004.

APPENDIX 1

MATLAB® M - FILES

1.1 M-file for theoretical flutter calculations

```
clear all;
clc;
close all;
% Parameters for the dimensional state space model

% Total Mass (kg)
m=8.93+1.36;              %airfoil plus shaft mass
mmech=m+8.36+9.2;         %total mechanism mass

%Density of air at Ankara level (kg/m^3)
rho=1.115;

%Half chord length (m)
b=0.15;

% span length (m)
l=0.6;

% elastic axis coefficent
a=-0.6;
xalpha=0.5;

% First moment of Inertia (kg-m)
S=m*xalpha*b;

% Second moment of Inertia of the airfoil
Iairfoil=0.048695;        % Load Inertia (kg-m^2)
Ishaft=0.002156;          % Shaft Inertia (kg-m^2)
I=Iairfoil+Ishaft;

% Plunge Stiffness (N/m)
Kh=10000;
wh=sqrt(Kh/m)/2/pi; %(Hz)

% Torsional Stiffness (N-m/rad)
```

```
Kalpha=55.2;
walpha=sqrt(Kalpha/I)/2/pi; %(Hz)


% Coefficients of Theodorsen's Function
c1=0.10805;
c2=0.006825;
c3=0.3455;
c4=0.01365;

flag_flutter=0;

%matrices involved in System Equations
for U=1:100         % (m/s)

   mass=[mmech m*xalpha*b;m*xalpha*b I];
   K1=[Kh 0;0 Kalpha];

   Mnc=[-pi*rho*b^2*l pi*rho*a*b^3*l;pi*rho*a*b^3*l pi*rho*b^4*(1/8+a^2)*l];
   Bnc=[0 -pi*rho*b^2*U*l;0 -pi*rho*b^3*U*(1/2-a)*l];
   R=[-1;b*(a+1/2)];
   S1=[1 b*(1/2-a)];
   S2=[0 1];
   Bc=pi*rho*U*l*b*R*S1;
   Kc=pi*rho*U^2*b*l*R*S2;
   D0=2*pi*rho*l*U^2*R*[U*c2/b c1];

   M=mass-Mnc;
   B=-Bnc-Bc;
   K=K1-Kc;

   E1=[0 0;1 b*(1/2-a)];
   E2=[0 0;0 U];
   F=[0 1;-U^2*c4/b^2 -U*c3/b];

   % system matrix
   A=[zeros(2,2) eye(2) zeros(2,2); -inv(M)*K -inv(M)*B inv(M)*D0;E2 E1 F];
   B=[0;0;inv(M)*[0;Kalpha];0;0];
   C=[1 0 0 0 0 0;0 1 0 0 0 0];
   D=[0;0];
   sys=pck(A,B,C,D);
   sys2=ss(A,B,C,D);

   % for loop with U=1:70

   poles(U,:)=spoles(sys);
   all_poles(U,:)=sort(poles(U,:));
   realparts_of_poles(U,:)=(real(all_poles(U,:)));
   imagparts_of_poles(U,:)=(imag(all_poles(U,:)));


   % For loop to find the flutter speed
```

```
   if flag_flutter==0
      if U>1
         for (i=1:6)
            if (realparts_of_poles(U,i)*(realparts_of_poles(U-1,i)) < 0)
               % Linear Lagrange Interpolation Algorithm
               f0=realparts_of_poles(U-1,i);
               f1=realparts_of_poles(U,i);
               x0=U-1;
               x1=U;
               Flutter_Speed=-((f1*x0-f0*x1)/(x0-x1))/((f0-f1)/(x0-x1));
               flag_flutter=1;
               Flutter_Frequency=(abs(all_poles(U-1,i))+abs(all_poles(U,i)))/2;
            end
         end
      end
   end
end

plot(realparts_of_poles);
title('Real Parts of Open Loop Poles vs. Air Speed');
xlabel('Air Speed, m/s');
ylabel('Real Parts of Open Loop Poles');
grid;
figure;
plot(imagparts_of_poles)/2/pi;
grid;
figure;
plot(all_poles,'x');
title('Loci of Open Loop Poles w.r.t Air Speed');
xlabel('Re');
ylabel('Im');
grid;
sqrt(eig(inv(M)*K1))/2/pi   % uncoupled natural frequencies
['wh=',num2str(wh),', Hz    w_alpha=',num2str(walpha),' Hz,    Flutter
Speed=',num2str(Flutter_Speed),' m/s,  Flutter Frequency=',num2str(Flutter_Frequency/2/pi),' Hz']
```

1.2 M-file for determining the aeroelastic system matrix at certain air speed

```
%System matrices for certain air speed and stiffness values
clear all;
clc;
close all;
% Parameters for the dimensional state space model

% Air speed
U=60;

% Total Mass (kg)
m=8.93+1.36;              %airfoil plus shaft mass
mmech=m+7+8.36+9.2;    %total mechanism mass
```

```
%Density of air at Ankara level (kg/m^3)
rho=1.115;

%Half chord length (m)
b=0.15;

% span length (m)
l=0.6;

% elastic axis coefficent
a=-0.6;
xalpha=0.5;

% First moment of Inertia (kg-m)
S=m*xalpha*b;

% Second moment of Inertia of the airfoil
Iairfoil=0.048695;          % Load Inertia (kg-m^2)
Ishaft=0.002156;            % Shaft Inertia (kg-m^2)
I=Iairfoil+Ishaft;

% Plunge Stiffness (N/m)
Kh=30000;
wh=sqrt(Kh/m)/2/pi; %(Hz)

% Torsional Stiffness (N-m/rad)
Kalpha=165.6;
walpha=sqrt(Kalpha/I)/2/pi; %(Hz)


% Coefficients of Theodorsen's Function
c1=0.10805;
c2=0.006825;
c3=0.3455;
c4=0.01365;

%matrices involved in System Equations
mass=[mmech m*xalpha*b;m*xalpha*b I];
K1=[Kh 0;0 Kalpha];

Mnc=[-pi*rho*b^2*l pi*rho*a*b^3*l;pi*rho*a*b^3*l pi*rho*b^4*(1/8+a^2)*l];
Bnc=[0 -pi*rho*b^2*U*l;0 -pi*rho*b^3*U*(1/2-a)*l];
R=[-1;b*(a+1/2)];
S1=[1 b*(1/2-a)];
S2=[0 1];
Bc=pi*rho*U*l*b*R*S1;
Kc=pi*rho*U^2*b*l*R*S2;
D0=2*pi*rho*l*U^2*R*[U*c2/b c1];

M=mass-Mnc;
B=-Bnc-Bc;
K=K1-Kc;
```

```
E1=[0 0;1 b*(1/2-a)];
E2=[0 0;0 U];
F=[0 1;-U^2*c4/b^2 -U*c3/b];

% system matrices
A=[zeros(2,2) eye(2) zeros(2,2); -inv(M)*K -inv(M)*B inv(M)*D0;E2 E1 F];
B=[0;1;0;0;0;0];
C=[1 0 0 0 0 0;0 1 0 0 0 0];
D=[0;0];
[b,a]=ss2tf(A,B,C,D);
```

1.3 M-file for motor selection calculation

```
clear all;
clc;
close all;
% Determining the Limit Loads
% Motor Stall Torque is calculated assuming
% Steady aerodynamic moment and Lift acting on the airfoil.
% Chord length of the airfoil
c=0.3;                  % (m)
% Span Length of the airfoil
s=0.6;                  % (m)
% Density of air at Ankara level
rho=1.1341;             % kg/m^3
% Maximum operating speed at flutter conditions at the AWT;
U=70;                   % (m/s)
S=c*s;                  %Surface area of the airfoil
% Factor of Safety
n=1.2;
% Elastic axis coefficient worst case
a=-0.6;

% Cl is taken from NACA Technical Report no.457
% 'The Aerodynamic characteristics of airfoils as affected by surface
% roughness' Ray W. Hooker, LANGLEY;
% assuming the airfoil is metal(Al), machined and the surface roughness
% is as machine-cut and the airfoil is operating at -/+15 deg (linear region).

Cl=1.42;

% Steady Lift
L=-0.5*Cl*rho*U^2*S*n;

% Steady Moment
M=L*(c*a+0.5*c)*s;

%Bandwidth Requirement of the system is 50 Hz @ 1 deg
F=50;
t=0:0.00001:.2;
% Torque Equation (in phase with the angle)
T=M*sin(2*pi*F*t);
% Angle, Speed and acc. Equation
```

```
theta=pi/180*sin(2*pi*F*t);
theta_d=2*F*pi^2/180*cos(2*pi*F*t);
theta_dd=-2^2*F^2*pi^3/180*sin(2*pi*F*t);

% Inertial Properties of the components
Imotor=1.5e-4+0.068e-4;        % Motor Inertia (kg-m^2)
Igearbox=1.34e-4;              % Gearbox Inertia (kg-m^2)
Ishaft=0.002156;               % Shaft Inertia (kg-m^2)
Iairfoil=0.048695;               % Load Inertia (kg-m^2)


Pmax=(-T+(Igearbox+Ishaft+Iairfoil)*theta_dd).*(theta_d);
Pmin=(T+(Igearbox+Ishaft+Iairfoil)*theta_dd).*(theta_d);
figure(1);
plot(t,Pmin,'b');
hold on
plot(t,Pmax,'m');
grid

% Motor Selected with Power Rating 1107 W and
% with Back EMF constant of 160 V/KRPM
% and Torque Constant of 1.53 N-m/amp

Kt=0.74;
Kb=47.5;

% The servo driver circuit used can give 320 VDC output voltage to the motor

max_speed=320/Kb*1000;       % max speed achieved by the motor @320VDC
wreq=60;                     % Required Speed (rpm)

% Maximum Rated Power of the selected motor
P_max_rated=1.48e3             %(kW)

% Maximum Mechanical Speed of the selected motor
max_mech_speed=6000            % (rpm)

% Selected gear Ratio is 29:1
N=29;

% Required motor shaft speed;
W=wreq*N;

if max_speed < max_mech_speed
   if W < max_speed
      'Speed OK'
   end
else
   if W < max_mech_speed
      'Speed OK'
   end
end
```

```
% Add motor inertia at the load to check the power
Pmax_2=(-T+(Igearbox+Ishaft+Iairfoil+Imotor*N^2)*theta_dd).*(theta_d);
Pmin_2=(T+(Igearbox+Ishaft+Iairfoil+Imotor*N^2)*theta_dd).*(theta_d);
figure(2);
plot(t,Pmin_2,'b');
hold on
plot(t,Pmax_2,'m');
max(Pmax_2);
min(Pmin_2);
grid

if max(Pmax_2)< P_max_rated
   'Power OK'
end

['Pmax = ',num2str(max(Pmax)),'W',',  Pmin = ',num2str(max(Pmin)),'W',',  Pmax_2=
',num2str(max(Pmax_2)),'W']
['Pmin_2= ',num2str(max(Pmin_2)),'W',',    W=',num2str(W),'rpm',',
max_speed=',num2str(max_speed),'rpm']
['Max Lift=',num2str(L),'N',',  Max Moment=',num2str(M),'N_m']
```

1.4 M-file for spring design calculations

```
% LINEAR COMPRESSION and TORSIONAL SPRING DESIGN CALCULATIONS

% LINEAR COMPRESSION SPRING
d=6;        %(mm) wire diameter
D=60;       %(mm) mean spring diameter
G=80e3;     %(Mpa)Shear Modulus of Elasticity
Nmax=7;     % maximum number of active coils
for i=1:5;
   K=(d^4*G)/(8*D^3*(Nmax-i)); % (N/mm)spring equation
   K*1000                  % (N/m) stiffness values
end

% Strength Calculations
Fmax=855;   %maximum lift force
C=D/d;      %spring index
Ks=1+0.5/C; %shear-stress multiplication factor
tau=Ks*(8*Fmax*D)/(pi*d^3);
tau

% TORSIONAL SPRING
d=8;        %(mm) wire diameter
D=40;       %(mm) mean spring diameter
E=207e3;    %(MPa)Modulus of Elasticity
Nmax=8;     %maximum number of active coils
for j=1:6;
   K_tor=(d^4*E)/(64*D*(Nmax-j));  %(Nmm/rad)  spring equation
   K_tor/1000                  %(Nm/rad)   stiffness values
end
```

```
% Strength Calculations
Mmax=15.5;    %(Nm) maximum aerodynamic moment
C=D/d;      % spring index
Ki=(4*C^2-C-1)/(4*C*(C-1));
Ko=(4*C^2+C-1)/(4*C*(C+1));
if Ki > Ko;
   sigma=Ki*(32*Mmax*1000)/(pi*d^3);
else
   sigma=Ko*(32*Mmax*1000)/(pi*d^3);end sigma
```

1.5 Modified m-file for calculating the critical flutter speed and frequency with damping

```
clear all;
clc;
close all;
% Parameters for the dimensional state space model

% Total Mass (kg)
m=8.93+1.36;              %airfoil plus shaft mass
mmech=m+8.36+9.2;         %total mechanism mass

%Density of air at Ankara level (kg/m^3)
rho=1.115;

%Half chord length (m)
b=0.15;

% span length (m)
l=0.6;

% elastic axis coefficent
a=-0.6;
xalpha=0.5;

% First moment of Inertia (kg-m)
S=m*xalpha*b;

% Second moment of Inertia of the airfoil
Iairfoil=0.048695;          % Load Inertia (kg-m^2)
Ishaft=0.002156;            % Shaft Inertia (kg-m^2)
I=Iairfoil+Ishaft;

% Plunge Stiffness (N/m)
Kh=10000;
wh=sqrt(Kh/m)/2/pi; %(Hz)

% Torsional Stiffness (N-m/rad)
Kalpha=55.2;
walpha=sqrt(Kalpha/I)/2/pi; %(Hz)
```

```
% Coefficients of Theodorsen's Function
c1=0.10805;
c2=0.006825;
c3=0.3455;
c4=0.01365;

% Damping terms
zetah=0.14;
ch=zetah*2*sqrt(Kh*m);              % plunge damping
zetaa=0.08;
calpha=zetaa*2*sqrt(Kalpha*I);   % pitch damping
C_damp=[ch 0;0 calpha];

flag_flutter=0;

%matrices involved in System Equations
for U=1:100          % (m/s)

   mass=[mmech m*xalpha*b;m*xalpha*b I];
   K1=[Kh 0;0 Kalpha];

   Mnc=[-pi*rho*b^2*l pi*rho*a*b^3*l;pi*rho*a*b^3*l pi*rho*b^4*(1/8+a^2)*l];
   Bnc=[0 -pi*rho*b^2*U*l;0 -pi*rho*b^3*U*(1/2-a)*l];
   R=[-1;b*(a+1/2)];
   S1=[1 b*(1/2-a)];
   S2=[0 1];
   Bc=pi*rho*U*l*b*R*S1;
   Kc=pi*rho*U^2*b*l*R*S2;
   D0=2*pi*rho*l*U^2*R*[U*c2/b c1];

   M=mass-Mnc;
   B=-Bnc-Bc;
   K=K1-Kc;

   E1=[0 0;1 b*(1/2-a)];
   E2=[0 0;0 U];
   F=[0 1;-U^2*c4/b^2 -U*c3/b];

   % system matrix
   A=[zeros(2,2) eye(2) zeros(2,2); -inv(M)*K -inv(M)*(B+C_damp) inv(M)*D0;E2 E1 F];
   B=[0;0;inv(M)*[0;Kalpha];0;0];
   C=[1 0 0 0 0 0;0 1 0 0 0 0];
   D=[0;0];
   sys=pck(A,B,C,D);
   sys2=ss(A,B,C,D);

   % for loop with U=1:70

   poles(U,:)=spoles(sys);
   all_poles(U,:)=sort(poles(U,:));
   realparts_of_poles(U,:)=(real(all_poles(U,:)));
   imagparts_of_poles(U,:)=(imag(all_poles(U,:)));
```

```
   % For loop to find the flutter speed

   if flag_flutter==0
      if U>1
         for (i=1:6)
            if (realparts_of_poles(U,i)*(realparts_of_poles(U-1,i)) < 0)
               % Linear Lagrange Interpolation Algorithm
               f0=realparts_of_poles(U-1,i);
               f1=realparts_of_poles(U,i);
               x0=U-1;
               x1=U;
               Flutter_Speed=-((f1*x0-f0*x1)/(x0-x1))/((f0-f1)/(x0-x1));
               flag_flutter=1;
               Flutter_Frequency=(abs(all_poles(U-1,i))+abs(all_poles(U,i)))/2;
            end
         end
      end
   end
end

plot(realparts_of_poles);
title('Real Parts of Open Loop Poles vs. Air Speed');
xlabel('Air Speed, m/s');
ylabel('Real Parts of Open Loop Poles');
grid;
figure;
plot(imagparts_of_poles)/2/pi;
grid;
figure;
plot(all_poles,'x');
title('Loci of Open Loop Poles w.r.t Air Speed');
xlabel('Re');
ylabel('Im');
grid;
sqrt(eig(inv(M)*K1))/2/pi   % uncoupled natural frequencies
['wh=',num2str(wh),', Hz    w_alpha=',num2str(walpha),' Hz,    Flutter
Speed=',num2str(Flutter_Speed),' m/s,  Flutter Frequency=',num2str(Flutter_Frequency/2/pi),' Hz']
```

APPENDIX 2

TECHNICAL DRAWINGS AND DATA SHEETS

2.1 Technical Drawings of the components

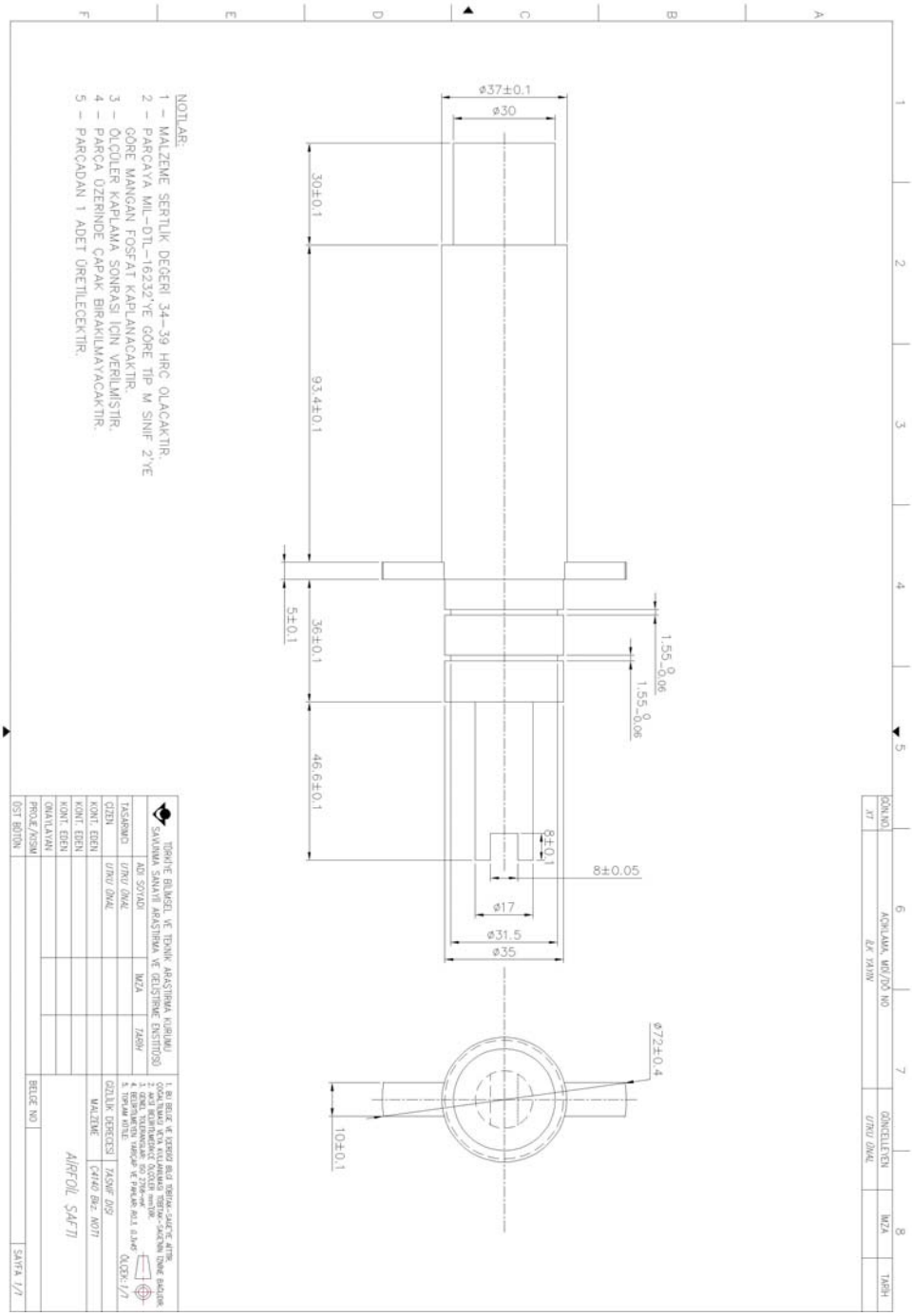

Figure A.2. 1: Technical drawing of the airfoil shaft.

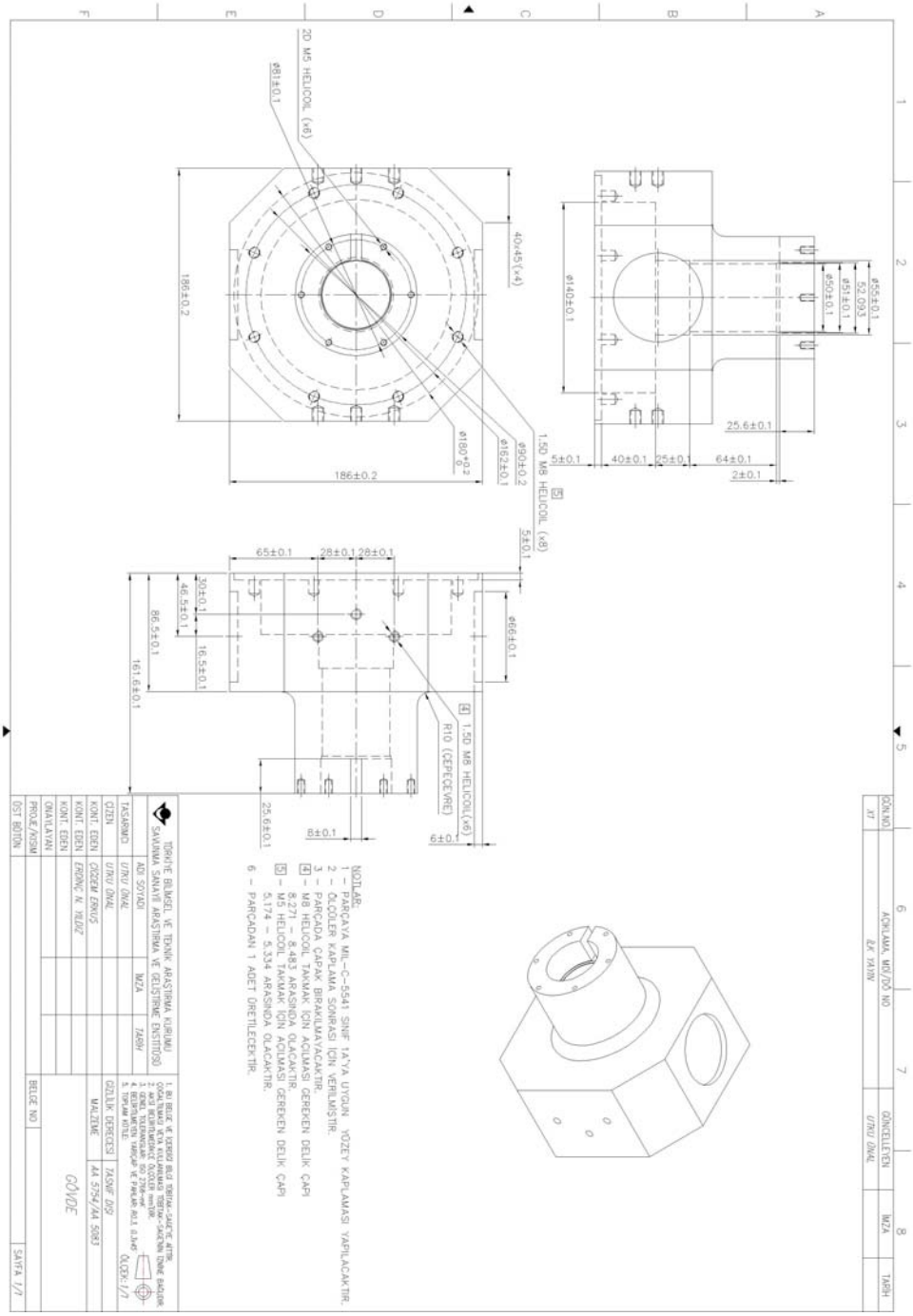

Figure A.2. 2: Technical drawing of the casing.

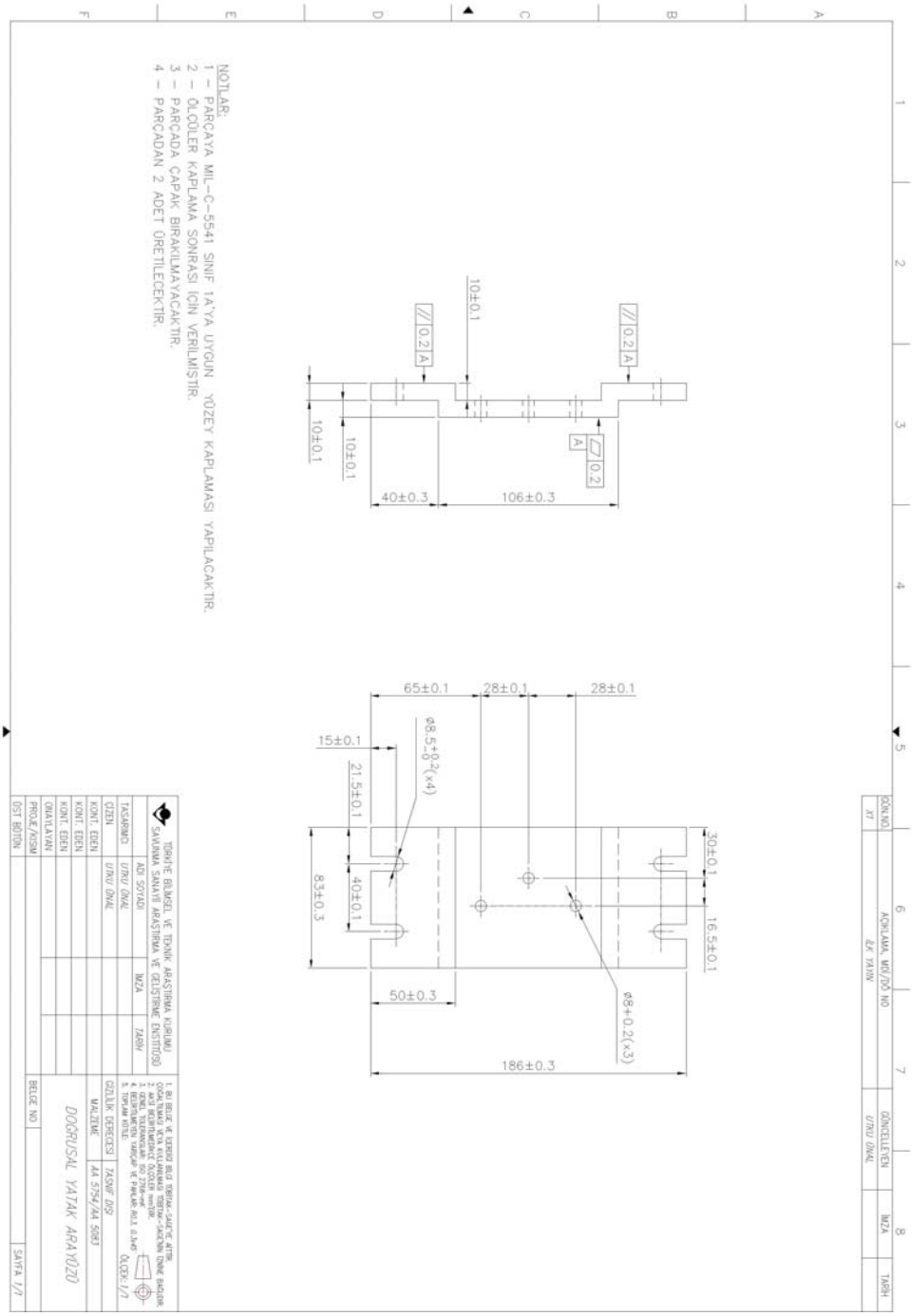

Figure A.2. 3: Technical drawing of the linear guide interfaces.

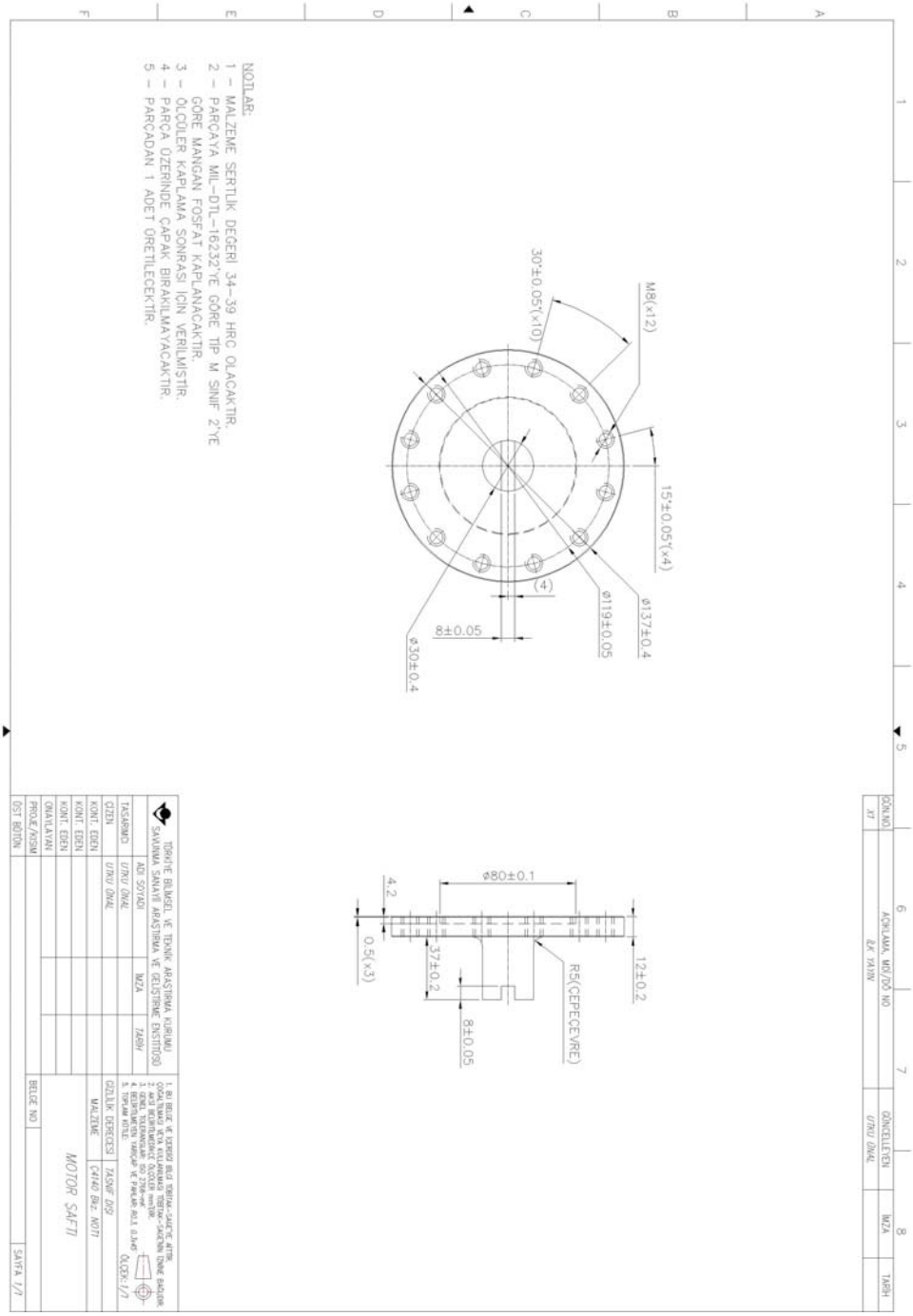

Figure A.2. 4: Technical drawing of the motor shaft.

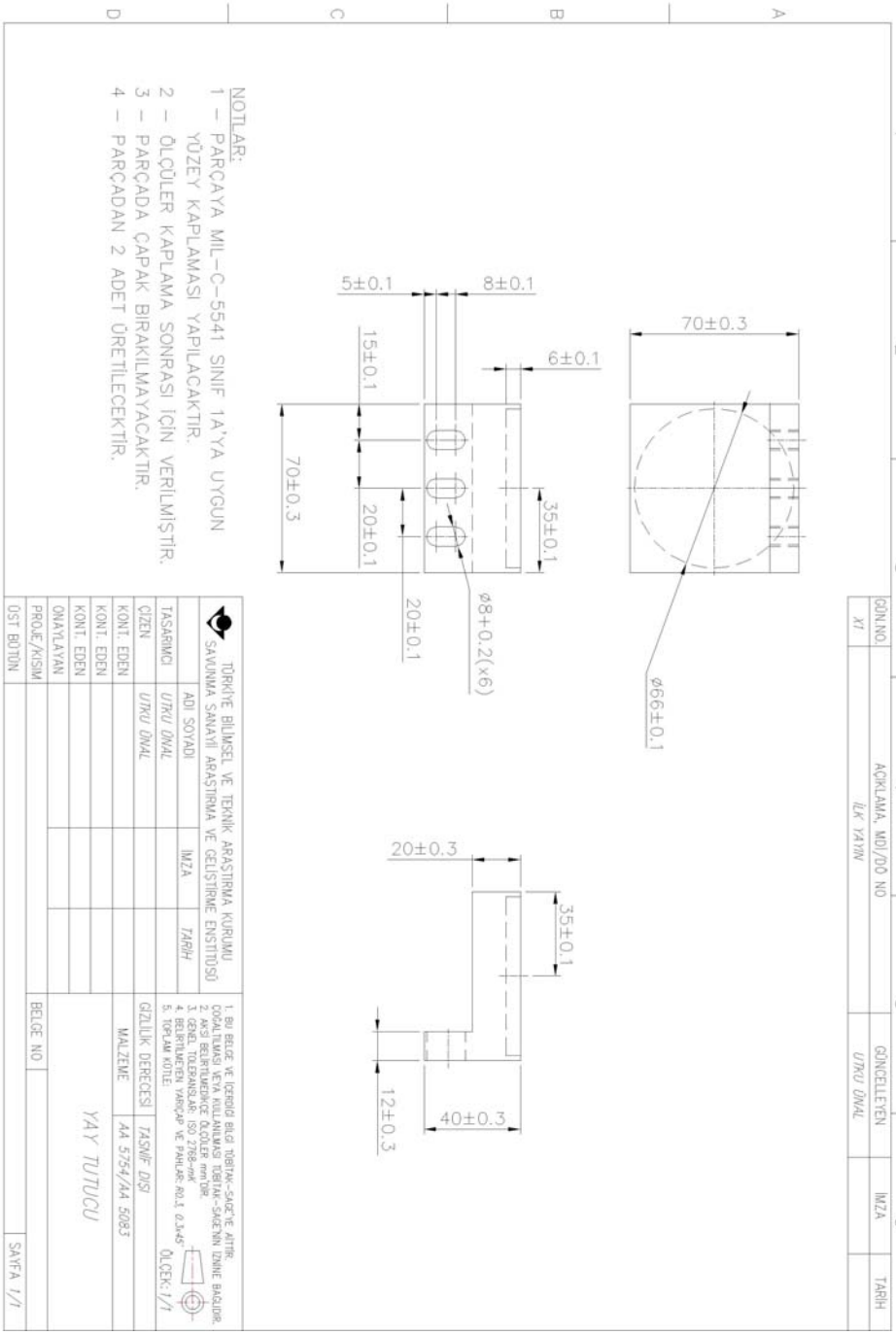

Figure A.2. 5: Technical drawing of the spring holder.

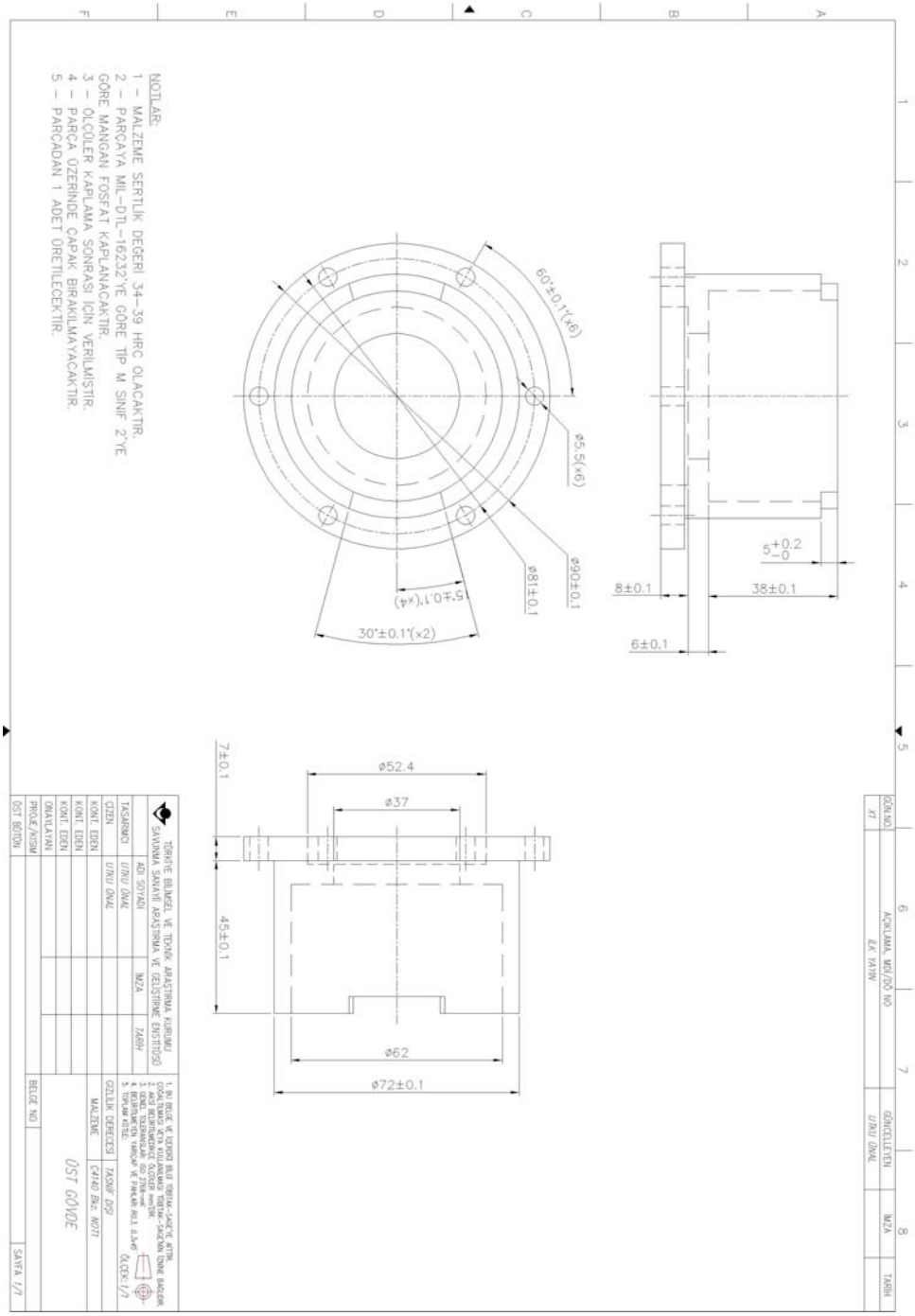

Figure A.2. 6: Technical drawing of the upper casing.

2.2 Data sheets

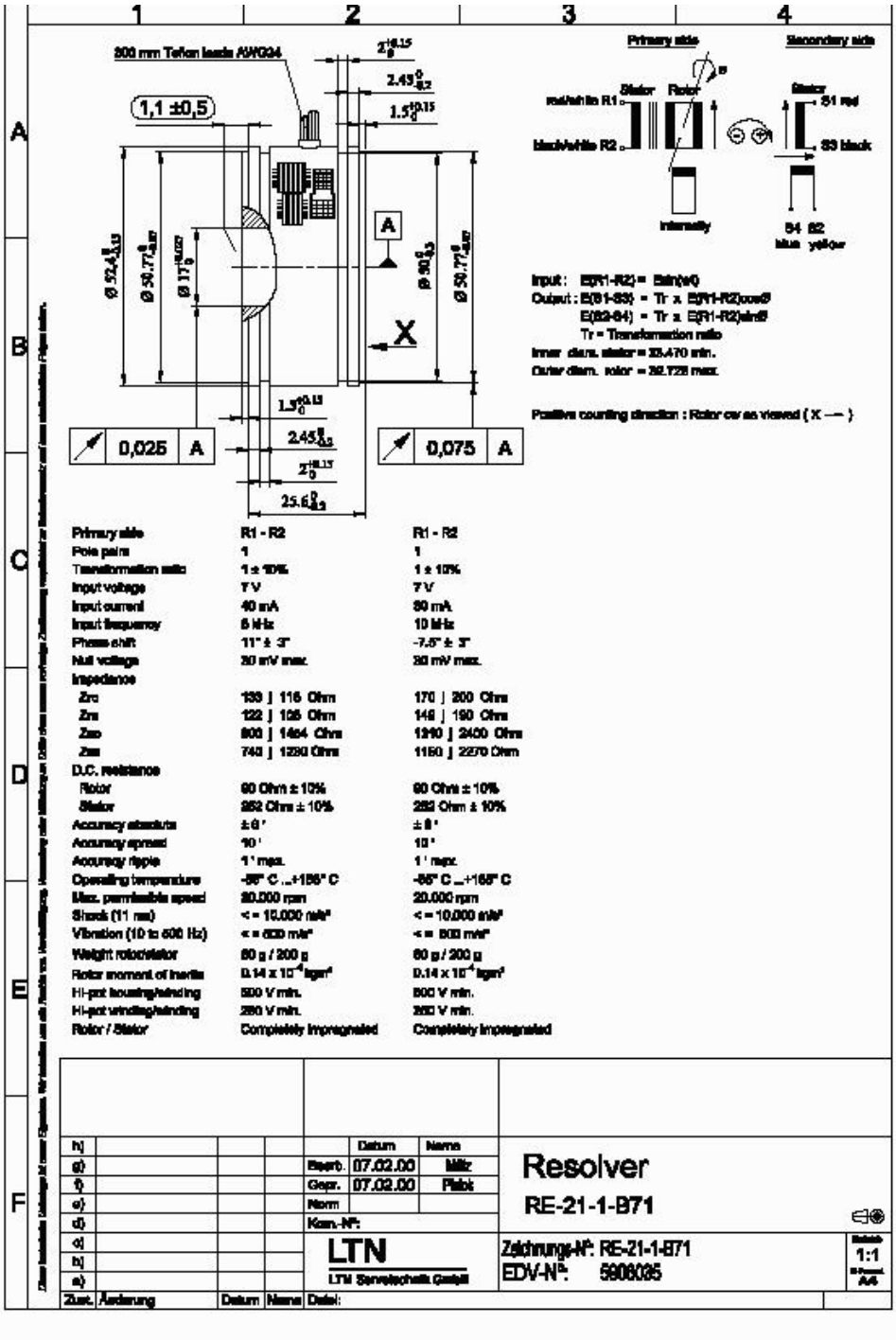

Figure A.2. 7: The data sheet of RE-21-1-B71 Resolver.

Linear scale
GEL 176

SENSORLINE
LENORD+BAUER

Technical information ***Version 11.02***

The pressure-proof linear scale GEL 176 - made of stainless steel - was conceived for the direct use in a hydraulic cylinder. It is furthermore suited for the external installation into industrial automation lines. This linear scale offers the user the following important advantages:

- a long service life due to the contactless and wearless measuring of position magnets
- direct, digital synchronous serial output (SSI) or direct analogue current or voltage output
- there is a homogeneous supply voltage of 24 V
- for lengths up to 7,600 mm
- resolution up to 5 µm (SSI) and 16 bits (analogue)

Output signals

The absolute information on the travelled path is supplied either digitally or analogue. The digital transmission is performed in Gray-Code, so that a simple cabling is ensured and the transmission security rises. Various current/voltage outputs are available as analogue output signals.

Measuring principles

The tried and tested measuring principle was further improved. It is the running time of the torsion pulse that is measured and which is proportional to the distance between an internal start signal and a stop signal. The torsion emerges from the interaction of two magnetic fields under the position magnet. The running time is the absolute measure up to the position of the magnet and is transformed into a digital or analogue output signal.

Internet: http://www.lenord.de
E-Mail: info@lenord.de
Tel.: +49 (0)208 9963-0
Fax: +49 (0)208 676292
Lenord, Bauer & Co. GmbH
Dohlenstrasse 32
46145 Oberhausen, Germany

Figure A.2. 8: The data sheet of Lenord Bauer's GEL176 A0100 A Linear Scale.

Technical Data

sensor	analogue	SSI
sensor head	aluminium die casting	
protection class	IP 65	
sensor tube with flange	stainless steel	
pressure resistance	350 bar	
protection class	IP 67	
installation thread	M18 x 1,5	
assemby fitting position	any	
connection type	plug or cable connection	
measuring length	50 ... 7600 mm in 50 mm steps	
resolution	25 µm or 16 Bit	5 µm
linear tolerance (non-corrected)	< ± 0,02 %*, min. ± 50 µm (independent of influences of temperature from outside)	< ± 0,01 %*, min. ± 40 µm (independent of influences of temperature from outside)
repeatability	< ± 0,001 %*, min. ± 2,5 µm	
hysteresis	< 4 µm	
voltage supply	24 V DC (+20 % /-15%)	
power consumption	100 mA typ.	70 mA typ.
temperature coefficient	< 40 ppm/°C	< 15 ppm/°C
voltage sustaining capability	500 V	
operating temperature	-40 °C ... +75 °C	
EMC (if the assembly instructions are observed)		
electromagnetic emissions	EN 50081-1	
electromagnetic immunity	EN 50082-2	
The linear scale GEL 176 is in strict conformity with Directive EMC 89/336/EEC of the European Union which is certified by the CE mark.		
shock protection	100 g (single shock) as per IEC 68-2-27	
vibration protection	5 g /10 ... 150 Hz as per IEC 68-2-6	
SSI		
data format	-	Gray
data length	-	25 bits
output signal		
voltage	0 ... + 10 V or + 10 ... 0 V, $R_L \geq 5$ kΩ	-
current	0 ... +20 mA or +20 ... 0 mA 4 ... +20 mA or +20 ... 4 mA burden 0 ... 500 Ω	-

* referring to the measuring length

Figure A.2.8 (Continued): The data sheet of Lenord Bauer's GEL176 A0100 A Linear Scale.

Synchronous serial interface, Pin layouts

Synchronous serial interface

Principles of serial data transmission
Gray code (25 bits)

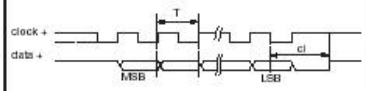

f ≥ 100 kHz
cl = clock pulse space min. 16 µs
T = cycle duration of the clock signal

Number of distance measurements per second

measuring length	150	300	500	750	1000	2000
measure-ments	10000	6600	4500	3300	2500	1400

Baud rate
The transmission rate depends on the line length and reaches a maximum of 1.5 MBaud. Use screened cables with paired wires.

cable length	<50	<100	<200	<400
clock frequency [kHz]	<400	<300	<200	<100

Pin layout (analogue)
6-pole plug or cable outlet

soldered side

pin	cable	0 ... 20 mA	20 ... 0 mA	4 ... 20 mA	20 ... 4 mA	0 ... 10 V	10 ... 0 V
1	grey	0 ... 20 mA	20 ... 0 mA	4 ... 20 mA	20 ... 0 mA	0 ... 10 V	10 ... 0 V
2	pink	DC GND					
3	yellow	nc	nc	nc	nc	nc	nc
4	green	nc					
5	brown	+ 24 V DC (+ 20 % / -15 %)					
6	white	DC GND					

Pin layout (SSI)
7-pole plug or cable outlet

soldered side

pin	cable	signal
1	grey	data (-)
2	pink	data (+)
3	yellow	clock (+)
4	green	clock (-)
5	brown	+24 V DC
6	white	0 V
7	-	nc

Figure A.2.8 (Continued): Third page of the data sheet of Lenord Bauer's GEL176 A0100 A Linear Scale.

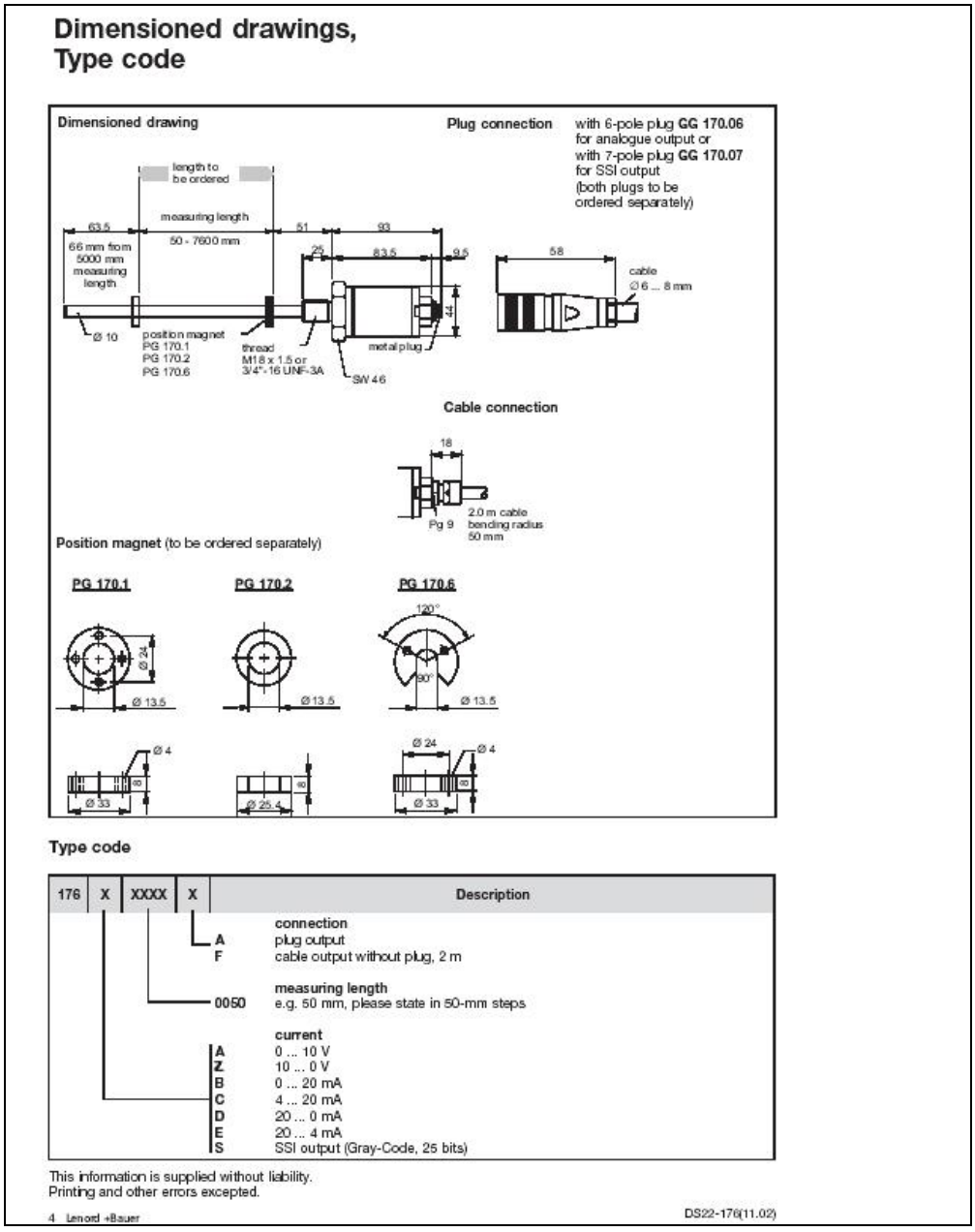

Figure A.2.8 (Continued): Fourth page of the data sheet of Lenord Bauer's GEL176 A0100 A Linear Scale.

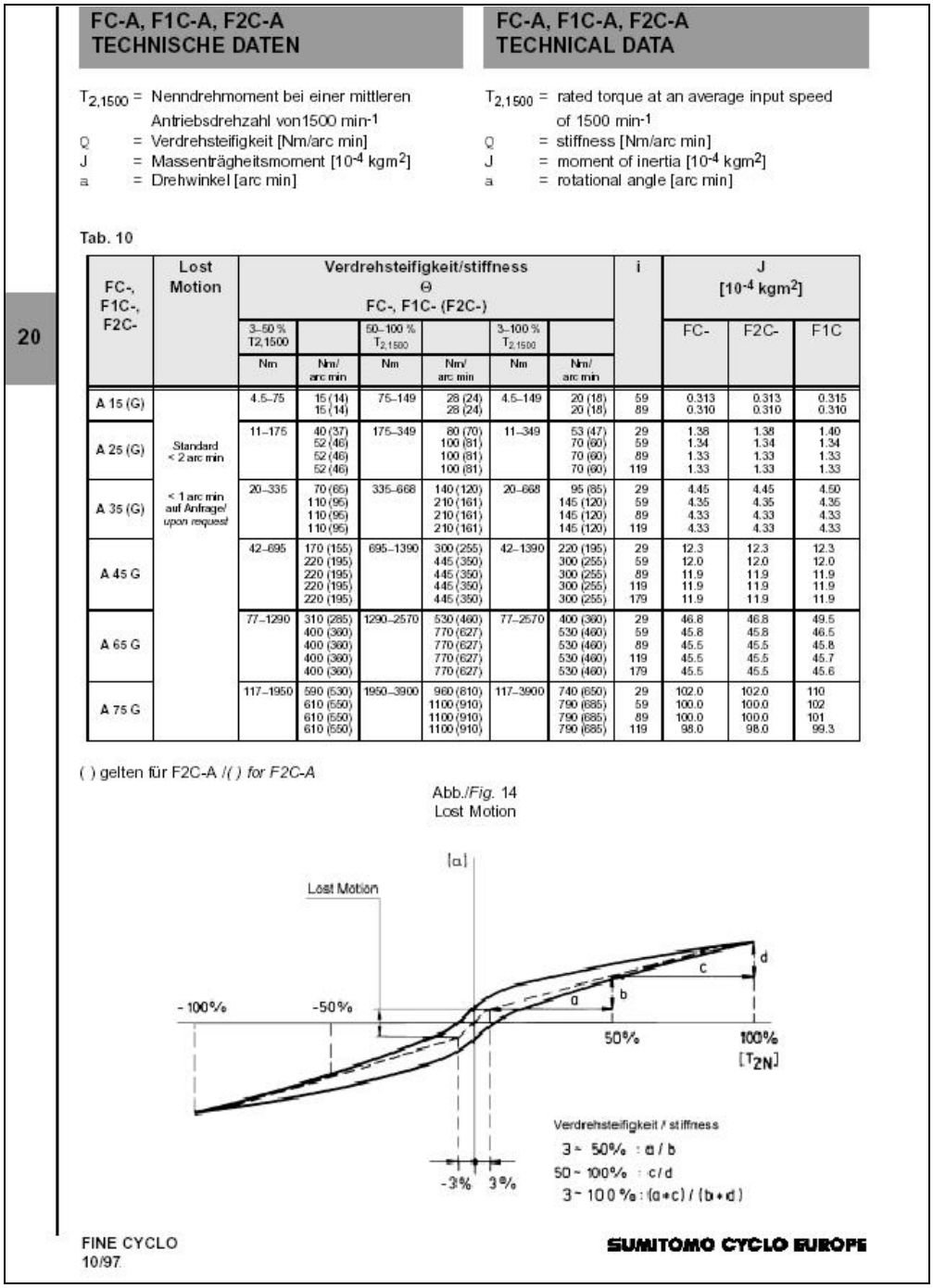

FC-A, F1C-A, F2C-A
TECHNISCHE DATEN

$T_{2,1500}$ = Nenndrehmoment bei einer mittleren Antriebsdrehzahl von1500 min^{-1}
Q = Verdrehsteifigkeit [Nm/arc min]
J = Massenträgheitsmoment [10^{-4} kgm^2]
a = Drehwinkel [arc min]

FC-A, F1C-A, F2C-A
TECHNICAL DATA

$T_{2,1500}$ = rated torque at an average input speed of 1500 min^{-1}
Q = stiffness [Nm/arc min]
J = moment of inertia [10^{-4} kgm^2]
a = rotational angle [arc min]

Tab. 10

20

FC-, F1C-, F2C-	Lost Motion	Verdrehsteifigkeit/stiffness Θ FC-, F1C- (F2C-)						i	J [10^{-4} kgm^2]		
		3–50 % $T_{2,1500}$		50–100 % $T_{2,1500}$		3–100 % $T_{2,1500}$			FC-	F2C-	F1C
		Nm	Nm/ arc min	Nm	Nm/ arc min	Nm	Nm/ arc min				
A 15 (G)	Standard < 2 arc min < 1 arc min auf Anfrage/ *upon request*	4.5–75	15 (14) 15 (14)	75–149	28 (24) 28 (24)	4.5–149	20 (18) 20 (18)	59 89	0.313 0.310	0.313 0.310	0.315 0.310
A 25 (G)		11–175	40 (37) 52 (46) 52 (46) 52 (46)	175–349	80 (70) 100 (81) 100 (81) 100 (81)	11–349	53 (47) 70 (60) 70 (60) 70 (60)	29 59 89 119	1.38 1.34 1.33 1.33	1.38 1.34 1.33 1.33	1.40 1.34 1.33 1.33
A 35 (G)		20–335	70 (65) 110 (95) 110 (95) 110 (95)	335–668	140 (120) 210 (161) 210 (161) 210 (161)	20–668	95 (85) 145 (120) 145 (120) 145 (120)	29 59 89 119	4.45 4.35 4.33 4.33	4.45 4.35 4.33 4.33	4.50 4.35 4.33 4.33
A 45 G		42–695	170 (155) 220 (195) 220 (195) 220 (195) 220 (195)	695–1390	300 (255) 445 (350) 445 (350) 445 (350) 445 (350)	42–1390	220 (195) 300 (255) 300 (255) 300 (255) 300 (255)	29 59 89 119 179	12.3 12.0 11.9 11.9 11.9	12.3 12.0 11.9 11.9 11.9	12.3 12.0 11.9 11.9 11.9
A 65 G		77–1290	310 (285) 400 (360) 400 (360) 400 (360) 400 (360)	1290–2570	530 (460) 770 (627) 770 (627) 770 (627) 770 (627)	77–2570	400 (360) 530 (460) 530 (460) 530 (460) 530 (460)	29 59 89 119 179	46.8 45.8 45.5 45.5 45.5	46.8 45.8 45.5 45.5 45.5	49.5 46.5 45.8 45.7 45.6
A 75 G		117–1950	590 (530) 610 (550) 610 (550) 610 (550)	1950–3900	960 (810) 1100 (910) 1100 (910) 1100 (910)	117–3900	740 (650) 790 (685) 790 (685) 790 (685)	29 59 89 119	102.0 100.0 100.0 98.0	102.0 100.0 100.0 98.0	110 102 101 99.3

( ) gelten für F2C-A / *( ) for F2C-A*

Abb./*Fig.* 14
Lost Motion

FINE CYCLO
10/97

SUMITOMO CYCLO EUROPE

Figure A.2. 9: A sample page of the Sumitomo's FC-A35-29 gearbox data sheet showing the inertia and stiffness properties of the gearbox.

APPENDIX 3

TABLES RELATED TO EXPERIMENTS

3.1 Critical Flutter velocities and frequencies for different pitch and plunge stiffness values

Table A3.1 1: Critical flutter speed and flutter frequency for plunge stiffness of 30,000 N/m.

Plunge Stiffness (N/m)	Pitch Stiffness (Nm/rad)	Cr. Flutter Speed (m/s)	Cr. Flutter Frequency (Hz)
30,000	47.3	40.4	5.3
30,000	55.2	40.9	5.3
30,000	66.3	41.9	5.3
30,000	82.8	43.6	5.4
30,000	110.4	47.3	5.5
30,000	165.6	56.2	5.7

Table A3.1 2: Critical flutter speed and flutter frequency for plunge stiffness of 20,000 N/m.

Plunge Stiffness (N/m)	Pitch Stiffness (Nm/rad)	Cr. Flutter Speed (m/s)	Cr. Flutter Frequency (Hz)
20,000	47.3	34.5	4.4
20,000	55.2	35.6	4.4
20,000	66.3	37.4	4.5
20,000	82.8	40.3	4.6
20,000	110.4	45.9	4.7
20,000	165.6	58.4	4.8

Table A3.1 3: Critical flutter speed and flutter frequency for plunge stiffness of 15,000 N/m.

Plunge Stiffness (N/m)	Pitch Stiffness (Nm/rad)	Cr. Flutter Speed (m/s)	Cr. Flutter Frequency (Hz)
15,000	47.3	31.9	3.8
15,000	55.2	33.4	3.9
15,000	66.3	35.8	4.0
15,000	82.8	39.7	4.0
15,000	110.4	46.8	4.1
15,000	165.6	62.1	4.4

Table A3.1 4: Critical flutter speed and flutter frequency for plunge stiffness of 12,000 N/m.

Plunge Stiffness (N/m)	Pitch Stiffness (Nm/rad)	Cr. Flutter Speed (m/s)	Cr. Flutter Frequency (Hz)
12,000	47.3	30.64	3.5
12,000	55.2	32.59	3.5
12,000	66.3	35.53	3.6
12,000	82.8	40.25	3.7
12,000	110.4	48.58	3.8
12,000	165.6	66.15	4.0

Table A3.1 5: Critical flutter speed and flutter frequency for plunge stiffness of 10,000 N/m.

Plunge Stiffness (N/m)	Pitch Stiffness (Nm/rad)	Cr. Flutter Speed (m/s)	Cr. Flutter Frequency (Hz)
10,000	47.3	30.1	3.3
10,000	55.2	32.4	3.3
10,000	66.3	35.9	3.3
10,000	82.8	41.3	3.4
10,000	110.4	50.7	3.5
10,000	165.6	70.2	3.8

3.2 Similitude check for different stiffness value combinations

Table A3.2 1: Similitude check table for different stiffness value combinations.

Plunge Stiffness	Torsional Stiffness	Uncoupled Plunge Natural Freqency (ωh)	Uncoupled Torsional Natural Frequency (ωα)	ωh/ωα
10,000	47.3	2.75	7.07	0.39
10,000	55.2	2.79	7.53	0.37
10,000	66.3	2.83	8.14	0.35
10,000	82.8	2.87	8.98	0.32
10,000	110.4	2.9	10.23	0.28
10,000	165.6	2.94	12.36	0.24
12,000	47.3	2.95	7.21	0.41
12,000	55.2	3	7.66	0.39
12,000	66.3	3.06	8.25	0.37
12,000	82.8	3.1	9.07	0.34
12,000	110.4	3.15	10.31	0.31
12,000	165.6	3.2	12.44	0.26
15,000	47.3	3.2	7.43	0.43
15,000	55.2	3.27	7.85	0.42
15,000	66.3	3.35	8.43	0.40
15,000	82.8	3.42	9.22	0.37
15,000	110.4	3.49	10.44	0.33
15,000	165.6	3.56	12.53	0.28
20,000	47.3	3.52	7.82	0.45
20,000	55.2	3.62	8.2	0.44
20,000	66.3	3.73	8.73	0.43
20,000	82.8	3.84	9.49	0.40
20,000	110.4	3.95	10.65	0.37
20,000	165.6	4.05	12.7	0.32
30,000	47.3	3.91	8.6	0.45
30,000	55.2	4.08	8.93	0.46
30,000	66.3	4.25	9.38	0.45
30,000	82.8	4.43	10.05	0.44
30,000	110.4	4.63	11.11	0.42
30,000	165.6	4.83	13.05	0.37

3.3 Observations during wind tunnel experiments

Table A3.3 1: Observations during wind tunnel experiments.

ATD Flutter Test 1	29.11.2005		
Stiffness Characteristics:			
K_α = 47.3 Nm/rad	K_h=30,000 N/m		
ρ=1.110 kg/m³			
Air speed, V (m/s)	**Time (sec)**	**Disturbance**	**Observations**
10.0	128	3 consecutive 5º pulses were given to the airfoil	Oscillations were damped
15.1	180	3 consecutive 5º pulses were given to the airfoil	Oscillations were damped
20.2	233	3 consecutive 5º pulses were given to the airfoil	Oscillations were damped
25.2	278	3 consecutive 5º pulses were given to the airfoil	Oscillations were damped
30.4	335	3 consecutive 5º pulses were given to the airfoil	Oscillations were damped
35.4	408	3 consecutive 5º pulses were given to the airfoil	Oscillations were damped
40.9	468	3 consecutive 5º pulses were given to the airfoil	Oscillations were damped
45.8	516	3 consecutive 5º pulses were given to the airfoil	Oscillations were damped
52.8	590	3 consecutive 5º pulses were given to the airfoil	Oscillations were damped
55.5	641	3 consecutive 5º pulses were given to the airfoil	Oscillations were damped
60.2	724	3 consecutive 5º pulses were given to the airfoil	Oscillations were damped
64.9	780	3 consecutive 5º pulses were given to the airfoil	Oscillations were damped

Table A3.3 1 (Continued): Observations during wind tunnel experiments.

69.7	842	3 consecutive 5º pulses were given to the airfoil	Oscillations were damped
74.7	933	3 consecutive 5º pulses were given to the airfoil	Oscillations were damped
ATD Flutter Test 2	30.11.2005		
Stiffness Characteristics:			
K_α = 55.2 Nm/rad	K_h=10,000 N/m		
ρ =1.116 kg/m³			
Air speed, V (m/s)	**Time (sec)**	**Disturbance**	**Observations**
9.5	188	3 consecutive 5º pulses were given to the airfoil	Oscillations were damped
20.0	298	3 consecutive 5º pulses were given to the airfoil	Oscillations were damped
25.0	409		
29.7	464		
39.2	577		
49.7	693		
60.6	814	5º pulse was given the the airfoil	Undamped oscillations were observed. Data acquired revealed that the airfoil was fluttering.
ATD Flutter Test 3	30.11.2005		
Stiffness Characteristics:			
K_α = 55.2 Nm/rad	K_h=10,000 N/m		
ρ =1.116 kg/m³			
Air speed, V (m/s)	**Time (sec)**	**Disturbance**	**Observations**
44.9	72	6 consecutive pulses with magnitudes of 1º to 6º were given to the airfoil	Oscillations were damped

Table A3.3 1 (Continued): Observations during wind tunnel experiments.

47.5	107	6 consecutive pulses with magnitudes of 1º to 6º were given to the airfoil	Oscillations were damped
50.0	201	6 consecutive pulses with magnitudes of 1º to 6º were given to the airfoil	After 6º pulse, limit cycle oscillations were observed. Then The air speed was reduced to 47.5 m/s and the oscillations remained. Oscillations were damped when the air speed was reduced to 46.94m/s.
47.5	574	11 consecutive pulses with magnitudes of 1º to 11º were given to the airfoil	Oscillations were damped, limit cycle was not observed.
48.0	716	9 consecutive pulses with magnitudes of 1º to 9º were given to the airfoil	After 9º pulse, limit cycle was observed, then the air speed wa reduced to 45.97m/s and the oscillations were damped.
ATD Flutter Test 4	30.11.2005		
Stiffness Characteristics:			
K_α = 55.2 Nm/rad	K_h=10,000 N/m		
ρ =1.116 kg/m³			

Table A3.3 1 (Continued): Observations during wind tunnel experiments.

Air speed, V (m/s)	Time (sec)	Disturbance	Observations
51.0	100	7 consecutive pulses with magnitudes of 1º to 7º were given to the airfoil	After 7º pulse, limit cycle was observed, with the same magnitude of -10º/+-10º. The limit cycle oscillations were damped at V=47.03m/s, t=196sec..
52.0	297	6 consecutive pulses with magnitudes of 1º to 6º were given to the airfoil	After 6º pulse, limit cycle was observed, with the same magnitude of -10º/+-10º. The limit cycle oscillations were damped at V=46.9m/s, t=371sec..
53.0	422	6 consecutive pulses with magnitudes of 1º to 6º were given to the airfoil	After 6º pulse, limit cycle was observed, with the same magnitude of -10º/+-10º. The limit cycle oscillations were damped at V=46.1m/s, t=550sec..
53.0	622	An 8º pulse was given to the airfoil.	Limit cycle oscillations with the same amplitude of -10º/+-10º were observed.
53.1	693	Disturbance from plunge degree of freedom was given by forcing the motor and gearbox was given to the system	Oscillations were damped.

Table A3.3 1 (Continued): Observations during wind tunnel experiments.

54.1	862	6 consecutive pulses with magnitudes of 1º to 6º were given to the airfoil	After 6º pulse limit cycle oscillations with the same amplitude of -10º/+-10º were observed. The plunge motion could not be stopped by hand during these oscillations.
55.0	1,000	6 consecutive pulses with magnitudes of 1º to 6º were given to the airfoil	After 6º pulse, limit cycle oscillations with the same amplitude of -10º/+-10º were observed.
56.0	1,177	6 consecutive pulses with magnitudes of 1º to 6º were given to the airfoil	After 6º pulse, limit cycle oscillations with the same amplitude of -10º/+-10º were observed upto t=1267 sec.
ATD Flutter Test 5	30.11.2005		
Stiffness Characteristics:			
K_α = 55.2 Nm/rad	K_h=10,000 N/m		
ρ =1.116 kg/m³			
Air speed, V (m/s)	**Time (sec)**	**Disturbance**	**Observations**
56.0	93	Disturbance from plunge degree of freedom was given by forcing the motor and gearbox was given to the system	Limit cycle oscillations with the same amplitude of -10º/+-10º were observed.
57.0	200	A 6º pulse was given to the airfoil.	Limit cycle oscillations with the same amplitude of -10º/+-10º were observed.

Table A3.3 1 (Continued): Observations during wind tunnel experiments.

57.0	360	A 10º pulse was given to the airfoil.	Limit cycle oscillations with the same amplitude of -10º/+-10º were observed.
58.0	495	5 consecutive pulses with magnitudes of 1º to 5º were given to the airfoil	After 5º pulse, limit cycle oscillations with the same amplitude of -10º/+-10º were observed. At t=600 a -5º pulse was given to the airfoil. Limit cycle oscillations were damped. Then at the same air speed, 6 consecutive pulses with magnitudes of -1º to 6º were given to the airfoil. After 6º pulse at t=667, limit cycle oscillations were observed with the same amplitude of -10º/+10º
59.0	780	6 consecutive pulses with magnitudes of 1º to 6º were given to the airfoil	After 6º pulse limit cycle oscillations with the same amplitude of -10º/+-10º were observed. Then negative consecutive pulses from-1º to -6º were given. Limit cycle oscillations were observed after the 6th pulse and oscillations could not be stopped by hand. Then air speed was reduced and oscillations were damped.

Table A3.3 1 (Continued): Observations during wind tunnel experiments.

ATD Flutter Test 6	30.11.2005		
Stiffness Characteristics:			
K_α = 55.2 Nm/rad	K_h=10,000 N/m		
ρ =1.116 kg/m³			
Air speed, V (m/s)	**Time (sec)**	**Disturbance**	**Observations**
60.1	85	5 consecutive pulses with magnitudes of 1º to 5º were given to the airfoil	After 5º pulse, limit cycle oscillations with the same amplitude of -10º/+-10º were observed. Then negative pulse was given but oscillations did not damp, so the air speed was reduced, limit cycle oscillations were damped and then set again to 60.05. An 8º pulse was given to the system and limit cycle oscillations were observed with the same amplitude.
60.5	405	5 consecutive pulses with magnitudes of 1º to 5º were given to the airfoil	Oscillations started but stopped suddenly. Further investigation of the system revealed that the bolts connecting the linear guide interfaces to the casing were loosened and the airfoil was bend to touch the wind tunnel ground.

Table A3.3 1 (Continued): Observations during wind tunnel experiments.

ATD Flutter Test 6	30.11.2005		
Stiffness Characteristics:			
K_α= 55.2 Nm/rad	K_h=10,000 N/m		
ρ =1.116 kg/m³			
Air speed, V (m/s)	**Time (sec)**	**Disturbance**	**Observations**
60.5	80	5 consecutive pulses with magnitudes of 1º to 5º were given to the airfoil	After 5º pulse, flutter was observed.

APPENDIX 4

GRAPHS OF EXPERIMENTAL DATA

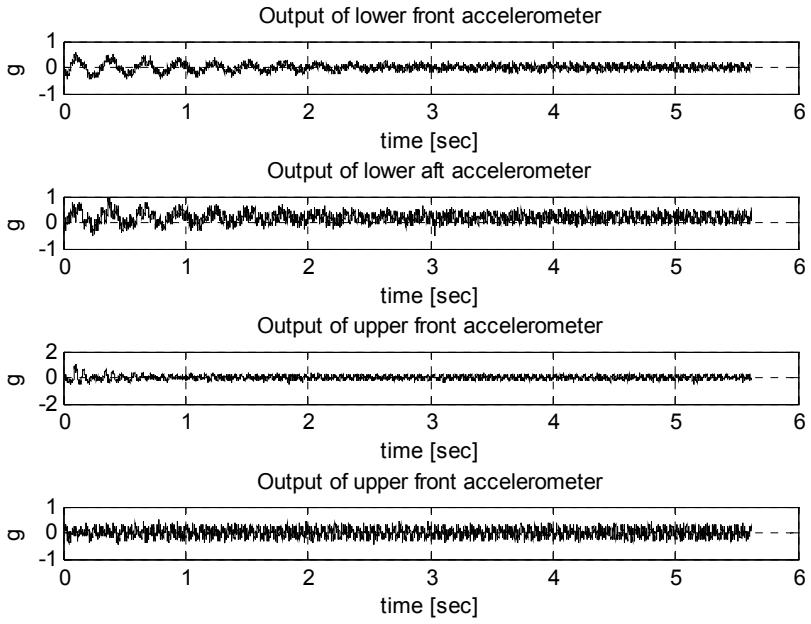

Figure A4. 1: Accelerometer measurements during 2º pulse response at U=10 m/s.

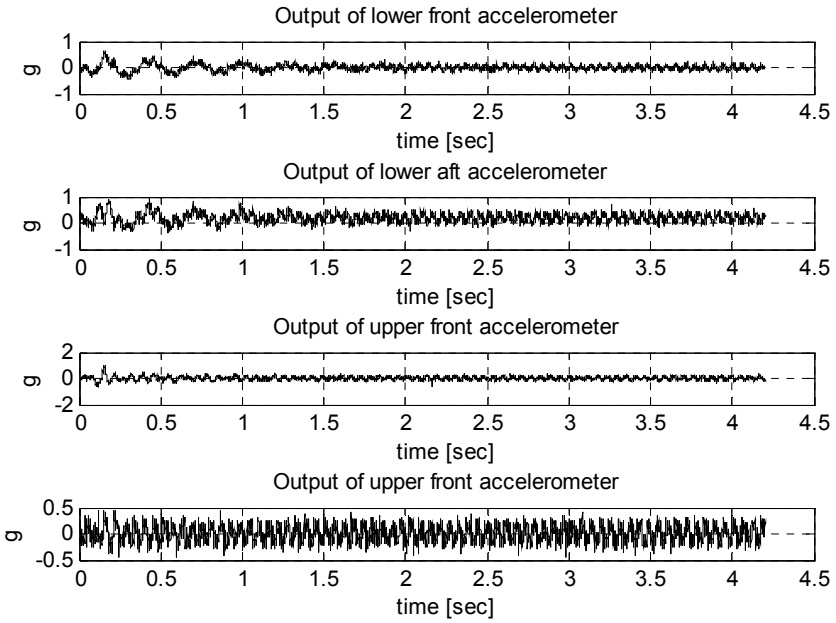

Figure A4. 2: Accelerometer measurements during 2º pulse response at U=20 m/s.

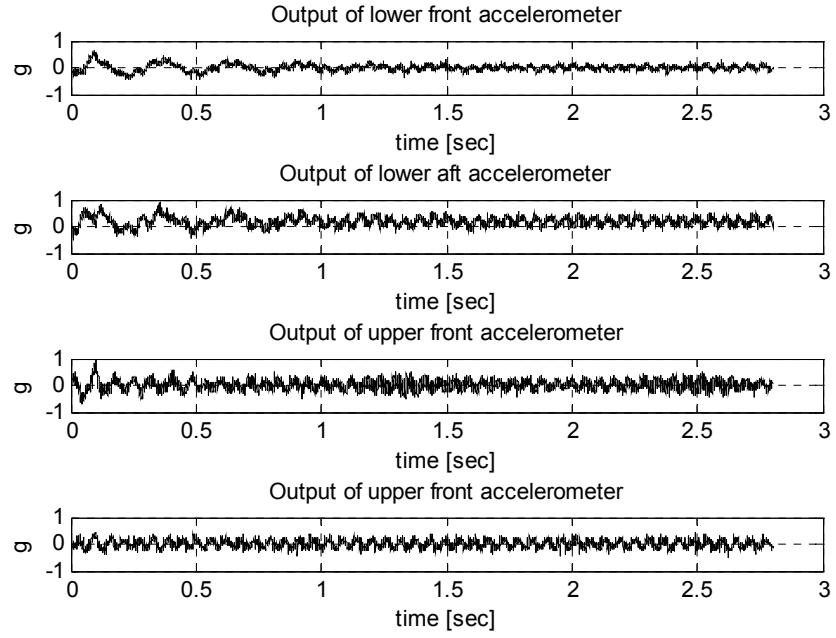

Figure A4. 3: Accelerometer measurements during 2º pulse response at U=30 m/s.

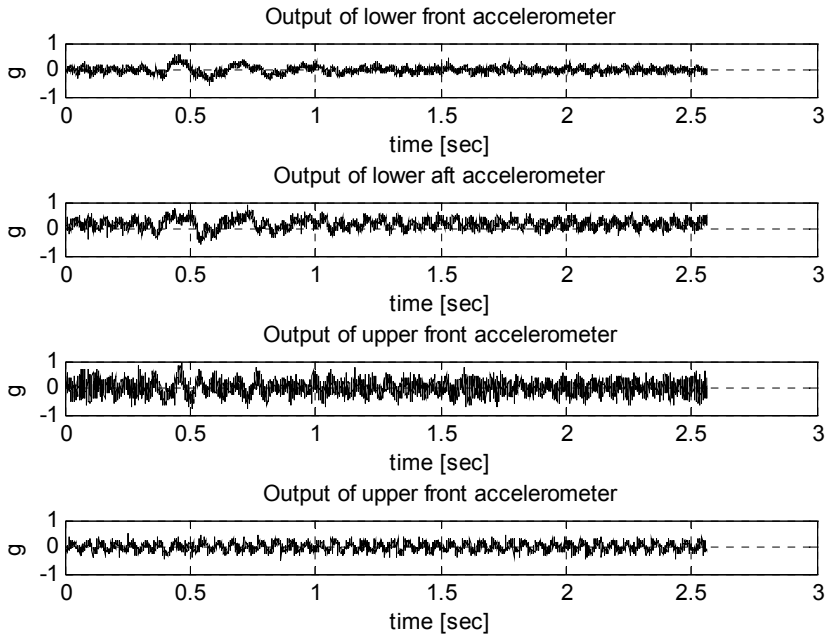

Figure A4. 4: Accelerometer measurements during 2º pulse response at U=40 m/s.

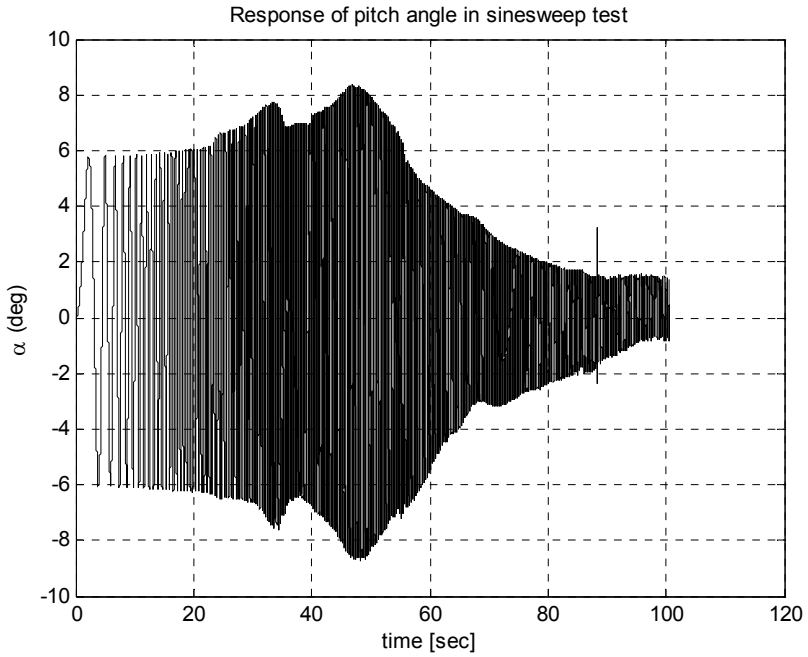

Figure A4. 5: Pitch response in sinesweep test with input amplitude of 6º before the modifications.

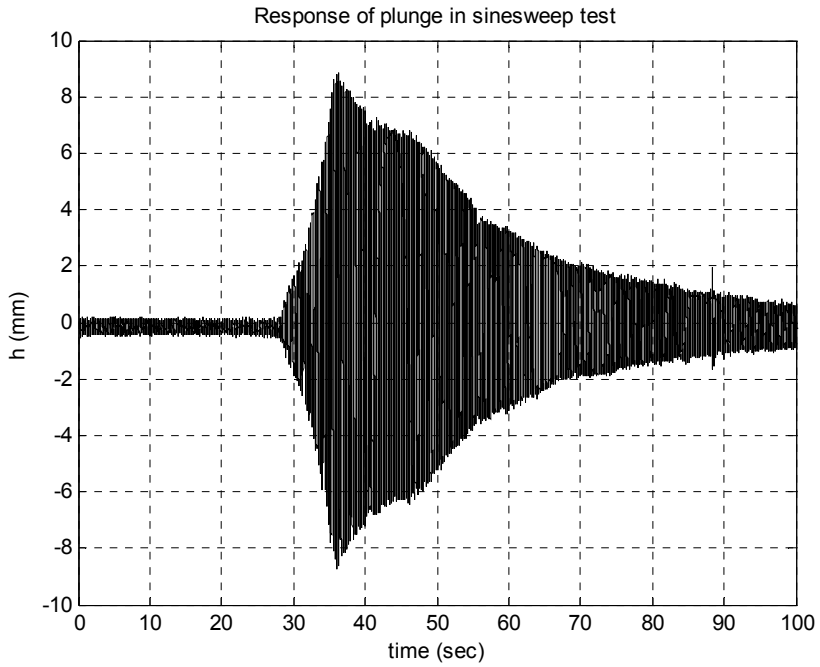

Figure A4. 6: Plunge response in sinesweep test with input amplitude of 6º before the modifications.

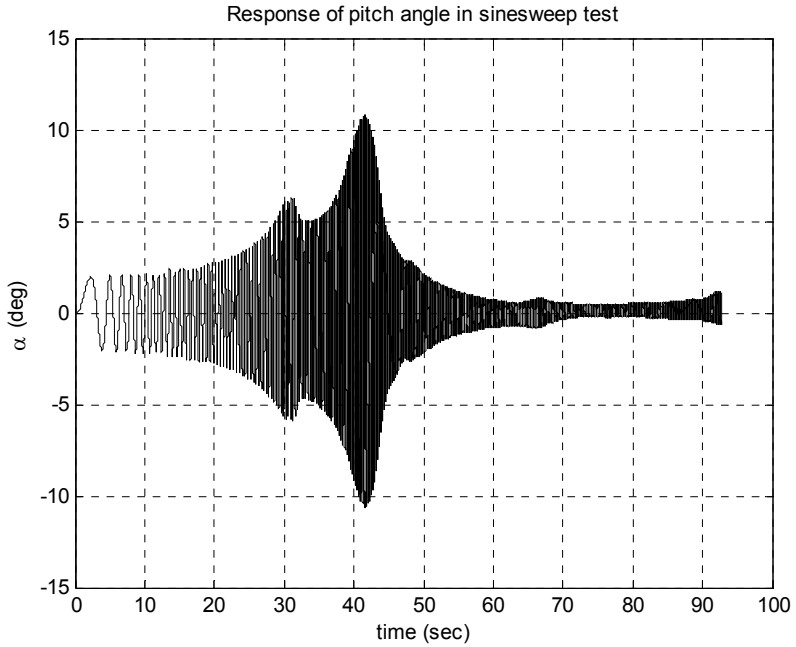

Figure A4. 7: Pitch response in sinesweep test with input amplitude of 2º after the modifications.

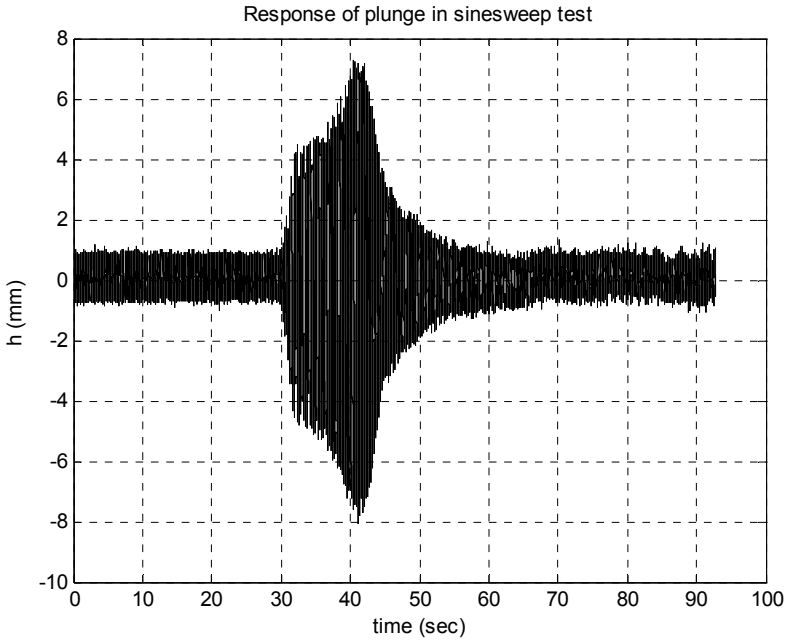

Figure A4. 8: Plunge response in sinesweep test with input amplitude of 2º after the modifications.